Fracture Experiments of Single Grain Boundaries in Ductile Metals

Vom Promotionsausschuss der
Technischen Universität Hamburg-Harburg
zur Erlangung des akademischen Grades
Doktor-Ingenieur (Dr.-Ing.)
genehmigte Dissertation

von
Daniel Kupka

aus
Saarlouis

2013

Gutachter:

- Prof. Dr.-Ing. habil. Norbert Huber
- Prof. Dr. rer. nat. Gerold Schneider

Tag der mündlichen Prüfung: 29. August 2013

urn:nbn:de:gbv:830-tubdok-12474

Fracture Experiments of Single Grain Boundaries in Ductile Metals

Daniel Kupka

Institute of Materials Research, Materials Mechanics,
Helmholtz-Zentrum Geesthacht, 21502 Geesthacht, Germany.
Contact: daniel.kupka@hzg.de

Abstract

The fracture toughness of metals is significantly reduced when intergranular fracture is involved in the propagation process of a crack while the structure of the grain boundaries determines their resistance against fracture. Thus, relations between the grain boundary structure and the macroscopic fracture toughness need to be established to improve predictions of the fracture process.

Within this work a test method was developed to fracture single grain boundaries in a plastically deforming metal. This method is based on a micro-cantilever bending technique. The aluminum-lithium alloy 2198 was chosen as a model material due to the morphology of the microstructure which provides flat elongated grains. The grains of this alloy were plastically deformed prior to the fracture of the grain boundary. However, the grain boundary showed brittle fracture; no damage was found prior to the complete fracture of the grain boundary.

The anisotropic plastic deformation properties of the grains were determined using a hybrid approach involving micro-column compression experiments on single crystalline columns and crystal plasticity finite element simulations. The adjusted material model was applied within finite element simulations of the cantilevers and it was shown that the deformation of the cantilevers can be predicted by the finite element models.

Finally, the fracture of a single grain boundary was modeled making use of a cohesive zone model. The methodology was applied to two cantilevers with significantly different deformation characteristics in order to determine the stress at damage initiation of the respective grain boundaries.

Bruchversuche an einzelnen Korngrenzen in duktilen Metallen

Daniel Kupka
Institut für Werkstoffforschung, Werkstoffmechanik,
Helmholtz-Zentrum Geesthacht, 21502 Geesthacht, Deutschland.
Kontakt: daniel.kupka@hzg.de

Zusammenfassung

Metalle, bei denen sich Risse entlang von Korngrenzen ausbreiten, weisen im Allgemeinen eine geringere Bruchzähigkeit auf als Metalle bei denen transkristallines Risswachstum dominiert. Die Trennfestigkeit der einzelnen Korngrenzen hängt wiederum von ihrer inneren Struktur ab. Daher müssen Beziehungen zwischen der Struktur der Korngrenzen und der makroskopischen Bruchzähigkeit ermittelt werden, um die Vorhersage des Bruchprozesses zu verbessern.

Im Rahmen dieser Arbeit wurde eine Methode entwickelt, die es ermöglicht, Bruchversuche an einzelnen Korngrenzen durchzuführen. Die Methode basiert auf dem Biegen mikroskopisch kleiner Kragarmproben. Die Aluminium-Lithium Legierung 2198 wurde auf Grund der Gefügemorphologie, mit flachen Körnern, als Modellmaterial ausgewählt. Bei den Biegeversuchen verformten dich die Körner zunächst plastisch, bevor der Bruch der Korngrenze einsetzte. Die Korngrenze selbst brach spröde, d. h. es konnte keine Schädigung der Korngrenze nachgewiesen werden bevor diese brach.

Die anisotropen plastischen Verformungseigenschaften der Körner wurden anhand von Mikrokompressionsversuchen an einkristallinen Mikrosäulen bestimmt. Zur weiteren Auswertung wurden mit Hilfe dieser experimentellen Daten die Parameter eines Finite Elemente Kristallplastizitätsmodells ermittelt. Es konnte gezeigt werden, dass die Verformung der mikroskopischen Kragarme mit diesem kalibrierten Materialmodell vorhergesagt werden kann.

Schließlich wurde der Bruch der Korngrenze unter Zuhilfenahme eines Kohäsivzonenmodells modelliert. Die kritische Bruchspannung wurde exemplarisch für zwei Korngrenzen in Proben mit deutlich unterschiedlichem Verformungsverhalten ermittelt.

Contents

Nomenclature

A	area of an indent
a	depth of the U-notch
$\bar{A}$	average column area
B	cantilever width
C_{11}, C_{12}, C_{44}	elastic constants of a cubic symmetric material in Voigt notation
$C_0 \dots C_n$	constants describing the area function of the indenter tip
CRSS	critical resolved shear stress
CSM	continuous stiffness measurement
$\mathbf{C}$	fourth order elasticity tensor
d	distance from the center of the U-notch to the support of the cantilever
$\bar{D}$	average column diameter
D_{foot}	diameter at the foot of the column
D_{top}	diameter at the top of the column
D	damage variable
$\mathbf{D}, \mathbf{D}^*, \mathbf{D}^{\text{p}}$	total stretching tensor and stretching tensor associated with the lattice and the plastic deformation, respectively
E	elastic modulus
e	initial thickness of the cohesive layer
E_{eff}	effective elastic modulus
E_{i}	elastic modulus of the indenter material
E^{sim}	elastic modulus used within a simulation
FIB	focused ion beam
$\mathbf{F}^{\text{p}}$	deformation gradient associated with plastic deformation

$\mathbf{F}^*$	deformation gradient associated with stretching and rotation
$\mathbf{F}$	deformation gradient
G_f	fracture energy of the cohesive elements
H	cantilever height
h	displacement of the nanoindenter tip with reference to the sample surface
h_0	initial hardening modulus
$\mathcal{H}$	hardness
$h_\mathrm{const}^\mathrm{cor}$	correction for deviations from linear loading prior to the yield point
$h_\mathrm{el}^\mathrm{cor}$	displacement associated with elastic deformations only
$\dot{h}$	displacement rate of the indenter
h^ind	indentation depth into a cantilever
$h_\mathrm{el}^\mathrm{ind}$	indentation depth corresponding to elastic deformations only
$h_\mathrm{pl}^\mathrm{ind}$	indentation depth corresponding to plastic deformations only
H_0	initial height of a micro-column
h_pl	displacement of the nanoindenter tip associated with plastic deformation only
h_raw	displacement of the indenter tip measured from the surface of the sample
h_Y	displacement at the yield point
$h_{\alpha\beta}$	hardening moduli for the interaction of the deformed slip system β with the slip system α
K	elastic cohesive normal stiffness
$K_\mathrm{b}^\mathrm{CSM}$	elastic stiffness of the cantilever measured by CSM
$K_\mathrm{sys}^\mathrm{CSM}$	combined stiffness of the cantilever and the indent measured by CSM
K^exp	cantilever stiffness determined in an experiment
$\hat{K}$	normalized stiffness
K_S	elastic cohesive shear stiffness

K^{sim}	cantilever stiffness determined from a simulation
K^*	stiffness of a cantilever
$\mathbf{L}$	velocity gradient
L	cantilever length
$\hat{l}$	characteristic length of a cantilever
$\mathbf{L}^{\mathrm{p}}$	velocity gradient associated with plastic deformation
$\mathbf{L}^*$	velocity gradient associated with stretching and rotation of the lattice
m	Schmid factor for a slip system
$\mathbf{m}^\alpha$	slip direction of slip system α
$\mathbf{n}^\alpha$	normal vector of to the slip plane of slip system α
P	load
$\hat{P}$	normalized load
$P_{\max}$	maximum load on an indent
$P_{\max,i}$	maximum load before unloading segment i
P_{Y}	load at the yield point
q_{cp}	interaction coefficient for coplanar slip
q_{ncp}	interaction coefficient for non-coplanar slip
$q_{\alpha\beta}$	hardening interaction coefficient for the interaction of slip systems α and β
R	radius of the U-notch
$\mathbf{R}$	rotation tensor
S	indent stiffness
$S_{\mathrm{ind}}^{\mathrm{CSM}}$	indent stiffness measured by CSM
S_{fc}	maximum loading slope in a micro-compression experiment
t	cohesive normal traction
$\bar{t}$	cohesive normal traction if no damage would be present in the cohesive zone
t_{i}	cohesive normal traction at damage initiation

$\mathbf{v}_{\text{crystal}}$	vector in the crystal coordinate system
$\mathbf{v}_{\text{global}}$	vector in the global coordinate system
w	cantilever deflection
w_{l}	cantilever deflection referring to a loading segment
w_{r}	cantilever deflection referring to a reloading segment
β	geometrical factor related to the indenter tip geometry
δ	cohesive displacement
δ_{f}	cohesive displacement at total fracture
δ_{i}	cohesive displacement at initiation of fracture
$\dot{\epsilon}$	nominal strain rate of a micro-compression experiment
ε	engineering plastic strain
ε_δ	cohesive strain
$\bar{\gamma}$	accumulated plastic strain
$\dot{\gamma}^\alpha$	shear rate on slip system α
$\dot{\gamma}_0^\alpha$	reference shear rate on slip system α
ν	Poisson ratio
ν_{i}	Poisson ratio of the indenter material
$\mathbf{\Omega}, \mathbf{\Omega}^*, \mathbf{\Omega}^{\text{p}}$	total spin tensor and spin tensor associated with the lattice and the plastic deformation, respectively
(ϕ_1, Φ, ϕ_2)	Eulerian angles to describe a crystallographic orientation
σ	engineering stress
$\boldsymbol{\sigma}$	Cauchy stress tensor
ς	normal stress on a slip system
τ	resolved shear stress on a slip system
τ_0	initial resistance to slip
τ^α	resolved shear stress on slip system α
τ_∞	saturation hardening shear stress
τ_{Y}^α	resistance against slip of slip system α at instant time

$\dot{\tau}_{\mathrm{Y}}^{\alpha}$	rate of change in resistance to slip of slip system α
θ	misorientaion angle
ξ	ratio between the elastic moduli of AA2198 and pure aluminum

1 Introduction

The resistance of metals to fracture is mostly characterized by macroscopic quantities of which the fracture toughness is the most popular. Detailed knowledge of the microscopic mechanisms involved during the fracture process is required to predict the macroscopic fracture properties. These microscopic mechanisms are controlled by microstructural features such as the grain size and the ductility of the grains, inclusions or pores and the grain boundaries.

The macroscopic fracture properties of aluminum lithium lightweight alloys are significantly influenced by the structure of the grain boundaries. It has been found that the macroscopic fracture toughness of such alloys is reduced when cracks advance along the grain boundaries [1]. With advanced heat treatment the yield stress was shown to increase while the fracture toughness decreased with respect to the quenched material taken as a reference (see figure 1.1). A reversion heat treatment was carried out to dissolve any precipitates in the grain interior while the grain boundary structure largely remained unaltered. The yield stress of the reference material was restored, indicating that all precipitates in the grain interior had been dissolved but the fracture toughness was significantly decreased compared to the reference material. The difference between the quenched (**I**) and the reverted material (**II**) was attributed to the different structure of the grain boundaries which were covered by precipitates in the reverted material as can be seen from the transmission electron images in figure 1.1. The results of [1] clearly show that the structure of the grain boundaries is responsible for the decreased fracture toughness and, as expected, a large extent of intergranular fracture was observed when grain boundary precipitates were present.

The mechanisms responsible for the increasing sensitivity of the aluminum lithium alloys toward intergranular fracture are subject to debate. Several approaches are based on local strain concentrations on particles at the grain boundaries or due to precipitate free zones adjacent to the grain boundaries [2]. Unfortunately, macroscopic experiments provide limited information about the fracture mechanisms on single grain boundaries due to the unknown local stress state at the respective grain boundaries and plastic deformation in the adjacent grains. In order to overcome these limitations experimental methods are required to conduct tests on specific grain boundaries involving well defined stress fields. The ability to fabricate small-scale site-specific test specimens of known geometry together with high resolution load-displacement measurements enable the development of such experiments which, in turn, provide a better understanding of the material properties on the macroscopic scale.

The challenge for this work was to develop a method that is capable of fracturing single grain boundaries and to provide a measure for their resistance to damage and

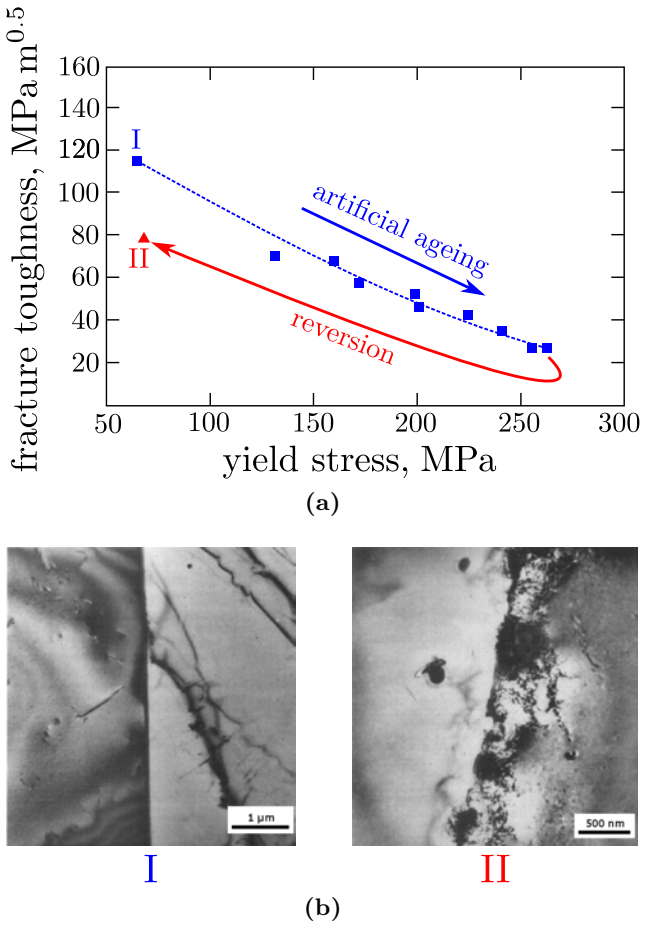

Figure 1.1 (a) Yield stress versus fracture toughness for different heat treatments of an aluminum lithium alloy (figure reproduced from [1]). **I** marks the reference specimens as quenched and **II** marks the fully reverted specimens. (b) Representative TEM images from grain boundaries of the specimens corresponding to the heat treatments **I** and **II**.

fracture. In particular, the analysis required the anisotropic plastic deformation of the grains adjacent to the boundary to be taken into account. Therefore, a hybrid approach of micro-mechanical testing and finite element analysis incorporating a crystal plasticity model has been chosen. This leads to the following structure of this thesis (see figure 1.2): In chapter 2 the experimental methods to access the material properties on the micro-scale are reviewed with a focus on the techniques that enable microscopic fracture experiments. The basic techniques required for the fabrication and the testing of microscopic specimens and the characterization of the material are outlined in chapter 3. Chapter 4 is dedicated to the development of the experimental approach for microscopic fracture experiments on single grain boundaries including the measuring techniques for the initiation and propagation of an interfacial crack. The plastic deformation of the grains adjacent to the grain

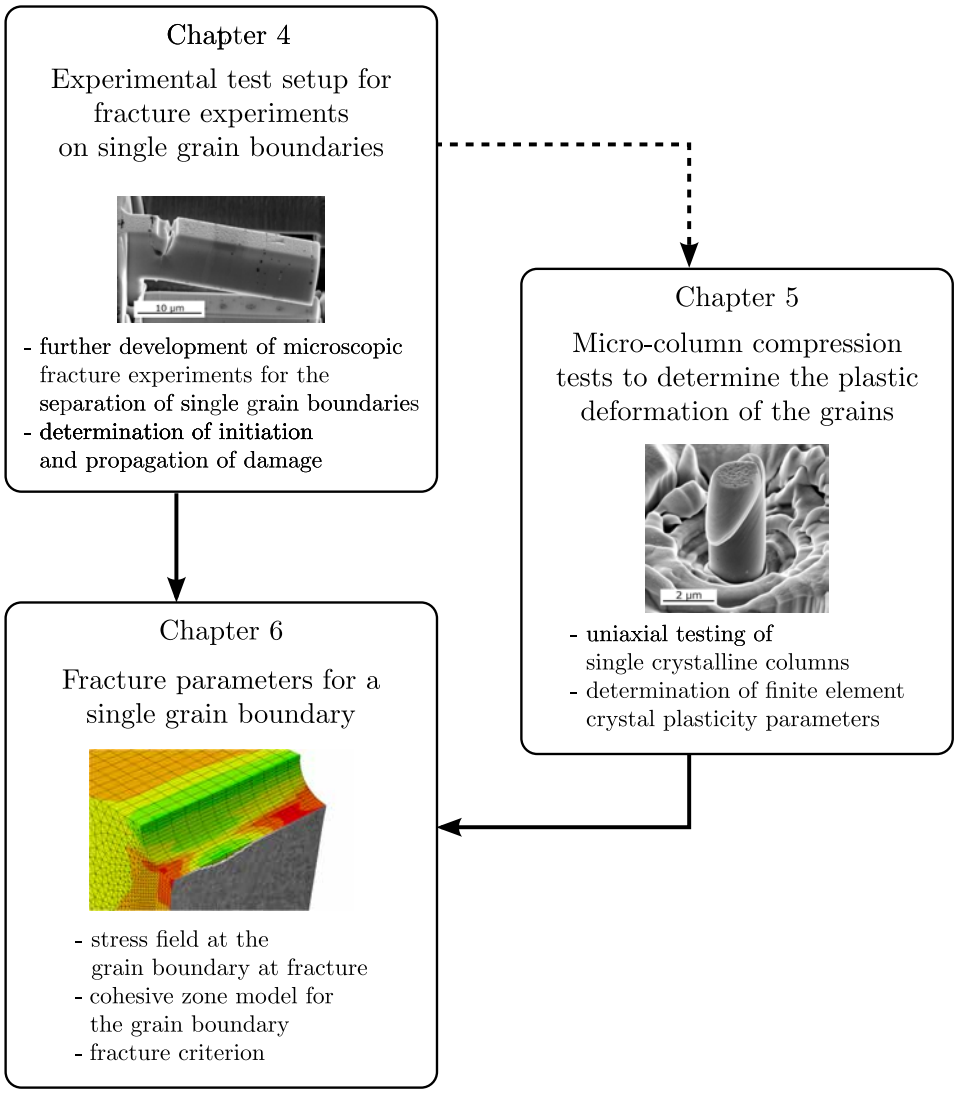

Figure 1.2 Key aspects of the thesis corresponding to chapters 4, 5 and 6.

boundary must be taken into account through an adequate constitutive law. Micro-column compression experiments on single crystals that provide access to the plastic deformation of a single grain are presented in chapter 5. The plastic deformation is thereby expressed through a finite element crystal plasticity model. In chapter 6 this model is transferred to the microscopic bending/fracture experiments. In order to model the fracture of a grain boundary a cohesive zone, which allows to determine the stress at damage initiation, is included into the simulations. Finally, the method is evaluated by applying it to two cantilevers with significantly different deformation behavior. In figure 1.2 the key aspects of this work as presented in chapters 4, 5 and 6 are summarized. Finally, the conclusions that can be drawn from this work and suggestions for future work are presented in chapter 7.

2 Literature Review

During the last decade, the commercial availability of focused ion beam systems has triggered the development of a wide variety of small scale specimens for novel micro-mechanical testing, since it provides the possibility to fabricate specimens of various geometries at distinct locations in bulk materials with a precision of approximately ten nanometers. Together with highly precise measuring and actuation techniques, experiments have been designed that provide insight into the micro-mechanical mechanisms that determine material properties regarding the deformation and failure. Single components of the microstructure, e. g. single grains or layers in composite materials, have been isolated and tested under well defined stress and strain fields. The results provide a better understanding for the microscopic processes which determine the material properties on the macroscopic scale.

The experimental methods that are presented here provide an overview of the possibilities and limitations of micro-mechanical testing for studying local material properties with a focus on metals. In particular, microscopic fracture experiments on bulk materials and interfaces are presented which, to date, are limited to brittle materials.

2.1 Determination of Local Material Properties using Indentation Testing

The principle of instrumented indentation is to press an indenter of well defined geometry into a surface while measuring the load and the displacement. The interpretation of indentation data to obtain material properties is described by Oliver and Pharr [3, 4]. A short review of this important method is given in chapter 3. The plastic deformability of the materials is usually described by the hardness. The method has been applied to a wide variety of materials including biological materials [5, 6], ceramics [7, 8], metals [9] and polymers [10]. Enabling measurements at small indentation depths, nanoindentation is particularly useful for investigations into the material properties of thin films [11, 12, 13].

The continuous measurement of load and displacement enables the design of experiments to determine elastic and plastic material properties [14, 15]. Moreover, they allow for the local determination of the material properties while the lateral resolution depends on the size of the indent and, thus, the indentation depth. There has been considerable effort in order to increase the lateral resolution by conducting measurements at small indentation depths. Today nanoindentation systems (or nanoindenters) have been developed which provide accurate control of load and

displacement on the order of sub-nanometers and micro-Newtons, respectively. The working principle of a nanoindenter is described in chapter 3.

Indentation experiments provide the advantage of a relatively simple preparation of the samples which makes the method quite versatile for a large variety of specimens and materials. However, the interpretation of the data from indentation experiments is difficult due to the complex stress field under the indent and because the deformed volume constantly increases with increasing indentation depth.

2.2 Micro-column Compression Experiments

In order to overcome the difficulties associated with the interpretation of nanoindentation experiments, it is preferred to conduct tests with well defined uniaxial stress fields and constant volumes of deformation. Tensile and compression experiments on microscopic specimens meet these requirements. However, the challenges are to fabricate those specimens and to develop testing procedures that provide the required high resolution in terms of load and displacement. The development of the focused ion beam microscope (FIB) with high resolution milling capabilities (see chapter 3) has triggered the development of specimens with characteristic dimensions of less than 10 µm, while the high resolution of the nanoindenter in terms of loads and displacement has been used to carry out the mechanical testing [16].

Tensile tests of microscopic samples for thin films [17, 18, 19] and bulk materials [20] have been developed. Such tests provide the desired uniaxial stress state and constant deformation volumes. However, there are problems associated with the fabrication, the handling and the loading of such specimens. In contrast, microscopic compression tests can be conducted at any location within the material and, moreover, the effort for the preparation and the handling of these specimens is significantly reduced.

In order to investigate the influence of the size of the specimens on the deformation properties Uchic *et al.* [16] fabricated cylindrical micro-columns into flat surfaces of nickel single crystals. The yield stress of the columns was found to increase with decreasing diameter of the columns. Compression tests on single crystals of metals have confirmed these findings and the yield stress has been found to be approximately proportional to the inverse square root of the diameter [21, 22, 23]. Various models have been proposed to explain this size-effect [24, 25, 26], but to date no consensus has been reached.

There are some limiting considerations to the interpretation of micro-compression experiments as discussed by Zhang *et al.* [27], Kiener *et al.* [28] and Kirchlechner *et al.* [29]. They mainly address inhomogeneities of the stress field which are caused by the geometry of the column or by the imposed boundary conditions during loading. It is pointed out that friction between the indenter head and the top of the column is unavoidable and the indenter shaft is designed to be stiff regarding lateral directions. Hence, the deformation at the top of the column is constrained and a multiaxial stress field is induced. Moreover, stress concentrations may be induced due to irregularities at the attachment of the specimen to its substrate. A tapered column

geometry induces a strain gradient due to the variation of the diameter along the columns axis thereby reducing the influence of the attachment to the substrate. In general, higher aspect ratios would be desirable to create a homogeneous uniaxial stress field but this is circumvented by buckling of such specimens.

Multiple constraints associated with the geometry of the specimen and the test method must be taken into account for the analysis of the load-displacement data from micro-compression experiments. If these constraints are considered micro-compression experiments provide local measurements of the material properties. As pointed out in section 5.1, finite element simulations are a highly versatile tool to incorporate the constraints into the analysis of the load-displacement data [30].

2.3 Micro-beam Bending

For some investigations on the microscopic scale tensile stresses are of interest. While micro-tensile experiments can be difficult to achieve, as described above, micro-bending experiments have been developed as an alternative. Moreover, such tests allow for the investigation of the deformation properties of materials subject to a well defined strain gradient.

Weihs *et al.* [31] designed a cantilever deflection experiment to determine the elastic moduli and the yield strengths of thin gold films on SiO_2 substrates using a simple beam bending theory. Florando and Nix [32] investigated the properties of copper thin films on silicon substrates by a similar technique, making use of a cantilever with in-plane triangular geometry in order to obtain a uniform state of plane strain in the film. They have shown that it is possible to separate the properties of the film from the properties of the substrate by using an average stress model which does not impose any constraints on the properties of the film, i. e. no constitutive law is assumed.

In order to investigate the effect of well defined strain gradients on the deformation of metals Stölken and Evans [33] developed a bending method for thin foils. Their goal was to determine the inherent length scale of the material when applying a phenomenological law of strain gradient plasticity. Annealed nickel foils were bent over a small mandrel which enables the determination of the bending moment and the deformation. Starting from a strain gradient plasticity equation, the bending moment was linked to the strain gradient and the intrinsic length scale for strain gradient plasticity from bending was determined.

Single crystalline cantilever beams have been tested by Motz *et al.* [34] to investigate the effects of strain gradients in single crystals. Here the FIB was used to fabricate cantilever beams out of a bulk copper sample which were then bent making use of a nanoindenter. Again a size effect was revealed with an increase of the yield stresses proportional to the reciprocal height of the cantilevers. This effect is explained by a combination of strain gradient plasticity with a pile-up of dislocations at the neutral plane. Demir *et al.* [35] generalized this approach by introducing a mean-field breakdown theory.

For further analysis of micro-beam bending experiments the deformation of the support of the cantilever and the exact geometry must be taken into account. Finite element simulations have been applied to assess the deformation properties in terms of stresses and strains. Gong and Wilkinson [36, 37] fabricated cantilevers with triangular cross-sections out of single crystals of titanium and titanium alloys. The cantilevers were oriented to deform along the $\langle a \rangle$ prismatic slip systems. Finite element simulations were applied to determine the critical resolved shear stress (CRSS) for these slip systems by a fitting procedure. Apart from the size effect which was attributed to the dislocation pile-up at the neutral plane, the influence of alloying elements forming a solid solution or second phases was determined. It has been shown that by extrapolating the CRSS values to the bulk, reasonable values for the yield stresses of the respective alloys can be calculated.

While strain gradients have been shown to significantly influence the deformation properties of small scale specimens, the exact mechanisms that are responsible for the change of the mechanical properties are subject to current research.

2.4 Micro-fracture Experiments

The advance of micro-mechanical experiments to determine the local elastic and plastic properties of materials has triggered the development of microscopic fracture experiments to characterize the failure of small structures. Fracture experiments on specimens with dimensions on the order of less than a hundred micrometers are generally restricted to predominantly brittle materials. In ductile materials the plastic zone extends through the whole specimen circumventing any fracture.

Microscopic silicon cantilevers have been tested for their fracture strength by Wilson *et al.* [38]. They fabricated a set of micro-cantilevers out of silicon wafers using lithographic methods and carried out bending tests making use of a pin and a precision displacement table. In order to prevent slipping of the pin on the cantilever they fabricated a hole into the cantilevers which ensured a well defined loading point. The stresses and strains at the point of fracture were determined by making use of an anisotropic elastic finite element model. The fracture stress between 3.0 GPa and 3.6 GPa were reported. Referring to inconsistencies in these values with other reported values, the quality of the surface preparation is pointed out to be a decisive factor for micro-mechanical experiments.

Halford *et al.* [39] used focused ion beam milling to create cantilever specimens of γ-TiAl alloys. Fracture tests have been conducted with specimens oriented along various directions of the lamellar morphology of these alloys. As expected, a much smaller fracture toughness was determined for interlamellar fracture than for translamellar fracture. Investigations into the fracture strength of thin passivation films (silicon oxide and silicon nitride) have been carried out by Matoy *et al.* [40]. The cantilevers were fabricated combining photolithographic techniques and focused ion beam milling. The height of the cantilevers was chosen equivalent to the thickness of the film material while the substrate material was used as support of the fixed end. Additionally, a notch was milled into the cantilever close to the

supported end under perpendicular ion beam condition. A nanoindenter with a spherical tip was used to deflect the cantilevers without any visible imprint. The fracture stresses were determined from the load-displacement data using analytical solutions and finite element simulations. Moreover, finite element simulations provided the geometry function for the notch in the cantilever for evaluation of the fracture toughness. The fracture stresses and the fracture toughnesses determined by microscopic experiments were in good agreement with the expected values. However, finite element simulations of the complete structure with its support were needed to determine the elastic moduli correctly from the bending experiments. Iqbal *et al.* [41] conducted similar fracture experiments on varying orientations of NiAl-crystals. The determined values of the fracture toughness of [1 0 0] and [1 1 0] oriented cantilevers were in good agreement with values determined from macroscopic tests. Additional fracture experiments were carried out *in situ* in a SEM allowing for the direct observation of the fracture process. The micro-cantilevers in these works have been notched to create a well defined location for the fracture. During the notching process the ion beam was perpendicular to the top surface of the cantilevers. Hence, it is unknown for the specimens if the ion damage at the ground of the notch influenced the results of the measurements.

Similar fracture experiments with unnotched cantilevers have been carried out by Klüsner *et al.* [42] on ultra fine grained hard metal cantilevers of different sizes. With reduced specimen size inherent material defects have been avoided such that the high intrinsic tensile strength of the material could be determined.

In many cases of material failure damage is initiated at the interfaces between micro-structural components. Here it is of great interest to evaluate the separation properties of such interfaces in terms of maximum stresses and energies for the separation of the surfaces. Promising experimental approaches have been adopted from micro-fracture experiments using micro cantilever specimens on homogeneous materials. An interface of interest needs to be placed close to the supported end of the cantilever with the normal of the interface aligned with the beam axis. Hirakata *et al.* [43] followed this approach for investigations into the adhesion properties of a thin (200 nm) copper film on a silicon substrate. The film was covered by a silicon nitride passivation film (500 nm). Using focused ion beam milling, a cantilever specimen was produced with silicon at the support and the interface normal of the Si-Cu and Cu-SiN interfaces aligned with the cantilever axis. The cantilevers were deflected within a TEM since the positioning of the sample is crucial at the submicrometer dimensions. The initiation of the crack at the interface was observed and the critical load was determined. Finite element calculations assisted in the calculation of the stress fields at the interfaces while it was assumed that the Si and SiN deform elastically only. A Ramberg-Osgood law was assumed for the copper layer. The parameters to this law were determined such that the load-deflection curve could be reproduced by the finite element simulation. In addition to the cantilever bending experiments millimeter sized three point bending specimens with an interfacial crack were fabricated of the same material. The critical stresses for both of these experiments are in good agreement such that it was concluded that both processes can be described by a single criterion. Zhao *et al.* [44] reinvestigated the

results and concluded that the influence of the plastic deformation of the copper layer can be neglected and that a purely elastic model of the copper layer suitably describes the deformation and the induced stress fields. Therefore, any nonlinearity in the load displacement data has been attributed to the interfacial properties only. Furthermore, they introduce cohesive zone elements into the finite element simulations to determine the separation properties of the Si-Cu interface by fitting the parameters to match the load-displacement curves.

The method developed by Hirakata [43] has been applied by Matoy *et al.* [45] to interfaces between silicon oxide and films of copper, tungsten and tungsten co-sputtered with titanium respectively. The load deflection curves for these experiments are linear to the point of fracture. This indicates that only elastic deformations need to be considered. Analytical calculations and finite element simulations are used to determine the energy release rates for the fracture of these interfaces and the results of both methods are in good agreement. This indicates the potential of this method to measure the separation properties of interfaces on the microscopic scale. The lowest energy release rates (weakest interface) are found for copper films. Higher energy release rates are found for tungsten films and tungsten films co-sputtered with titanium show the highest energy release rates. It is pointed out, that the precision of these measurements strongly depends on the defect sizes in particular on the cantilever top.

Armstrong *et al.* [46] presented a method to separate grain boundaries in metals which makes use of cantilevers of pentagonal cross-section with a grain boundary placed close to its supported end. The cantilevers were deflected until the desired maximum load is reached. Some bending experiments were carried out in a acid solution of potassium tetrathionate. While the cantilever deflection remained constant at the maximum load with no acid present, the deflection increased continuously for experiments which were carried out in the acid solution. *Post mortem* SEM images of the cantilevers revealed that the failure was induced at the grain boundary as desired. Most recent work has been carried out on copper grain boundaries that have been embritteled with bismuth [47]. In this material system the grain boundaries either do not fracture or they fracture without any indication of plasticity prior to fracture. Moreover, no systematic dependence on the orientation of the grain boundary could be identified.

2.5 Position of this Work in the Context of Micro-mechanical Testing

As just presented, a variety of methods have been developed to investigate the deformation and fracture properties of materials at the micro-meter scale. To date fracture experiments have been developed for brittle materials without significant plastic deformation in the vicinity of the fracture site.

Within the present work the application of micro-mechanical experiments for the investigation of the fracture of single grain boundaries is further developed. A method for the determination of the initiation and propagation of damage at

the grain boundary is presented. Moreover, the anisotropic plastic deformation of the adjacent grains is taken into account by combining finite element crystal plasticity and micro-mechanical experiments. Micro-column compression tests are shown to allow the calibration of the material model independently from the fracture experiments. Finally, a cohesive zone has been introduced into the model to provide a fracture criterion for the grain boundary.

Summary of the Methods for Micro-mechanical Testing

- Instrumented indentation provides access to the local material properties while the analysis of the acquired data is complex due to the complex stress field under the indentation body and the increasing test volume.
- Micro-compression experiments are used to test constant small volumes which facilitates the analysis of stress strain behavior while the fabrication of the specimens is a limiting factor to the use of the method.
- Micro-bending experiments induce well defined strain gradients in small specimens. Moreover, such experiments have been used to overcome the difficult fabrication of microscopic tensile specimens to test microscopic materials in tension.
- Size effects have been found for various, mostly crystalline, materials and models for these size effects have been presented. When the dimensions of the specimens becomes small, both the yield stress and the hardening rate may increase ("smaller is stronger"). These effects need to be considered for investigations into the deformation of small specimens.
- Micro-fracture experiments have been successfully conducted on both amorphous and crystalline brittle materials such that analytical approximations could be used for the analysis.
- Micro-fracture experiments on interfaces have been carried out on brittle interfaces with brittle matrix components.
- The preparation of microscopic specimens is subject to limitations regarding the damage induced by the preparation technique and the precision of the geometry.

3 General Methods and Equipment

The fundamental methods and equipment of micro-mechanical testing that have been used within this thesis are described in the present chapter. Since the focused ion beam has been used to fabricate the test specimens the principles of ion beam milling are reviewed. For the mechanical testing of the specimens a nanoindentation system that provides high resolution for both the load and the displacement has been used. Hence, the working principle of a nanoindenter is presented. The principles of electron back scatter diffraction (EBSD) are also presented since it has been used to identify the individual orientations of the grains of the micro-fracture and micro-compression experiments. Finally, the concept of digital image correlation is presented, which has been used for the determination of local displacements during deformation.

3.1 Imaging and Milling using a Focused Ion Beam Microscope

During the last decade the focused ion beam microscope (FIB) has evolved to an essential tool for the microscopical characterization of materials since it offers capabilities for both imaging and micro-structuring [48]. The working principle is similar to the working principle of a standard scanning electron microscope (SEM): ions are extracted from a source and accelerated by an electric field. Liquid metal ion sources provide the highest brightness and due to the low melting temperature and vapor pressure of gallium most commercially available FIB systems rely on gallium as source material. The ions energies are typically on the order of 5 eV to 30 eV. Using an electrostatic lens system the beam is focused and deflection plates raster the beam over the surface.

The ions interact with the sample material, causing the emission of electrons and, moreover, sample material is removed due to the high mass of the incident ions. For imaging purposes usually the ion-induced secondary electron contrast is used. Crystalline materials show a strong dependence of the ion induced emission of electrons on the crystal orientation and, thus, the ion imaging can be used for identifying grains and grain boundaries. Moreover, the removal of sample material from the surface provides the possibility to precisely machine microscopic structures into the surface. The rate of material removal also depends on the orientation of the crystal.

Imaging and milling procedures result in damage of the material due to incorporation of incident ions, removal of material and local heating. The thickness of the damaged layer depends on the sample material that is exposed to the ion beam and

the intensity of the ion beam. In particular, when micro-mechanical specimens are fabricated the direct exposure of the specimen to the ion beam needs to be limited as far as possible. However, micro-mechanical specimens will be in contact with the incident ions at their side surfaces, which are parallel to the ion beam. The resulting damage layers have a thickness of approximately 10 nm to 50 nm. Therefore, the side surfaces can be machined in several steps with subsequently reduced acceleration voltage. This can significantly reduce the thickness of the damaged layer. For some materials also the chemical interactions need to be taken into account since the ion source material may interact with the sample and alter its properties, e. g. by alloying or by segregation. The influence of such a damaged layer on the mechanical properties of the microscopic specimens is a current topic of scientific investigation [49].

Within this work the FIB has been used for the fabrication of microscopic specimens and for the identification of suitable locations for the fabrication of specimens. A system combining a SEM and a FIB (Nova Nanolab 200, FEI) allows for the preparation and imaging of specimens. The FIB is located at an angle of 52° with respect to the electron beam such that milling and *in situ* imaging without moving the specimen is possible (see figure 3.1). The FIB and the electron beam coincide at a working distance (electron beam) of 5 mm which is also the eucentric hight. The sensitivity of the FIB to differences in the crystallographic orientation is used to image parts of the surface next to suitable positions for the specimen preparation while the location of the specimens are never directly exposed to the ion beam. During the fabrication of the specimens, SEM images are used to adjust the milling process in order to obtain the desired specimen geometry. Since the specimen is never exposed to the incident ion beam, no ion damage is introduced into the specimens with exception of the damage layer at the surfaces of the specimens.

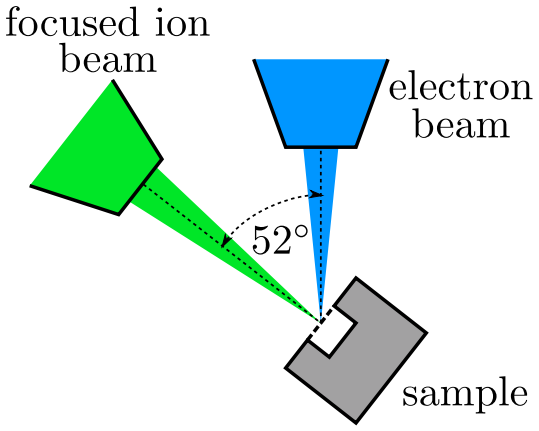

Figure 3.1 Schematic of a combined FIB/SEM system with a sample in the position of the standard milling procedure.

3.2 Operating Principle of the Nanoindenter

Instrumented indentation, or depth-sensing indentation, makes use of indenters which are pressed into the flat surface of the specimen while continuously measuring the load and the displacement. Making use of an analysis of the contact stresses that are present during the loading and unloading of the indenter, several material properties may be determined. For the analysis of the load-displacement data at low indentation depths on the order of micrometers forces on the specimens must be exerted with a resolution on the order of micro newtons and the displacements must be measured with an accuracy in the order of nanometers. Additionally, lateral displacements normal to the indentation axis must be avoided. A system of three components meets all these requirements simultaneously (see figure 3.2). The actuation is realized through a coil that is placed within an annular magnet such that the electric current through the coil is directly proportional to the applied load. Two leaf springs ensure that the applied load acts only in direction of the indentation axis, in particular when contact is made. Finally, the high resolution displacement measurement is realized through a capacitive displacement gauge. The system is originally load controlled since the load is determined by the current through the coil. Displacement control may be achieved through a feedback loop. The phenomenon of thermal drift has to be taken into account, which means that the displacement may vary at a constant force due to thermal expansion or contraction of the loaded assembly. In particular at low loading rates and higher temperatures this can affect the data significantly. To take the thermal drift into account the displacement rate at a constant load can be measured after significant unloading of the specimen. This allows to take the effects of thermal drift into account.

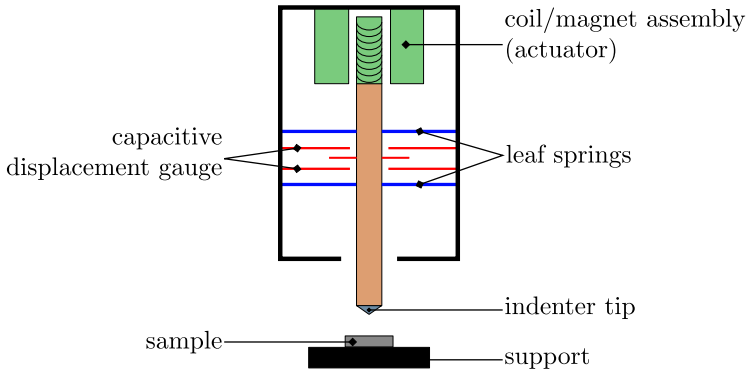

Figure 3.2 Schematic representation of a nanoindentation head.

The analysis of indentation experiments is based on contact mechanics and there has been considerable development in understanding the load-displacement data [4]. Here, only a brief introduction to the analysis of instrumented indentation with sharp indenters is given: Assuming that only elastic deformations are recovered during the unloading of the surface, the initial slope of the unloading curve is re-

garded as the elastic indentation stiffness, S. The elastic indentation stiffness is related to the contact area of the indent, A, by:

$$S = \beta \frac{2}{\sqrt{\pi}} E_{\text{eff}} \sqrt{A} \tag{3.1}$$

where β is a correction factor close to unity which is related to the shape of the indenter and E_{eff} is the effective elastic modulus that takes the deformation of the indentation body into account:

$$\frac{1}{E_{\text{eff}}} = \frac{1-\nu^2}{E} + \frac{1-\nu_{\text{i}}^2}{E_{\text{i}}} \tag{3.2}$$

with the elastic modulus of the indentation body, E_{i}, the Poisson ratio of the indenter, ν_{i} and the Poisson ratio of the material, ν. While the E_{i} and ν_{i} are known, the Poisson ratio of the material is mostly assumed; for metals the characteristic value of 0.3 is often a good estimation. In general, the contact area, A, may be determined by imaging the indents or by calculation from the contact depth of the indent, h, using the area function, $f_{\text{A}}(h)$:

$$\begin{aligned} f_{\text{A}}(h) = A &= \sum_{8}^{n=0} C_n \, h^{\frac{1}{2^{n-1}}} \\ &= C_0 h^2 + C_1 h + C_2 h^{\frac{1}{2}} + C_3 h^{\frac{1}{4}} + \cdots + C_8 h^{\frac{1}{128}} \end{aligned} \tag{3.3}$$

For each tip the constants, $C_0 \ldots C_8$, need to be determined through curve fitting of indentation data from indentation on materials with known material constants. Unfortunately, deviations from the contact area may occur when the material piles up around the indent or when it sinks in. This alters the area function by reducing ("sink-in") or extending ("pile-up") the contact area. In particular in materials with low work hardening capacity pile-up can cause problems in the analysis and needs to be accounted for, e. g. by imaging the indents. The contact area, either measured optically or calculated for the indentation depth, may be used to determine the hardness, H, of the material which is defined as:

$$\mathcal{H} = \frac{P_{\text{max}}}{A} \tag{3.4}$$

where P_{max} is the maximum force exerted on the surface during the experiment. Some empirical relations between the hardness and the yield strength of particular materials (e. g. steels) have been established [50]. However, the hardness is not a fundamental material property but depends on the geometry of the indentation body as well as on the elastic-plastic mechanical behavior of the tested material.

Moreover, dynamic indentation methods have been developed as an addition to the standard methods [3]. During an indentation experiment a harmonic oscillation with a small amplitude is superimposed to the indenter displacement. Comparing the harmonic displacement to the harmonic load the stiffness of the indent may be

determined continuously during an indentation experiment. For materials showing visco-elastic/visco-plastic behavior (e. g. polymers) dynamic indentation methods provide a possibility for investigations into the time and rate dependent material response [10].

As a final note, the indenter stiffness perpendicular to the indentation axis (lateral stiffness of the indenter) has a finite value. This can play an important role in the experimental procedure when the lateral loads on the indenter are not balanced. This is the case for asymmetric loading due to inhomogeneities in the material or an asymmetric indenter tip. The lateral indenter stiffness depends on the displacement of the indenter shaft and is calibrated by the measurement of the lateral forces versus the displacements; i. e. for each indentation depth the lateral stiffness of the indenter is known. Within the present work the lateral indenter stiffness must be taken into account for the cantilever bending/fracture experiments. During these experiments the location of the indent relative to the indentation axis moves due to the deformation of the cantilever. The resistance to this movement must be included in the analysis of the load-displacement data.

3.3 Orientation Measurement by Electron Backscatter Diffraction (EBSD)

When electrons are shot into a conductive material in a scanning electron microscope different interactions can be found. A part of the electrons is scattered elastically, i. e. without loss of their energy. Since these electrons are scattered into all directions, the source of the scattered electrons may be assumed to be a point source within the material. If the material is a crystal, the electron waves emitted from such a source are diffracted by the lattice planes. Thereby, diffraction patterns are formed which may be used to identify the orientation of the crystals relative to a global coordinate system.

In order to use the back scattered and diffracted electrons for the local determination of the crystal orientation the system described in the following has been established (see figure 3.3). The energy of the electrons is typically in a range between 10 eV and 30 eV. A phosphorous screen enables to capture the diffraction pattern of the backscattered electrons. The normal of the screen is placed at an angle of approximately 30° to the surface normal. This type of assembly allows for the measurement in a domain of relatively high total intensities of the back scattered electrons. Making use of a CCD camera the diffraction patters on the phosphorous screen can be captured.

The diffraction patterns form an assembly of bands on the phosphorous screen, where each band represents a lattice plane. The diffraction patterns are used to identify the crystal orientation at the point of the incident electron beam. A Hough transform [51, 52] is used to identify the positions of the bands and their intersections on the screen. Knowing the crystal structure of the sample of interest the orientation of the crystal is determined by comparing the positions and intensities of the peaks in the Hough transform with the expected peaks of an ideal crystal. Using this

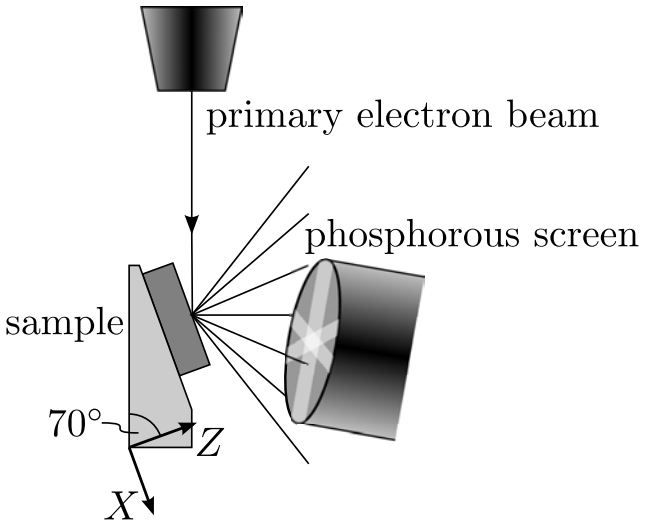

Figure 3.3 Schematic representation of an EBSD system.

information the orientation of the crystal relative to the sample coordinate system as indicated in figure 3.3 is identified. Repeating this procedure at different points of the sample allows to create an orientation map.

3.4 Digital Image Correlation (DIC)

The measurement of local deformations in small dimensions requires techniques which provide an adequate resolution of the displacement fields. The Digital Image Correlation (DIC) is capable of contactless capturing of such displacement fields from pixel based images, thus, without affecting the measurement in any way [53]. The DIC algorithm takes two greyscale images as input: the reference picture and the actual picture of the deformed structure. Characteristic subsets of pixels are identified in both pictures and the displacement fields can be calculated from the relative difference in positions. Hence, the native units of the measurement are pixels such that the DIC algorithm is scale independent. However, sufficiently contrasted images providing distinguishable characteristic subsets of pixels are required to apply the DIC algorithm. This is usually achieved by applying an irregular speckle pattern if the surface of interest does not provide enough contrast.

In a first step, both images are divided into subsets of pixels which accurately represent the structure of the irregular speckle pattern. Making use of a bi-cubic interpolation algorithm the images are smoothed, enabling for a sub-pixel resolution in the order of 10^{-2} pixel. Bi-cubic interpolation is used since it generally provides a well-balanced relation between computation time and accuracy. The relative displacement and the deformation of each subset are determined by finding the location of the subset in the actual image where the correlation coefficient reaches a maximum value. This correlation coefficient depends on the location, (x, y), of the subset taken from the actual image and thus on the displacement of the center of

the subset, (u, v). The calculation of the position of each point within the subset additionally requires the derivatives $\frac{\partial u}{\partial x}$, $\frac{\partial v}{\partial y}$, $\frac{\partial u}{\partial y}$ and $\frac{\partial v}{\partial x}$ at the center of the subset. Various iteration methods may be used to determine the displacement and the respective derivations to find the maximum of the correlation coefficient, e. g. the Newton-Raphson method which provides good accuracy at acceptable computation times [54]. The software used within the present work is a free software available at [55].

Making use of the DIC-method it is possible to determine two dimensional displacement and strain fields on a surface. The strain terms result from the derivation terms at each subset center. In order to apply the method for investigations into the deformation of microstructural components it is necessary to create a sufficiently contrasted surface. The problem to create a speckle pattern in this dimensions will be addressed in chapter 6. Moreover, a suitable resolution of the images is required to achieve a sufficient accuracy to apply the DIC-method.

4 Experimental Test Setup for Fracture Experiments on Single Grain Boundaries

The investigation of the initiation and propagation of interfacial cracks at single grain boundaries requires the application of novel experimental techniques on the microscopic scale. In this chapter the experimental challenges for quantitative fracture experiments of individual grain boundaries are specified. First, the aluminum-lithium alloy AA2198 is introduced as a model material for the development of a method for separation of single grain boundaries. An experimental testing protocol is established together with a data analysis procedure which necessitates the introduction of corrections. Finally, a finite element framework is established that provides the possibility of comparing specimens with differences in their geometry.

4.1 Choice of AA2198 as a Model Material

The aluminum-lithium alloy AA2198 was chosen as a model material for the development of a single grain boundary separation method. Aluminum-lithium alloys are interesting materials for investigations into the separation properties of single grain boundaries since intergranular fracture is known to reduce the fracture resistance of these alloys [1]. An understanding of the mechanisms that lead to intergranular fracture is fundamental for the prediction of the macroscopic fracture properties. The concept of strain localization at or in the vicinity of the grain boundaries provides an explanation for the susceptibility of these such alloys to intergranular fracture [2, 56, 57]. Severe strain localizations may be caused by precipitate free zones adjacent to the grain boundaries as well as by precipitates on the grain boundaries. Such strain localizations lead to the nucleation and growth of voids which finally cause failure of the grain boundary. It has been shown that the structure of the grain boundaries determines the fracture mode between transgranular and intergranular failure rather than the ductility of the matrix [58, 59].

As described in section 4.2, focused ion beam (FIB) milling with a gallium liquid metal ion source has been used for the preparation of the specimens. Since gallium is known to embrittle grain boundaries in aluminum and its alloys, the analysis of the micro-mechanic processes that cause the failure of the grain boundaries is limited. However, the understanding of fracture processes which involve the combination of brittle grain boundaries and ductile grains provides an important challenge.

Rolled sheets of the material were provided by ALCAN in the temper T351 which is also called “underaged”. A heat treatment to obtain the temper T8 was carried

out on some of the sheets; this temper is also called "peak-aged". The macroscopic yield stress and the ultimate tensile strength have been determined from tensile tests in the rolling and the transversal direction. The results of these tests are listed in table 4.1. The peak-aged material shows a higher yield stress and ultimate tensile strength, as expected. Additionally, nanoindentation experiments with a Berkovich indenter have been carried out to determine the microscopic hardness of the alloy. The results averaged over 25 indentations for each heat treatment are listed in table 4.2. The increase of the hardness of the peak-aged material compared to the hardness of the under-aged material is in good agreement with the increase of the yield stress and the ultimate tensile strength measured from the tensile experiments. Cavaliere and de Santis [60] determined the elastic modulus from tensile tests as 74.3 GPa for the transversal direction and 76.7 GPa for the longitudinal direction. However, other values of the elastic modulus have been reported in the range between 71 GPa [61] and 78 GPa [62]. The actual elastic modulus of the material is needed for the crystal plasticity model used in chapters 5 and 6. However, the elastic deformation plays a minor role for these experiments such that it is reasonable to assume an elastic modulus of 75 GPa for the following investigations.

temper	yield stress , MPa	UTS , MPa
T351-L	324	445
T8-L	470	511
T351-T	294	416
T8-T	449	490

Table 4.1 Yield stress and ultimate tensile stress of the aluminum lithium alloy AA2198 from macroscopic tensile tests.

temper	Hardness , GPa
T351-T	1.322 ± 0.041
T8-T	1.602 ± 0.069

Table 4.2 Hardness of the aluminum lithium alloy AA2198 measured by Berkovich indentation.

The microstructure of the material was revealed by polishing and subsequent etching, using Barker's etch and observation under polarized light (see figure 4.1). The polishing procedure is described in table 4.3. The grains are elongated in the rolling direction and flat respective to the thickness direction of the sheet. In particular, the grain boundaries are flat which is a great advantage for the bending experiments to determine the interfacial strength. In the rolling direction the length of the grains is generally larger than 300 µm while the grain size in the transversal

direction is between 100 and 300 µm. The thickness of the grains ranges between 1 and 10 µm with an average thickness of about 3 µm.

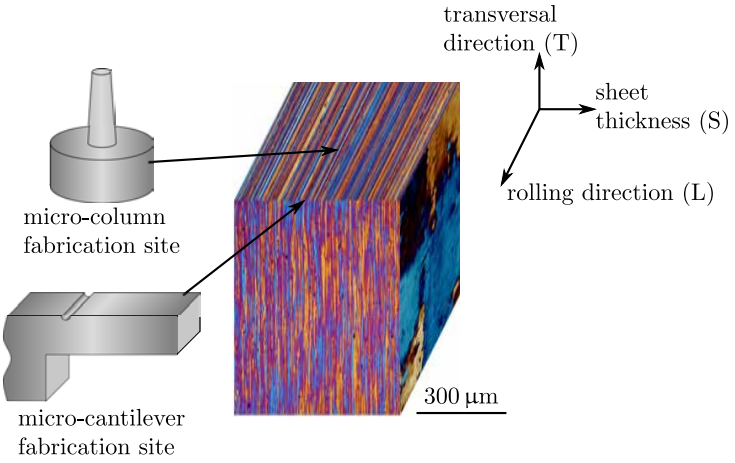

Figure 4.1 Microstructure of the AA2198 sheets after Barker's etch ($HBF_4 + H_2O$, anodized using 0.2 A/cm^2), observed in polarized light.

Type	Grain size	Time
SiC	500	1 min
SiC	800	1 min
SiC	1000	1 min
SiC	1200	1 min
SiC	2500	1 min
Diamond	3 µm	3 min
OPS	0.05 µm	3 min

Table 4.3 Polishing procedure for AA2198.

4.2 Fabrication of Notched Cantilever Specimens

As pointed out in chapter 2, micro-bending experiments on specimens with dimensions on the order of several micrometers have been carried out by various researchers to determine material properties of both thin films on a substrate and bulk materials. Furthermore, micro-cantilever specimens have been found to provide the most promising approach for microscopic fracture tests. Within this work a cantilever bending and fracture test has been established for investigations into the fracture properties of single grain boundaries.

Cantilevers with a rectangular cross-section were prepared using FIB milling with a gallium ion source. A rectangular cross section was chosen in order to maintain a constant crack width. To achieve such a geometry, the specimens were fabricated

from a near edge region of the sample in order to minimize the amount of material to be removed by the FIB milling process. Both surfaces forming the edge had been polished prior to the fabrication process according to the procedure described in table 4.3. Using orientation contrast images achieved with the ion beam, a suitable grain boundary was found and placed in a distance of approximately 2 µm from the supported end of the cantilever. Only the regions adjacent to the cantilever were scanned such that the cantilever was never directly exposed to the ion beam. The selected boundary was marked by a line pattern outside the cutting area to identify the position of the boundary during the cantilever fabrication process. The orientations of the grains included in the cantilever were determined using the EBSD technique. In particular the orientations of the grains adjacent to the grain boundary were important for the further analysis presented in chapter 6 since this is the location of the highest deformation and, moreover, the orientations can be used to characterize the grain boundary.

Using a relatively high beam current (e. g. 7 nA) a trench of material was removed from each side adjacent to the cantilever (figure 4.2(a)), leaving sufficient space for subsequent cuts to release the cantilever from below (see figure 4.2(b)). Subsequent milling was conducted at lower currents in the range of 1 nA down to 0.1 nA for the final surface milling. After the cantilever had been prepared, a U-notch was made using FIB milling from one side of the cantilever at the location of the grain boundary. The notch ensures that the selected boundary serves as the primary failure site during testing by avoiding high tensile stress concentrations in the support. The blunt shape of the notch is favorable since the boundary edge may not be perfectly straight, which would prevent the fabrication of a sharp artificial crack directly at the boundary. Lastly, the well defined shape of the notch circumvents any ambiguities associated the finite element analysis, as will be discussed later. In the work presented here, the nominal dimensions of the final cantilever are approximately 20 µm × 5 µm × 5 µm (length × width × height). A representative cantilever is shown in figure 4.3.

4.3 Cantilever Bending Experiments

The bending experiments were carried out using a nanoindenter (Nanoindenter XP, Agilent) equipped with a Berkovich tip. This tip is used since it is sufficiently sharp to create visible indents on the cantilevers such that the bending length, L, of the cantilever from the supported end to the contact point for loading could be determined. Also, the lateral position of the indent could be identified for further analysis. Moreover, the use of a sharp tip largely avoided the problems associated with a wedge or cylindrical contact, where misalignment at the contact would create torque.

During the experiment, the cantilever was loaded at a constant displacement rate. A typical loading profile during an experiment is shown in figure 4.4. In order to monitor the onset and propagation of damage, multiple partial unloads were employed for stiffness measurements; a decrease in the elastic stiffness was associated

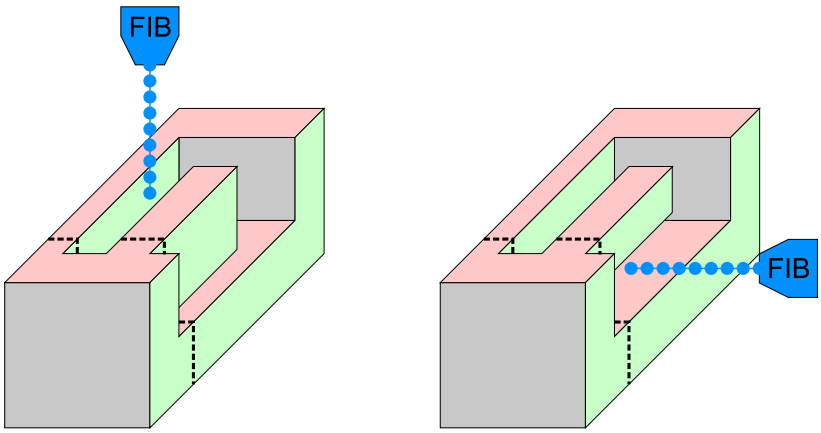

(a) First milling process **(b)** Second milling process

Figure 4.2 Preparation of a cantilever from the edge of a sample.

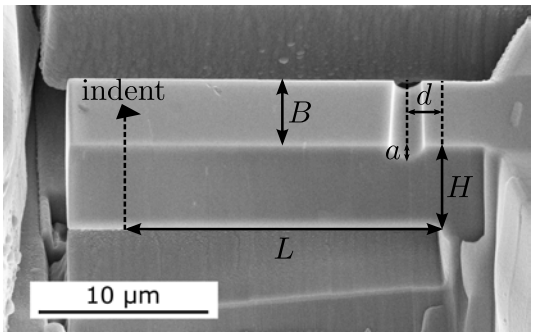

Figure 4.3 SEM image of a cantilever with characteristic dimensions. The dashed line represents a grain boundary. L is the bending length, B is the cantilever width, H is the height of the cantilever, a is the depth of the notch and d is the distance of the notch center to support.

with the presence of damage or crack initiation. Assuming small changes in geometry due to plastic deformation, plasticity did not affect the unloading stiffness. While both the unloading and reloading data may be used to determine the stiffness, here the reloading data was used for the stiffness analysis. Additionally, the stiffness of the cantilever was determined by the continuous stiffness method (CSM); the stiffness was measured by superimposing an oscillation with a small displacement amplitude of 2 nm to the loading procedure.

4.4 Corrections to the Experimental Data

While the applied load, P, is measured directly, the total displacement, h_{raw}, is comprised of the deflection of the cantilever beam, w, and the indentation depth, h^{ind}, as shown in 4.5(a). Figure 4.5(b) gives a schematic representation of the experiment

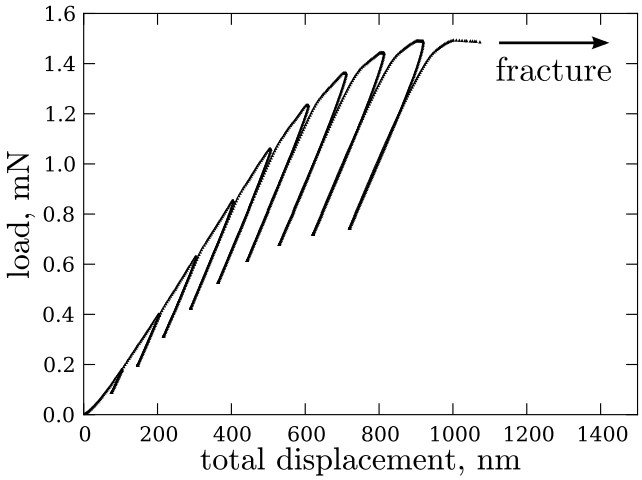

Figure 4.4 Load-displacement data from a typical micro-bending experiment.

illustrating the correction to be applied to the raw data. During the loading segment the indentation depth into the cantilever, $h^{\mathrm{ind}}(P)$, is approximated by the indentation depth associated with a standard indentation experiment conducted in the bulk material at the same load. Hence, a reference curve was measured from indentation experiments in the bulk material at loads up to the maximum load measured for the bending experiments. The deflection of the cantilever alone during loading, w_{l}, is expressed as:

$$w_{\mathrm{l}}(P) = h_{\mathrm{raw}}(P) - h^{\mathrm{ind}}(P). \tag{4.1}$$

It is worth noting that when the cantilever is deflected the indentation surface is no longer normal to the indentation axis. However, the cantilever deflections presented in this work do not exceed 10 % of the bending length, leading to a maximum inclination of the cantilever-axis at the contact point of approximately 6°. The effect of the inclination of the cantilever surface is neglected within the correction.

During the unloading and reloading segments the correction shown in equation (4.1) cannot be applied, due to partial elastic recovery of the indent. In order to correct for the deflection of the cantilever during unloading and reloading the indentation depth must be decomposed into a plastic part, $h_{\mathrm{pl}}^{\mathrm{ind}}$, and an elastic part, $h_{\mathrm{el}}^{\mathrm{ind}}$:

$$h^{\mathrm{ind}} = h_{\mathrm{pl}}^{\mathrm{ind}} + h_{\mathrm{el}}^{\mathrm{ind}}. \tag{4.2}$$

During the un- and re-loading of the cantilever the plastic indentation depth is constant whereas the elastic indentation depth varies. The correction of the deflection during un- and re-loading is given by:

$$w_{\mathrm{r}}(P) = h_{\mathrm{raw}}(P) - h_{\mathrm{pl}}^{\mathrm{ind}}(P_{\mathrm{max},i}) - h_{\mathrm{el}}^{\mathrm{ind}}(P), \tag{4.3}$$

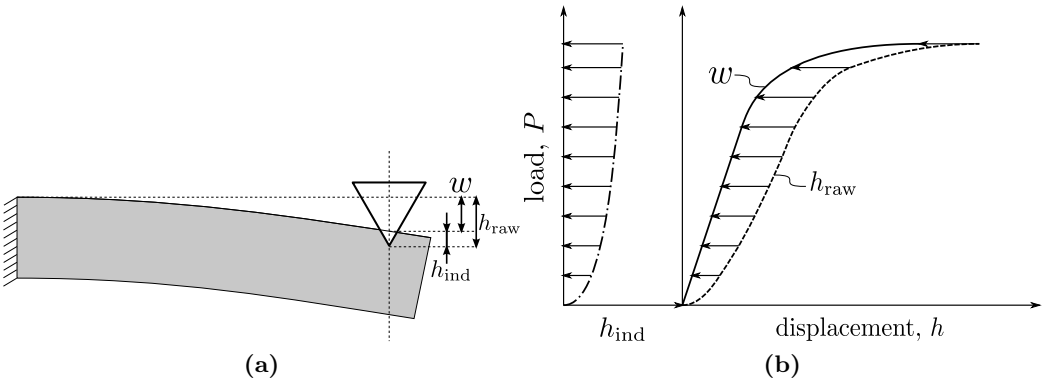

Figure 4.5 (a) Schematic representations of the decomposition of the total measured displacement, h_{raw}, the cantilever deflection, w, the indentation depth, h^{ind}, and (b) the correction of the raw data for the indentation depth.

where the plastic indentation depth at the previous maximum is calculated as:

$$h_{\mathrm{pl}}^{\mathrm{ind}}(P_{\mathrm{max},i}) = h^{\mathrm{ind}}(P_{\mathrm{max},i}) - h_{\mathrm{el}}^{\mathrm{ind}}(P_{\mathrm{max},i}). \tag{4.4}$$

In order to determine the elastic indentation depth, $h_{\mathrm{el}}^{\mathrm{ind}}(P)$, the elastic indentation stiffness, S, of the material was determined from bulk indentation experiments. The indentation stiffness is a function of the maximum indentation depth or equivalently the maximum applied load: $S := S(P)$. Either the use of multiple unloading segments or continuous stiffness measurements during indentation into the bulk can provide the indentation stiffness as a function of the load, as needed for the correction. The elastic indentation depth is calculated as:

$$h_{\mathrm{el}}^{\mathrm{ind}}(P) = \frac{P}{S(P_{\mathrm{max},i})}. \tag{4.5}$$

The actual experimental stiffness of the cantilever, K_{beam}, is calculated from the slope, $\frac{\mathrm{d}P}{\mathrm{d}w}$, of the corrected reloading segments.

Finally, the elastic indentation depth also influences the dynamic measurement of the stiffness by the CSM. In order to separate the continuous stiffness of the cantilever, $K_{\mathrm{beam}}^{\mathrm{CSM}}$, from the stiffness of the indent, $S_{\mathrm{indent}}^{\mathrm{CSM}}$, the stiffness of the system, $K_{\mathrm{sys}}^{\mathrm{CSM}}$, is modeled by two springs connected in series:

$$\frac{1}{K_{\mathrm{sys}}^{\mathrm{CSM}}} = \frac{1}{S_{\mathrm{ind}}^{\mathrm{CSM}}} + \frac{1}{K_{\mathrm{b}}^{\mathrm{CSM}}}. \tag{4.6}$$

By rearranging (4.6) we find an expression for the continuous stiffness of the cantilever alone:

$$K_{\mathrm{b}}^{\mathrm{CSM}}(P) = \frac{S_{\mathrm{ind}}^{\mathrm{CSM}}(P) \cdot K_{\mathrm{sys}}^{\mathrm{CSM}}(P)}{S_{\mathrm{ind}}^{\mathrm{CSM}}(P) - K_{\mathrm{sys}}^{\mathrm{CSM}}(P)}. \tag{4.7}$$

In order to determine the harmonic indent stiffness as a function of the applied load, indentation experiments using the CSM method were carried out in the bulk, up to the maximum load used in the bending experiments. In particular, at low indentation depths ($h^{\mathrm{ind}} < 100\,\mathrm{nm}$) the variation of the elastic indentation depth cannot be neglected. Without considering the change in $h^{\mathrm{ind}}_{\mathrm{el}}$, the slope of the unloading and reloading curves would be smaller than associated with the beam alone; leading to inaccurate stiffness calculations. The errors in the stiffness associated with the first reloading segments would be particularly large since the elastic indentation stiffness is lowest at small depths. It is worth noting, that the stiffness of the cantilever alone as calculated from equation (4.7) tends to infinity when $S^{\mathrm{CSM}}_{\mathrm{ind}}(P)$ approaches $K^{\mathrm{CSM}}_{\mathrm{sys}}(P)$. However, a typical stiffness measured in an experiment $K^{\mathrm{CSM}}_{\mathrm{sys}}(P)$ is $3000\,\mathrm{N/m}$. This value of $S^{\mathrm{CSM}}_{\mathrm{ind}}(P)$ is achieved at a load of approximately $5\,\mu\mathrm{N}$. Therefore, this case has no practical impact on the measurements.

Calibration Curves for the Indentation Depth Correction

The correct determination of the cantilever deflection requires the indentation depth into the cantilever as a function of the load, $h^{\mathrm{ind}}(P)$. This correction function needs to be determined experimentally for each combination of indenter tip and material. For the cantilever bending experiments a Berkovich tip was used, with the correction factor $\beta = 1.034$. Typical loads in the cantilever bending experiments were on the order of 2 mN, leading to indentation depths of 200 nm with a Berkovich tip. The corresponding size of the indent was on the order of 1 µm. Since this is only 20 % of the width of the cantilevers, it is reasonable to approximate the indentation depth into the cantilever by evaluating the indentation depth into the bulk material at low loads.

The load-displacement curves for the indentation experiments were established up to loads of 2.5 mN which are the highest loads measured during the bending experiments. Five indentation experiments were carried out for each temper. The displacement rate for these experiments was set to 10 nm/s. For a Berkovich tip the area function is dominated by the square of the indentation depth. Therefore, assuming that the materials hardness is constant, the load-displacement data is expected to follow a square function of the type:

$$P = a\left(h^{\mathrm{ind}}\right)^2 + b\,h^{\mathrm{ind}}. \tag{4.8}$$

The linear term is introduced to account for deviations from the tip geometry from an ideally sharp tip. The constants a and b are determined from a fitting procedure of the load-displacement data for the whole set of experiments. Rearranging (4.8) provides the desired correction:

$$h^{\mathrm{ind}}(P) = \sqrt{\frac{P}{a} + \frac{b^2}{4\,a^2}} - \frac{b}{2\,a}. \tag{4.9}$$

temper	a, GPa	b, kN/m	c, mm^2/N	d, µm
T351	38.7	0.593	0.149	0.474
T8	43.7	0.533	0.177	0.270

Table 4.4 Fit constants for the correction functions presented in equation (4.8) and (4.11).

The elastic stiffness of the indent also increases with increasing load. This correction was determined by indentation experiments in the bulk material, as well. The elastic indent stiffness, $S(P)$, was determined by making use of the continuous stiffness method. Five measurements using CSM were carried out for each temper of the alloy. The maximum indentation load was 2.5 mN and the displacement rate was set to 10 nm/s.

Assuming that the hardness is constant at each indentation depth (3.4) results in:

$$A = \frac{P}{\mathcal{H}}. \tag{4.10}$$

Replacing the indent area, A, in equation (3.1) by this expression, a function of the square root type for the stiffness versus the indentation load is suggested. Using the same method as described before, the indentation load, P, is fitted as a function of the elastic stiffness of the indent, S, assuming:

$$P = c\,S^2 + d \cdot S, \tag{4.11}$$

where the linear term is introduced to account for deviations of the indenter tip. However, the indentation stiffness versus load data is dominated by the quadratic term. The correction is provided by rearranging (4.11):

$$S(P) = \sqrt{\frac{P}{c} + \frac{d^2}{4\,c^2}} - \frac{d}{2\,c}. \tag{4.12}$$

It is worth noting that the indent stiffness depends on the loading history, such that the maximum load applied to the indentation site determines the elastic stiffness of the indent. The elastic indent stiffness as a function of the depth is also used for the correction of the cantilever stiffness measured from the continuous stiffness method by equation (4.7), i. e. $S_{\mathrm{ind}}^{\mathrm{CSM}}(P) := S(P)$.

4.5 Methods for the Measurement of the Cantilever Stiffness

In order to determine if the grain boundary of interest is subject to damage it is necessary to measure the elastic stiffness of the cantilever; a loss of elastic stiffness is associated with the occurrence of damage (e. g. [63]). By measuring the stiffness continuously during the loading procedure the load and the displacement at the

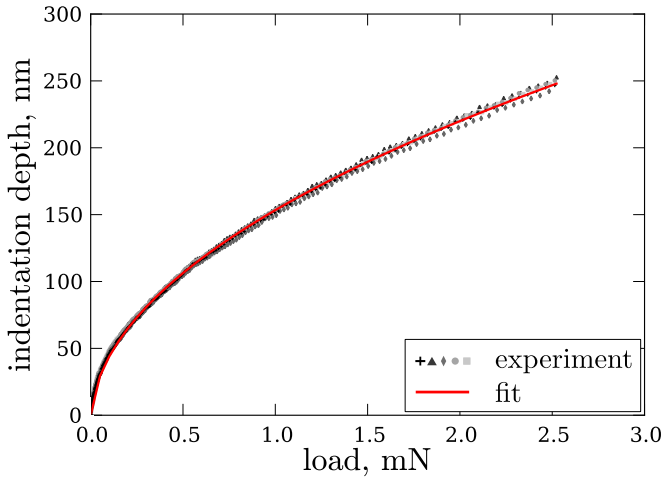

(a)

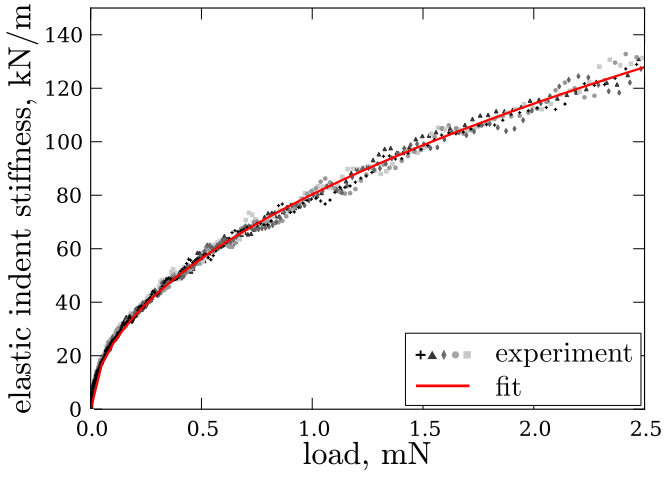

(b)

Figure 4.6 Calibration curves for (a) the indentation depth and (b) the elastic indent stiffness versus the load.

point of initiation of damage can be determined and it is possible to observe the propagation until complete failure.

In order to measure the elastic stiffness of the cantilever at each instant, the CSM method is favorable. However, it must be verified that the stiffness of the cantilever and the stiffness measured from the slope of the reloading segments are of the same value. For two of the specimens the indenter was unloaded every 200 nm of displacement to 50 % of the maximum load while a continuous stiffness measurement was carried out. The harmonic frequency for the measurement was set to 45 Hz and the harmonic displacement was fixed at 2 nm.

The stiffness data is presented in figure 4.7 where both the harmonic stiffness and the stiffness measured from the unloading segments are plotted against the cantilever deflection. The geometry of the cantilevers is given in table 4.5. The CSM-data shows scatter of approximately 15 % around its average value. At deflections up to 100 nm the harmonic stiffness increases until it attains a constant average value. This is likely due to deviations from the correction given in equation (4.7) at very low indentation depths until full contact is established. The stiffness measured from the reloading segments deviates from the mean value by approximately 5 %, which shows that both methods are sufficiently accurate for the measurement of the cantilever stiffness. Figure 4.7(a) shows a specimen where the stiffness remains approximately constant until the point of failure. In figure 4.7(b) a specimen is shown where the stiffness decreases significantly before failure. Both methods were able to capture this decrease of the cantilever stiffness. It is worth noting that the decrease of the stiffness, as shown in figure 4.7(b), is atypical for specimens of both tempers investigated in this work. As pointed out later, the grain boundaries mostly fail without significant loss of the structural stiffness prior to fracture. This is consistent with the expectation that the grain boundaries are embrittled due to the gallium that is used during the fabrication process.

4.6 Finite Element Framework for Normalization

In order to compare the load-displacement data between specimens that have different geometries a normalization technique is required. Due to the complex geometry of the specimens involving the U-notch and the compliant support, finite element modeling was used. Making use of an isotropic linear elastic constitutive law, specimens with different geometries were compared in terms of the cantilever stiffness and load.

For each specimen a finite element model was created to include the specific geometry, as shown in figure 4.8. The main features of the geometry are: the bending length, L, defined from the supported end of the cantilever to the location of the indent; the width, B; the height, H; the distance, d, from the supported end to the center of the notch; the notch depth, a; and the notch radius, R. Additionally, the cantilever support was explicitly modeled.

In order to create the FE-models, the finite element code ABAQUS was employed. Eight-node brick elements were used to mesh the model except within the

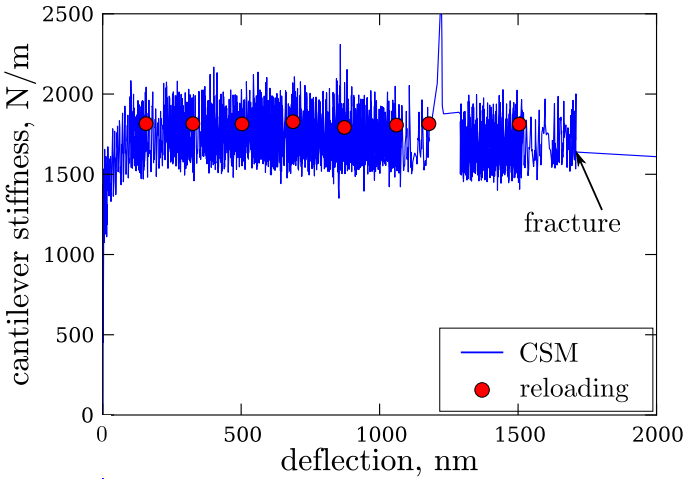

(a)

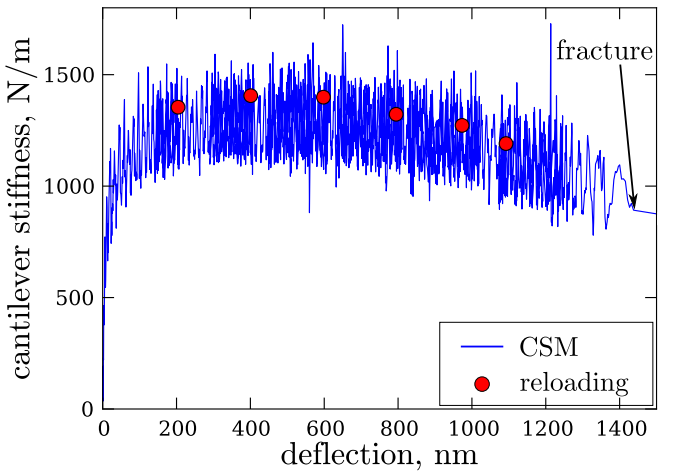

(b)

Figure 4.7 Elastic cantilever stiffness measurements of cantilevers with (a) constant stiffness (CB-8) and (b) decreasing stiffness prior to fracture (CB-9). The stiffness measured from reloading segments (red dots), the elastic cantilever stiffness measured by CSM (blue curve) are given for the corrected datasets.

transition zone adjacent to the notch (see figure 4.8) where six-node wedge elements were employed to reduce the mesh size. Fixed boundary conditions were imposed on the surfaces at the bottom of the support as well as on its back surface. The elastic modulus of the material at the loading point was 10^6 GPa in order to prevent severe distortions of the elements. The resulting high contact stiffness negates the need for any indentation correction in the finite element analysis; the displacement in the simulation equals the cantilever deflection, w. The deflection in the simulation is given by a displacement boundary condition at the loading point.

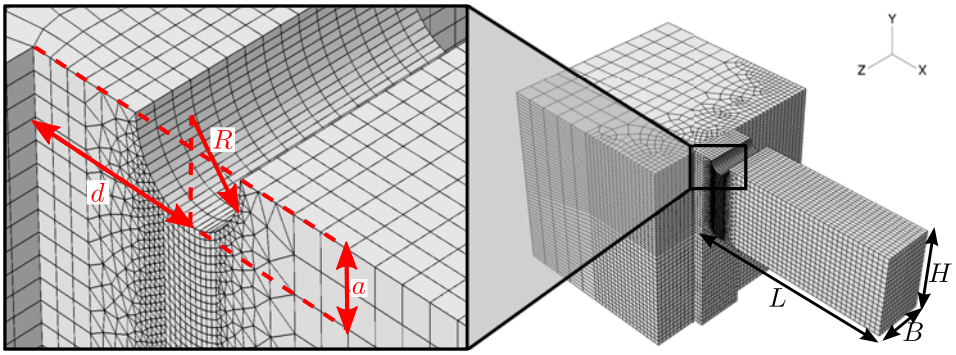

Figure 4.8 Finite element model of a micro-cantilever. The geometric features given are the bending length, L, the width, B, the height, H, the position of the notch center, d, the notch depth, a and the notch radius, R.

The indenter shaft provides a lateral stiffness which necessitates an additional boundary condition in the finite element model to correctly describe the experiment. The lateral stiffness of the nanoindenter depends on the position of the indenter tip relative to the load frame (see figure 4.9). For each experiment the lateral stiffness was introduced into the finite element model using two linear spring elements at the loading point.

For an estimation of the cantilever stiffness a linear elastic isotropic material model was used. The elastic modulus in the simulation, E^{sim}, is chosen as 75 GPa, and a Poisson ratio of $\nu = 0.33$ is assumed. Using these isotropic elastic constants, the stiffness, K^{sim}, of the structure was computed for each specimen. Assuming that the deflection is small compared to the bending length of the cantilever, a linear law relates the deflection, w, to the load, P, by a constant stiffness, K^*:

$$P = K^* w. \tag{4.13}$$

All geometric features may be reduced to one single value with a dimension of length which we call the characteristic length, $\hat{l}$:

$$\hat{l} = \frac{K^{\text{sim}}}{E^{\text{sim}}}. \tag{4.14}$$

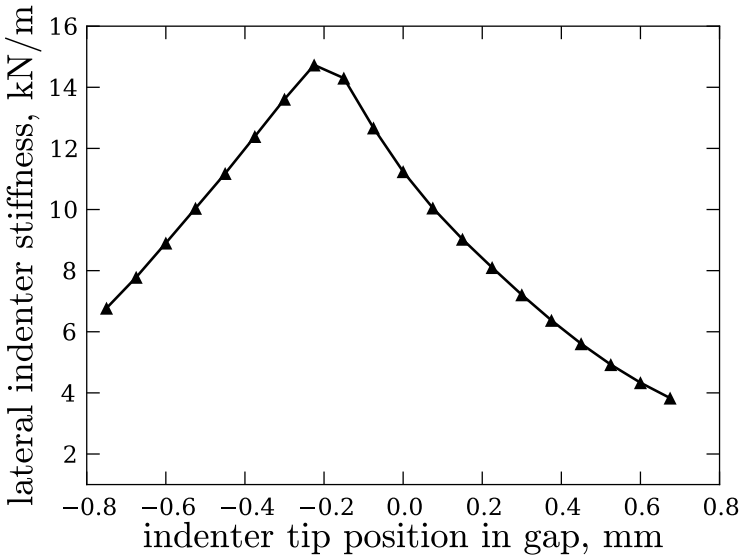

Figure 4.9 Lateral stiffness of the indenter as a function of the position of the indenter tip relative to the load frame.

While the FE-model used here is for linear elastic behavior, it is not expected that the plasticity occurring during the actual experiments limits the applicability of the characteristic length for the normalization; in all cases the stiffness of interest results from elastic deflections, and the permanent shape change resulting from plasticity is small.

In the absence of damage we obtain:

$$P = K^{\exp} w_{\mathrm{r}} = E \hat{l} w_{\mathrm{r}}. \tag{4.15}$$

A normalized load, $\hat{P}$, and a normalized stiffness, $\hat{K}$, are computed by dividing the load and the stiffness by the characteristic length associated with the specimen geometry:

$$\hat{P} = \frac{P}{\hat{l}} \tag{4.16}$$

$$\hat{K} = \frac{K^{\exp}}{\hat{l}}. \tag{4.17}$$

However, for a laterally constrained indenter the characteristic length depends on the elastic modulus chosen for the simulation, E_{sim}, as can be seen in figure 4.10. Therefore, the normalization approach may not be readily used to determine an unknown elastic modulus.

For the normalization linear elastic isotropic material behavior is assumed. Since oligo-crystalline cantilevers are tested, involving approximately ten grains in the deformation process, the influence of the elastic anisotropy of the single grains has been estimated. Simulations of single crystalline cantilevers with the crystallographic axes [1 1 1] and [1 0 0] taken as the cantilever axis have been carried out.

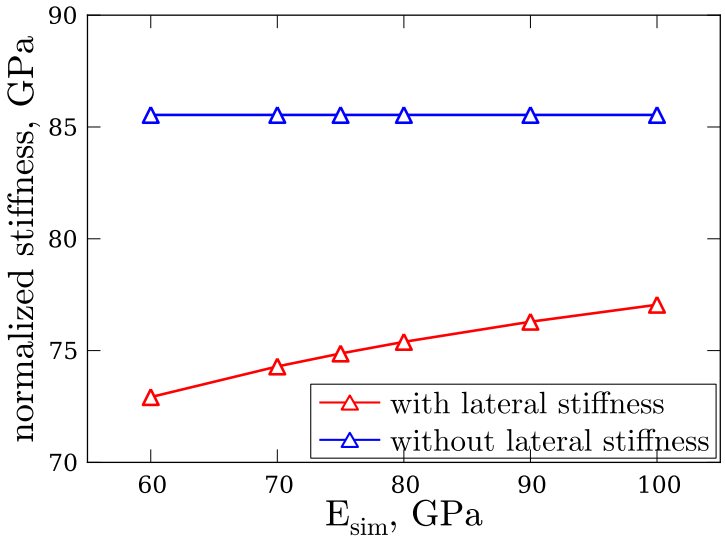

Figure 4.10 Normalized stiffness as a function of the elastic modulus chosen for the simulation for a laterally unconstrained and a laterally constrained indenter.

For these simulations an anisotropic elastic material model with cubic symmetry was applied. The cantilever with the [1 1 1] crystal orientation provides the highest elastic modulus in the direction of the cantilever axis, while the [1 0 0] orientation provides the lowest elastic modulus.

Assuming that the anisotropy of the aluminum crystals is preserved the elastic constants for the single crystal can be estimated. For pure aluminum the elastic constants in Voigt notation are given as [64]: $C_{11} = 108\,\text{GPa}$, $C_{12} = 61\,\text{GPa}$ and $C_{44} = 29\,\text{GPa}$. In order to determine a scaling factor, ξ, the isotropic elastic moduli of pure aluminum and AA2198 were compared to each other. The isotropic elastic modulus of the alloy is taken to be 75 GPa [60]. Pure aluminum has an isotropic elastic modulus of 70 GPa. Hence ξ is calculated:

$$\xi = \frac{E_{\text{AA2198}}}{E_{\text{pure Al}}} = 1.071. \tag{4.18}$$

The elastic constants for AA2198 are approximated as:

$$\begin{aligned} C_{11}^{\text{AA2198}} &= \xi\, C_{11}^{\text{Al}} = 115.7\,\text{GPa} \\ C_{12}^{\text{AA2198}} &= \xi\, C_{12}^{\text{Al}} = 65.3\,\text{GPa} \\ C_{44}^{\text{AA2198}} &= \xi\, C_{44}^{\text{Al}} = 31.1\,\text{GPa}. \end{aligned} \tag{4.19}$$

The simulations show that the deviations from the cantilever stiffness in a isotropic specimen with the same geometry do not exceed 10 %. These simulations of single crystals can be seen as a worst case where the elastic anisotropy of the single

grains is most important. Since multiple grains are involved in the deformation of the specimens which have been investigated here elastic isotropy is assumed for the analysis.

4.7 Experimental Evaluation of Damage Initiation and Propagation

SEM images were taken from each tested specimen to determine the location where the cantilevers were deformed, damaged or fractured. In most cases the cantilevers failed – as desired – at the chosen grain boundary as shown in figure 4.11. In a few cases the cantilevers failed at grain boundaries at the support or multiple grain boundaries failed during the test. Particularly stable grain boundaries or a badly positioned notch can cause such a behavior when the stress to separate the grain boundary is not achieved. The analysis of the fracture parameters of the single grain boundary is considered in section 6.

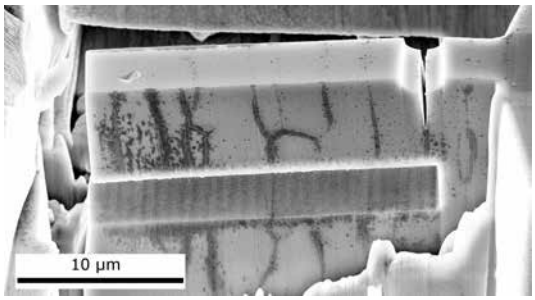

Figure 4.11 Cantilever after the fracture test. The grain boundary under the U-notch failed as desired.

For cantilevers of each temper the development of the stiffness during the bending experiments was determined. The loading of the cantilevers was performed at a constant loading rate of 5 nm/s. Every 100 nm of displacement the indenter was unloaded to 50 % of the maximum load for the determination of the stiffness. The load-displacement data is then normalized through the procedure given in section 4.6 including the lateral stiffness of the indenter in order to compare the cantilevers to each other.

The experimental data of two cantilevers of each temper is shown here for comparison. The geometry for of the cantilevers is given in table 4.5. The load versus deflection data is shown in figure 4.12(a). The elastic stiffness, i. e. the slope of the reloading segments, differs significantly between the specimens due to differences in the geometry. Making use of the FE-based normalization procedure these differences are largely eliminated, as shown in figure 4.12(b). Furthermore, the normalized stiffness is shown not to differ significantly between different specimens.

The normalized stiffness also refers to the elastic deformation of the specimen and can be used to monitor the initiation and propagation of a crack. The accumulated

damage of the cantilever depends on the deformation history which is represented by the maximum deflection of the cantilever at each instant. Hence, in order to compare the evolution of the stiffness for different specimens, the slopes of the reloading segments are plotted against the deflection of the cantilever at the beginning of the corresponding unloading segment. In figure 4.13 the cantilever stiffness is plotted for specimens of both tempers. Generally, no significant decrease of the normalized stiffness can be found with increasing deflection of the cantilever indicating brittle boundaries. As soon as the critical load or deflection for the initiation of a crack is attained, the grain boundary fails without stable crack propagation. Since no significant loss of elastic stiffness occurs prior to specimen failure, the nonlinearity in the normalized force is solely attributed to plastic deformation.*

Specimen	temper	H µm	L, µm	B, µm	a, µm	d, µm
CB-1	T8	6.43	24.46	6.05	0.8	3.0
CB-2	T8	8.89	24.8	5.14	0.64	4.71
CB-3	T8	9.07	21.9	5.82	0.88	4.55
CB-4	T8	9.43	25.23	5.57	1.05	3.20
CB-5	T351	6.48	17.43	7.11	1.01	2.13
CB-6	T351	6.46	19.03	5.72	1.07	2.91
CB-7	T351	6.84	18.40	4.31	1.09	1.28
CB-8	T351	7.28	24.99	7.69	1.24	4.12
CB-9	T351	8.33	23.18	5.81	1.6	5.90

Table 4.5 Geometry of the tested cantilever specimens. The geometric features given are the bending height, H, the bending length, L, the width, B, the notch depth, a and the position of the notch center, d. The notch radius for all specimens was 1 µm.

While it has already been stated that the plastic deformation of the specimen does not affect the applicability of the linear elastic model for the normalization of the load and the stiffness, this model cannot predict the stress fields in the cantilever at the point of failure. In order to overcome this limitation, the linear elastic constitutive law must be replaced by an appropriate constitutive model that includes plastic deformation. This is presented in chapter 5.

4.8 Morphology of the Crack Tip and the Crack Surface

In addition to the load-displacement response, the tested specimens were observed by high resolution electron microscopy. The crack tips and the fracture surfaces are of particular interest for studies of interfacial failure. Such observations provide insight into the mechanisms of grain boundary failure. While the usefulness of a

*It is worth noting that in very few cases a decrease of the stiffness is found prior to fracture. These samples have not been included for the further analysis presented in chapter 6.

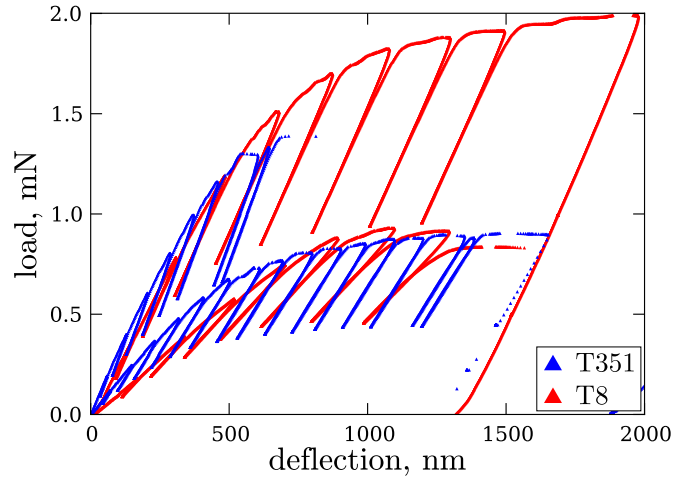

(a)

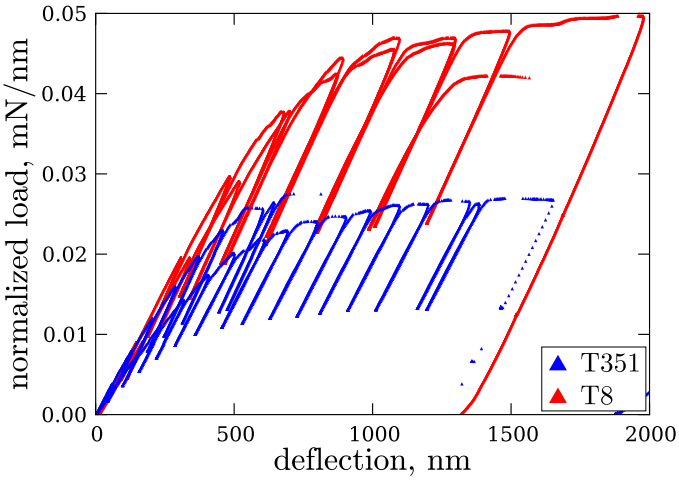

(b)

Figure 4.12 (a) load-deflection curves and (b) corresponding normalized load-deflection curves for specimens of the tempers T351 (CB-6, CB-7) and T8 (CB-1, CB-2).

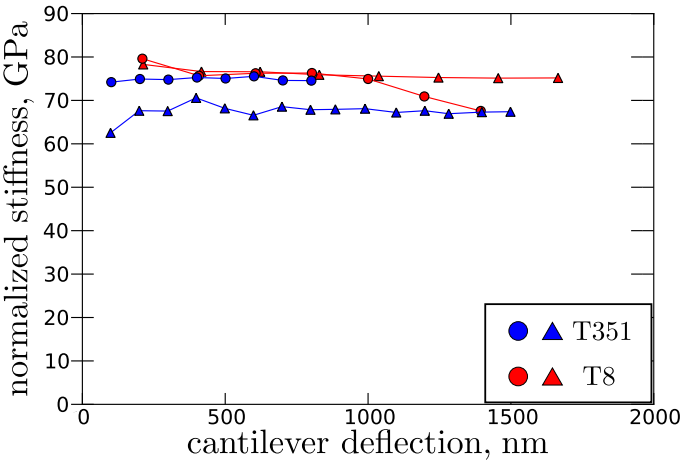

Figure 4.13 Normalized stiffness versus the deflection of the cantilever at the beginning of each corresponding unloading segment.

detailed analysis of the mechanisms involved in the failure of grain boundaries in AA2198 is limited to the effects of gallium embrittlement, several examples of the features discernible from this technique are presented in the following paragraphs.

Figure 4.14 shows high resolution SEM-micrographs of the crack tips (figure 4.14(a) and 4.14(b)) or directly behind the crack tip (figure 4.14(c)) for various tested cantilevers. Most crack tips were sharp irrespective of the thermo-mechanical condition, as shown in figure 4.14(a). In the grain on the left, slip traces are clearly visible. Such planar slip is known to cause stress concentrations at grain boundaries [65] which promote intergranular failure. Another feature which could be observed was a domain of bridging elements behind the crack tip also in an underaged specimen (see figure 4.14(b)). Lastly, a blunted crack tip in a peak-aged specimen (figure 4.14(c)) was observed. The interfacial crack in this specimen was stopped at a triple junction, and massive slip occurred at the crack tip. The largely vertical lines which are seen in figure 4.14(b) and 4.14(c) result from the specimen fabrication through FIB milling, the so-called "curtaining effect", and should not be confused with slip lines.

For further investigations into the mechanisms involved in the initiation and propagation of a crack, it is of great interest to examine the fracture surfaces after testing. The specimens remain connected to the support by a small ligament due to the plastic deformation and compressive stresses on the lower part of the cantilever. It is also possible that the cantilever makes contact with the material or the tip of the indenter makes contact with the material surrounding the cantilever. While the maintained attachment of the cantilever allows the identification of the indenter contact position which is needed to measure the bending length, the fracture surfaces are not readily accessible for imaging and need to be separated. In order to create enough space for the separation of the fracture surfaces using a Omniprobe micro-manipulator the cantilever was shortened using FIB milling. The micro-manipulator was carefully brought in contact with the shortened beam which was then deflected

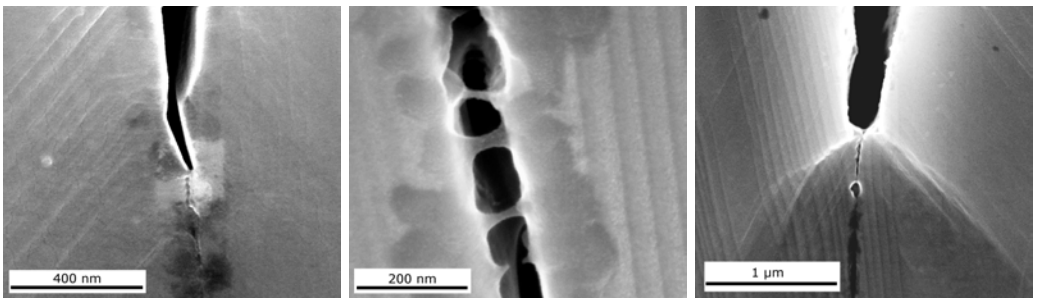

(a) **(b)** **(c)**

Figure 4.14 (a) Sharp crack tip as observed in most specimens. Slip lines can be seen on one of the adjacent grains. (b) Bridging elements found behind a crack tip of an underaged specimen. (c) Rounded crack tip in a peak-aged specimen showing massive slip on the crack ground.

to open the crack completely. It is worth noting that the complete removal of the cantilever up to the fracture is not possible since redeposition on the fracture surfaces must be avoided.

After opening the cracks further, the fracture surfaces reveal additional information regarding the mechanisms of fracture. The underaged specimens exhibit generally smooth fracture surfaces with some larger particles visible, as shown in figure 4.15(a) and figure 4.15(b). Lines resembling fatigue striations which bow around the coarse particles are found on the fracture surface (figure 4.15(a)). Figure 4.15(b) shows the fracture surface of the specimen that exhibits the domain of bridging elements shown in figure 4.14(b). The fracture surface may be divided into two regions. The first region resembles to the smooth surface of figure 4.15(a). The second region shows a highly dimpled morphology. The fracture surfaces for the peak-aged specimens show particles smaller than those found on the fracture surfaces of the underaged specimens, as can be seen from figure 4.15(c). This fracture surface corresponds to the crack tip shown in figure 4.14(c). The striation-like lines mentioned before are not found in any of the peak-aged specimens.

The features presented here give insight into the morphology of the intergranular cracks and the mechanisms involved in the fracture process. The coarse particles found on the fracture surfaces of the T351 specimens act as stress concentrators also promoting grain boundary failure. The multiple unloads used in the bending experiment can be one reason for the appearance of the striation-like lines on the fracture surfaces of the T351 specimens since the number of unloads may be roughly correlated to the number of lines. However, other T351 specimens either do not show these lines or the lines are less pronounced. The orientation of the boundary and the adjacent grains and, in particular, the particles on the grain boundaries are expected to influence the formation of these lines. From the fracture surfaces shown in figure 4.15(b) it can be seen that the fracture mode has changed from brittle fracture to dimpled fracture which indicates ductile deformation within the bound-

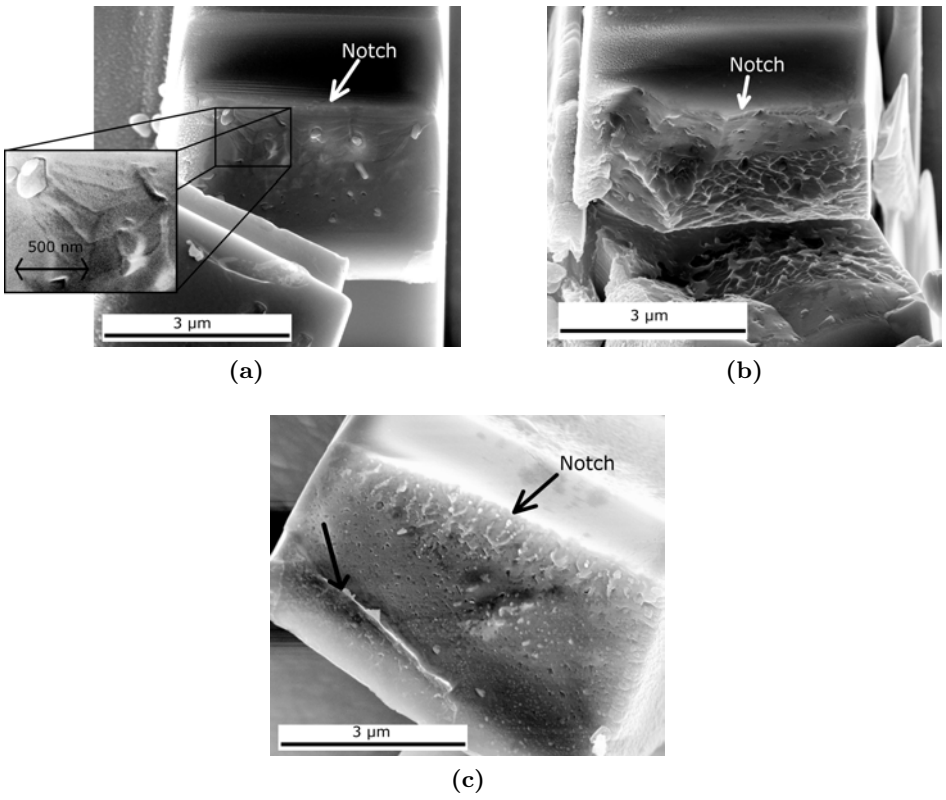

Figure 4.15 (a) Smooth fracture surface of a grain boundary in an underaged specimen showing large particles and striation like lines. (b) Partially dimpled fracture surface of an underaged specimen. (c) fracture surface of a grain boundary in a peak-aged specimen with finely distributed particles, the arrow marks the position where the crack stopped.

ary. More investigations on the morphology of the grain boundary are required to determine the cause for this change in fracture mode. However, due to the influence of gallium on grain boundaries in aluminum a detailed study of the mechanisms of grain boundary failure is beyond the scope of this thesis.

Summary

- The aluminum alloy 2198 has been chosen as a model material since it provides a combination of ductile grains with brittle interfaces which is a fundamental case for intergranular fracture in metals. The microstructure of this alloy provides flat grain boundaries and therefore the possibility of creating microscopic bending specimens with a constant crack width. The grain boundary properties of this alloy may be altered by heat treatments.

- Additional embrittlement of the grain boundaries due to the FIB preparation involving a gallium ion source is acceptable for the development of the method since the material's character of brittle interfaces and ductile grains is not changed.
- An experimental method for the separation of single grain boundaries has been established. Notched cantilever specimens with a rectangular cross-section have been chosen since they provide the most promising approach for microscopic fracture experiments.
- Corrections to the experimental data that arise due to the use of a sharp indentation tip have been established.
- The stiffness measurements have shown that the specimens fail without significant propagation of the damage. The grain boundaries can, thus, be identified as brittle interfaces.
- A finite element framework for the analysis of the specimens has been established. This framework incorporating a linear elastic material can be used to compare the load and the stiffness of similar specimens up to the yield load and to identify the onset and propagation of damage. However, for the analysis of stresses and strains at the moment of fracture, the plastic deformation of the specimens needs to be taken into account.

5 Determination of the Plastic Deformation Properties of the Grains

In order to describe the plastic deformation in the oligo-crystalline cantilevers the anisotropic deformation behavior of each grain must be taken into account. A finite element crystal plasticity material model is capable to describe the anisotropic deformation behavior. However, an independent determination of the plastic deformation properties is required. Since the determination of the model parameters is difficult to perform from load-displacement data of polycrystalline structures and macroscopic single crystals are not available for the specific temper of the alloy, micro-column compression experiments were carried out in order to provide uniaxial load-displacement data from single crystals of the alloy. The investigations into the plastic deformation behavior have been limited to the under-aged material (T351).

5.1 Experimental Set-up and Data Analysis

Micro-columns with a nominal diameter of 2 µm were prepared into the polished* surface of the sample. The transverse direction was parallel to the axis of the column, as shown in figure 4.1. Since the average grain thickness is 3 µm, the choice of columns with a diameter of 2 µm allowed for the fabrication of single crystal columns. Combining EBSD-measurements and focused ion beam imaging, preferable grains for column fabrication were identified. Coarser grains were found from FIB images of areas adjacent to the desired spot for milling. FIB marks were produced to identify these locations during the later milling process. Then, the orientation of the grains in these regions was determined by EBSD also revealing the shape of the grains such that the final milling location could be established. This location was marked by a "cross-hair" pattern in order to identify the position of the column axis using FIB images without directly scanning over the column. Annular milling [21] was used to fabricate the micro-columns, as schematically illustrated in figure 5.1. The outer diameter was chosen to leave enough space for a flat punch indenter. During the procedure concentric rings were milled into the surface while the ion current was stepwise reduced from 7 nA to 50 pA. This enabled finer control of the column geometry such that the taper angle could be reduced to less than 2°. The nominal dimensions of the columns were 2 µm : 6 µm (diameter : height), resulting in an

*see section 4.3 for polishing procedure

aspect ratio of 1 : 3. This aspect ratio provides a sufficiently homogeneous stress field in the column while preventing instable deformation modes like buckling. Due to the anisotropic milling rates for different crystallographic orientations the annular milling procedure created an uneven surface. In order to reduce elevated differences in the height of the surface, these differences were leveled after each milling step, but cannot be completely circumvented.

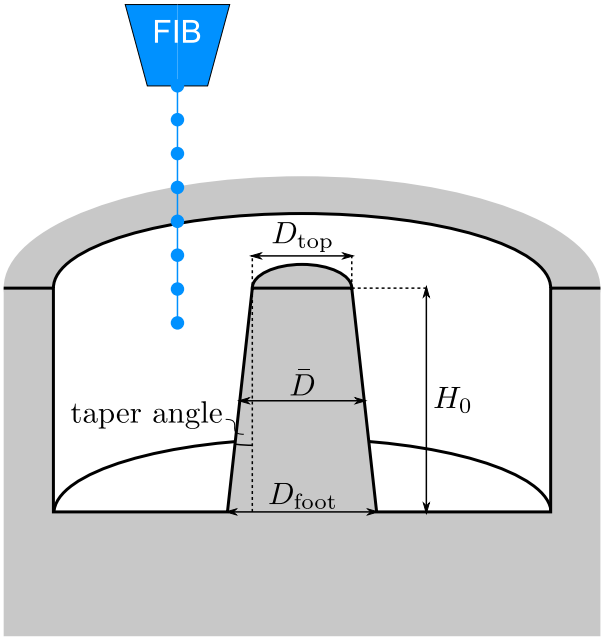

Figure 5.1 Annular milling procedure for the fabrication of micro-columns. The column geometry is determined by the initial height, H_0, and the diameter at the top, D_{top}, and at the foot, D_{foot}, of the column. The average diameter, $\bar{D}$, and the taper angle are calculated assuming that the diameter increases linearly from the top to the foot.

A set of micro-columns was fabricated according to the procedure described previously. Due to the need to create single crystalline volumes, the average diameters of the columns were in the rage between 1.5 µm to 2.0 µm and the initial height was in the range was in the range between 5.5 µm and 7.0 µm; the aspect ratio is held in the range between 1 : 2 and 1 : 4. For further investigations into the size dependence of the mechanical behavior, two columns with nominal diameters of 1 µm and 3 µm, aspect ratios of 1 : 3 (diameter : height) and similar orientations were fabricated. As shown later in this chapter, the specimen size does not influence the mechanical behavior for the considered range of specimen dimensions. The micro-columns have the shape of a tapered cylinder such that the geometry of each column is given by the initial height, H_0, and the initial diameters on the top, D_{top}, and at the foot, D_{foot}.

The micro-columns were compressed making use of the same nanoindenter as used for the bending experiments. The indenter was equipped with a flat punch tip

with a diameter of 15 µm in order to create a uniform displacement at the head of the column. The outer diameter for the milling procedure was chosen as 25 µm such that the indenter tip does not make contact with the material surrounding the column. The experiments were carried out using the displacement control with a constant nominal strain rate, $\dot{\epsilon}$, of $0.0005\,\mathrm{s}^{-1}$. This strain rate was achieved by adjusting the displacement rate, $\dot{h}$, for each column of the initial height, H_0, according to:

$$\dot{h} = \dot{\epsilon}\, H_0. \tag{5.1}$$

In addition to the load-displacement data the elastic stiffness of the column and its support was measured by making use of the dynamic indentation technique (continuous stiffness measurement, CSM). For the CSM measurement a displacement amplitude of 2 nm and a frequency of 45 Hz have been used. An example for a column before and after compression is shown in figure 5.2. The corresponding load-displacement data is shown in figure 5.3. The geometry of the tested specimens is given in table 5.1.

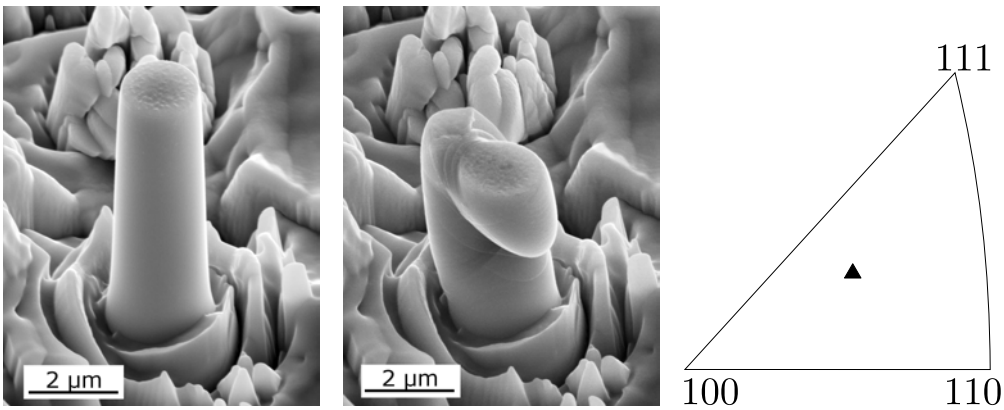

Figure 5.2 Example for a micro-column (a) before and (b) after the compression experiment. (c) Inverse pole figure describing the orientation of the compression axis in relation to the grain.

Data Analysis

The steps on the tested column in figure 5.2(b) indicate that plastic deformation took place along distinct slip planes. Moreover, the plastic deformation is restricted to the upper part of the column where the stresses are expected to be maximum due to the tapered shape of the column. The column shown in figure 5.2(b) has been deformed to strains larger than 30 %. The flattened region next to the circular initial contact area at the top of the column is formed when the indenter makes contact with the part of the column below the slip region. As expected from other microscopic

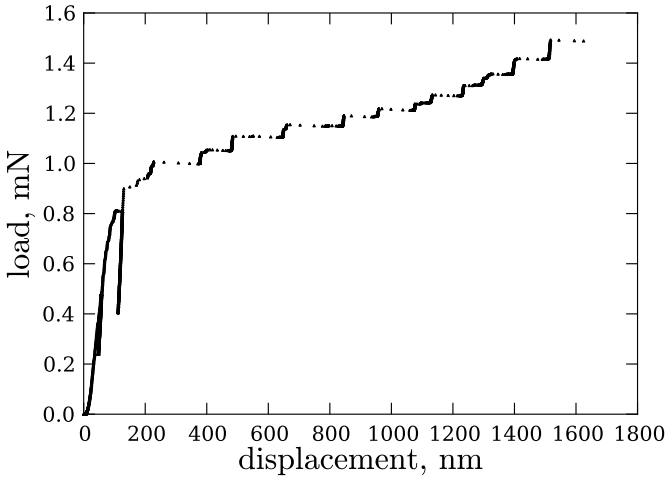

Figure 5.3 Load-displacement response of the micro-column shown in figure 5.2.

single crystal deformation experiments [16, 21] a mostly linear increase of the load is followed by discontinuous plastic deformation with displacement bursts.

The discontinuous plastic deformation is attributed to dislocation movement on distinct slip systems. Since the aluminum alloy has a FCC crystal structure the single crystals are expected to deform on $\{1\,1\,1\}$ crystallographic planes and in $[1\,1\,0]$ crystallographic directions. Including all permutations, 12 independent slip systems are available for the deformation. In order to determine the number of slip systems that are active during a compression experiment the Schmid factors are calculated. The Schmid factor, m, relates the normal stress ς to the resolved shear stress τ, i. e. the shear stress acting on a slip system:

$$\tau = m \cdot \varsigma. \tag{5.2}$$

Knowing the Schmid factors for a single crystal is particularly useful since they allow to distinguish between experiments where initially only one slip system is active and experiments where slip is initiated on multiple slip systems. For the measured orientation of the column along the column axis, as given by the inverse pole figure in figure 5.2(c), a maximum Schmid factor of 0.48 is achieved. The next lower Schmid factor is 0.40, suggesting that only one slip system is active during the beginning of the plastic deformation. However, at later stages of the plastic deformation more slip systems are activated due to changes in the geometry and the continuously changing crystallographic orientation [66].

Due to imperfections in the contact between indenter and column stemming from surface roughness due to redeposition during the milling process the point of full contact is not consistent with the point of initial contact. In order to assess the column deformation the following procedure is applied. First, as shown in figure 5.4(a) the local slope of the loading curve, which will be called loading stiffness,

Specimen	D_{top}, µm	D_{foot}, µm	H_0, µm
CC-1	1.76	2.46	6.52
CC-2	1.70	2.30	7.98
CC-3	1.70	2.23	5.46
CC-4	1.61	2.19	6.28
CC-5	1.59	2.21	6.63
CC-6	1.67	2.08	5.65
CC-7	1.63	2.18	6.10
CC-8	1.8	2.16	6.26
CC-9	1.82	2.21	6.77
CC-10	1.76	2.13	6.4
CC-11	1.91	2.15	6.55
CC-12	1.92	2.13	6.87
CC-13	1.91	2.27	6.32
CC-14	1.44	1.62	6.57
CC-15	0.96	1.21	3.45
CC-16	2.73	3.35	8.90
CC-17	0.81	1.04	3.64

Table 5.1 Geometries for the tested micro-columns. The aspect ratio is calculated using the average diameter.

is determined by using a linear fit over a range of $\pm$ 3 nm[†] around each point of the loading curve. The maximum of the slope, S_{fc}, is associated with the point of full contact, where effects of the surface roughness on the top of the column are negligible. As illustrated in figure 5.4(a), the yield point, $(h_{\text{Y}}, P_{\text{Y}})$, is defined here as the point where the slope of the loading curve becomes less than a threshold value of 20 % of S_{fc}.

The elastic analysis of the mechanical behavior of the columns is circumvented by the uneven foot of the column due to the anisotropic milling rates of the individual grains adjacent to the column. However, since the column diameter at the foot is larger than at the top, the highest stresses are expected at the top of the column. Therefore, the plastic deformation is restricted only to the upper part of the column, while the foot of the column is assumed to be subject to purely elastic deformation [28]. Since only the displacement associated with the plastic deformation is of interest for the determination of the parameters of the crystal plasticity model, an explicit analysis of the elastic material behavior is not needed. In order to obtain the displacement associated with the purely plastic deformation, h_{pl}, the

[†] $\pm$20 measuring points since the data acquisition rate is 10 Hz

experimental data must be corrected for the displacement associated with the elastic deformation, $h_{\mathrm{el}}^{\mathrm{cor}}$, as illustrated in figure 5.4(b):

$$h_{\mathrm{el}}^{\mathrm{cor}}(P) = \frac{P}{S_{\mathrm{fc}}}. \tag{5.3}$$

Assuming that the plastic deformation starts at the yield point, $(h_{\mathrm{Y}}, P_{\mathrm{Y}})$, deviations from the linear loading before the yield point require an additional correction, $h_{\mathrm{const}}^{\mathrm{cor}}$. This correction is found by extrapolating linear loading behavior to zero load, starting at the yield point:

$$P = 0 = S_{\mathrm{fc}}(h_{\mathrm{const}}^{\mathrm{cor}} - h_{\mathrm{Y}}) + P_{\mathrm{Y}}, \tag{5.4}$$

therefore:

$$h_{\mathrm{const}}^{\mathrm{cor}} = h_{\mathrm{Y}} - \frac{P_{\mathrm{Y}}}{S_{\mathrm{fc}}}. \tag{5.5}$$

The displacement associated with plastic deformation, $h_{\mathrm{pl}}(P)$, is then calculated as:

$$h_{\mathrm{pl}}(P) = h(P) - h_{\mathrm{el}}^{\mathrm{cor}}(P) - h_{\mathrm{const}}^{\mathrm{cor}} \tag{5.6}$$

$$\Rightarrow \quad h_{\mathrm{pl}}(P) = h(P) - \frac{P}{S_{\mathrm{fc}}} - \left(h_{\mathrm{Y}} - \frac{P_{\mathrm{Y}}}{S_{\mathrm{fc}}}\right). \tag{5.7}$$

where h is the total displacement of the indenter.

In order to compare specimens with differing geometries the engineering stress, σ, and the engineering plastic strain, ε, are defined as:

$$\sigma = \frac{P}{\bar{A}} = \frac{P}{\frac{\pi}{4}\bar{D}^2} \tag{5.8}$$

and

$$\varepsilon = \frac{h_{\mathrm{pl}}}{H_0}, \tag{5.9}$$

where $\bar{A}$ is the area at the center of the column and $\bar{D}$ is the average diameter, which is calculated using the diameter of the column at the top, D_{top}, and at its foot, D_{foot}:

$$\bar{D} = \frac{D_{\mathrm{top}} + D_{\mathrm{foot}}}{2}. \tag{5.10}$$

This normalization can be applied to the experimental data as well as to the simulations.

5.2 Crystal Plasticity Model for Finite Element Simulations

Both the elastic and the plastic deformation of the grains are anisotropic due to the crystal structure. Using finite element simulations this deformation is reproduced

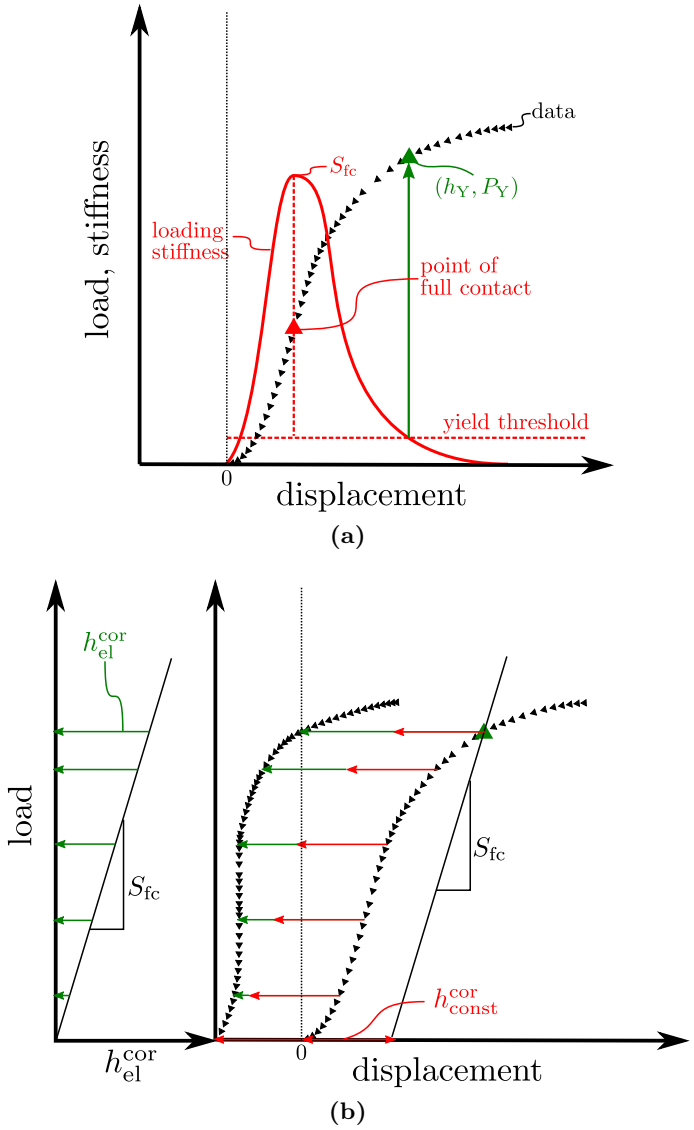

Figure 5.4 (a) Definition of the yield point based on the loading stiffness of a micro-column. (b) Correction to the experimental compression data of a micro-column to obtain the displacement associated with plastic deformation starting at the yield point.

with a crystal plasticity constitutive model. In the following the constitutive equations for the model used within this work are given. The origin of this model is a crystal plasticity user material subroutine (UMAT) developed at Harvard University [67], which bases on the framework of Peirce *et al* [68] and Asaro [69, 70]. The UMAT used in this work has been modified by Graff [71].

The deformation gradient, $\mathbf{F}$, of a crystal lattice can be multiplicatively decomposed into a part referring to the stretching and the rotation of the lattice, $\mathbf{F}^*$, and the deformation gradient associated with the plastic deformation, $\mathbf{F}^\mathrm{p}$:

$$\mathbf{F} = \mathbf{F}^* \mathbf{F}^\mathrm{p} \tag{5.11}$$

The velocity gradient therefore can be decomposed in a part referring to the stretching and the rotation of the lattice, $\mathbf{L}^*$, and a plastic part, $\mathbf{L}^\mathrm{p}$:

$$\begin{aligned} \mathbf{L} &= \dot{\mathbf{F}}\mathbf{F}^{-1} \\ &= \mathbf{L}^* + \mathbf{L}^\mathrm{p} \\ &= (\mathbf{D}^* + \boldsymbol{\Omega}^*) + (\mathbf{D}^\mathrm{p} + \boldsymbol{\Omega}^\mathrm{p}) \end{aligned} \tag{5.12}$$

where $(\mathbf{D}^*, \boldsymbol{\Omega}^*)$ are the lattice parts of the rate of the stretching tensor and the spin tensor, respectively. Accordingly, $(\mathbf{D}^\mathrm{p}, \boldsymbol{\Omega}^\mathrm{p})$ are the plastic parts of the rate of the stretching tensor and the rate of the spin tensor. Taking into account that the plastic deformation is constrained to specific slip directions, $\mathbf{m}^\alpha$, on particular lattice planes described by their normals $\mathbf{n}^\alpha$, the plastic velocity gradient, $\mathbf{L}^\mathrm{p}$, for the deformation is expressed by the sum of the slip rates on all slip systems:

$$\mathbf{L}^\mathrm{p} = \sum_\alpha \dot{\gamma}^\alpha \, \mathbf{m}^\alpha \cdot \mathbf{n}^\alpha, \tag{5.13}$$

where $\dot{\gamma}^\alpha$ describes the slip rate on the slip system α. $\mathbf{n}^\alpha$ and $\mathbf{m}^\alpha$ are given in the current configuration.

The constitutive law for elastic deformation in a rotating coordinate system can be written as:

$$\overset{\triangledown^*}{\boldsymbol{\sigma}} + \boldsymbol{\sigma}(\mathbf{I} : \mathbf{D}^*) = \mathbf{C} : \mathbf{D}^* \tag{5.14}$$

with $\mathbf{C}$ being the tensor of elastic constants, $\boldsymbol{\sigma}$ the Cauchy stress, and $\overset{\triangledown^*}{\boldsymbol{\sigma}}$ the Jaumann rate of the Cauchy stress formed on the axes that spin with the crystal lattice. This rate is related to the corotational stress rate on axes rotating with the material, $\overset{\triangledown}{\boldsymbol{\sigma}}$, by:

$$\begin{aligned} \overset{\triangledown^*}{\boldsymbol{\sigma}} &= \overset{\triangledown}{\boldsymbol{\sigma}} + (\boldsymbol{\Omega} - \boldsymbol{\Omega}^*) \cdot \boldsymbol{\sigma} - \boldsymbol{\sigma} \cdot (\boldsymbol{\Omega} - \boldsymbol{\Omega}^*) \\ \text{with} \quad \overset{\triangledown}{\boldsymbol{\sigma}} &= \dot{\boldsymbol{\sigma}} - \boldsymbol{\Omega} \cdot \boldsymbol{\sigma} + \boldsymbol{\sigma} \cdot \boldsymbol{\Omega} \end{aligned} \tag{5.15}$$

The plastic deformation on distinct slip systems is assumed as a viscoplastic power law. The slip rate on each slip system α depends on the resolved shear stress τ^α:

$$\frac{\dot{\gamma}^\alpha}{\dot{\gamma}_0^\alpha} = \left| \frac{\tau^\alpha}{\tau_\mathrm{Y}^\alpha} \right|^n \cdot \operatorname{sign}\left(\frac{\tau^\alpha}{\tau_\mathrm{Y}^\alpha} \right). \tag{5.16}$$

Here $\tau_{\mathrm{Y}}^{\alpha}$ characterizes the resistance to slip on the slip system α, i. e. the critical resolved shear stress (CRSS). $\dot{\gamma}_0^{\alpha}$ is a reference shear rate and n is the rate sensitivity exponent. The choice of the visco-plastic model for the slip systems allows for a numerically stable way of distinguishing between active and inactive slip systems.

The evolution of the resistance to slip during the deformation process is described by:

$$\dot{\tau}_{\mathrm{Y}}^{\alpha} = \sum_{\beta} h_{\alpha\beta}(\bar{\gamma})\, \dot{\gamma}^{\beta}, \tag{5.17}$$

with the hardening moduli $h_{\alpha\beta}$, that describe the self hardening ($\alpha = \beta$) on a slip system and the latent hardening ($\alpha \neq \beta$) due to plastic deformation on other slip systems. $\bar{\gamma}$ is the cumulative shear strain on all slip systems and can be calculated from:

$$\bar{\gamma} = \sum_{\alpha} \int_0^t |\dot{\gamma}^{\alpha}| \, \mathrm{d}t^*. \tag{5.18}$$

The interaction between slip systems is described by using the interaction coefficients, $q_{\alpha\beta}$, and a hardening law, $h(\bar{\gamma})$:

$$h_{\alpha\beta}(\bar{\gamma}) = q_{\alpha\beta}\, h(\bar{\gamma}) \tag{5.19}$$

The hardening law in this model is described by an exponential saturation law:

$$h(\bar{\gamma}) = h_0 \left(1 - \frac{\tau_0}{\tau_\infty}\right) \exp\left(-\frac{h_0\, \bar{\gamma}}{\tau_\infty}\right), \tag{5.20}$$

with the initial hardening modulus, h_0, and the saturation hardening shear stress, τ_∞.

The resistance to slip at each instant t is then given by:

$$\tau_{\mathrm{Y}}^{\alpha} = \tau_0 + \int_0^t h(\bar{\gamma}) \left(\sum_{\beta} q_{\alpha\beta} \dot{\gamma}^{\beta}\right) \mathrm{d}t^*. \tag{5.21}$$

The integration constant, τ_0, is a measure for the initial resistance against slip for each slip system, i. e. the initial critical resolved shear stress.

Model Set-up and Handling of the Orientation

The material model has been implemented in a UMAT in the framework of the finite element software ABAQUS. The grains of the model material show a face centered cubic (FCC) crystallographic structure. The elastic constants for AA2198 have been estimated as given by equation 4.19.

For FCC metals the plastic deformation is constrained to slip on $\{1\,1\,1\}$ planes in $[1\,1\,0]$ directions. In order to correctly determine the resolved shear stress on each slip system, the relation between the crystal orientation and the global orientation must be established. EBSD measurements provide the orientation in terms of Euler

angles. An orthogonal rotation tensor, $\mathbf{R}$ can be calculated from these angles. This rotation tensor, $\mathbf{R}$, defines the rotation of the crystal coordinate system into the global coordinate system, i. e. the components of the crystallographic vector, $\mathbf{v}_{\text{crystal}}$, are expressed in global coordinates by:

$$\mathbf{v}_{\text{global}} = \mathbf{R}\,\mathbf{v}_{\text{crystal}}. \tag{5.22}$$

With this relation given, material orientations for the crystals in ABAQUS are determined from three points: the origin $(0, 0, 0)$ and the components of the crystallographic vectors $(1, 0, 0)$ and $(0, 1, 0)$ in the global coordinate system. The parameters for the constitutive model need to be defined only once in the ABAQUS input file and the material orientations are defined for each grain in the definition of a material section.

The material is assumed to be rate independent. Therefore, the visco-plasticity exponent, n, in equation (5.16) should have a large value. For reasons of numerical stability of the simulations a maximum value of 20 is used in this work. The reference strain rate has been fixed to $0.001\,\text{s}^{-1}$. These parameters for the visco-plasticity have been used throughout the present work.

Finally, the hardening parameters need to be determined such that the load-displacement data of columns is correctly reproduced by the FE calculations. In order to reduce the number of fitting parameters, three cases can be distinguished: self hardening for one slip system, interaction of active slip systems on one slip plane (coplanar slip) and interaction of slip systems acting on different slip planes (non-coplanar slip). Thus, the interaction coefficients can be reduced to:

$$q_{\alpha\beta} = \begin{cases} 1 & \text{if } \alpha = \beta \\ q_{\text{cp}} & \text{for coplanar slip} \\ q_{\text{ncp}} & \text{for non-coplanar slip.} \end{cases} \tag{5.23}$$

5.3 Experimental Determination of the Crystal Plasticity Parameters

Displacement bursts during the plastic deformation have been found in compression experiments on micro-columns of various metals (e. g. [16, 21, 72]). This discontinuous plastic deformation is attributed to the discrete nature of dislocation activity. The crystal plasticity model used here describes the anisotropic deformation within strain levels where differences in the geometry between the experiment and the simulation are small, even though the model cannot account for discontinuous deformation. From the shape of the load-displacement curves of several specimens the plastic deformation shows a tendency to saturate. The exponential saturation hardening law, as presented in section 5.2, provides a good representation for this saturation within the FE model. The remaining parameters to be determined are the self hardening parameters and the interaction coefficients. The self-hardening parameters are the initial flow stress, τ_0, the initial hardening modulus, h_0, and the

saturation hardening stress, τ_∞. The interaction coefficients are given as q_{cp} and q_{ncp} for coplanar and non-coplanar slip, respectively.

Finite element models for each micro-column were created. These models for the micro-columns are three dimensional models that include the initial height as well as the diameters at the foot and on top of the column. An example FE-mesh is shown in figure 5.5. The column is smoothly connected to its support which consists of a cylindrical disk of 10 µm in height. The orientation of the respective column was assigned to the complete model; orientations of adjacent grains have been neglected. The ABAQUS mesh generator was used to create the finite element mesh that consists of 8-node brick elements (C3D8). The approximate length of each element edge was requested to be smaller than a tenth of the columns diameter on the top. The mesh in the support coarsens with increasing distance to the column. The bottom surface of the support was subject to fixed boundary conditions. The indenter was modeled by a prescribed axial displacement on the top surface of the column not allowing for lateral movement of any node of the top surface. Thus, the experiment was modeled assuming ideal adhesion of the indenter to the top surface of the column and no lateral compliance of the indenter. The displacement rate was set to the average displacement rate during the experiment which is determined by the maximum displacement at 10 % engineering strain, divided by the time needed to achieve this displacement. The investigation of the deformation is limited to the displacement where 10 % of the engineering strain is achieved. Beyond that point the geometry of the deformed column significantly differs from the geometry found in the simulation due to the discrete deformation. The parameters of the crystal plasticity model are, thus, fitted to this limit of 10 % engineering strain.

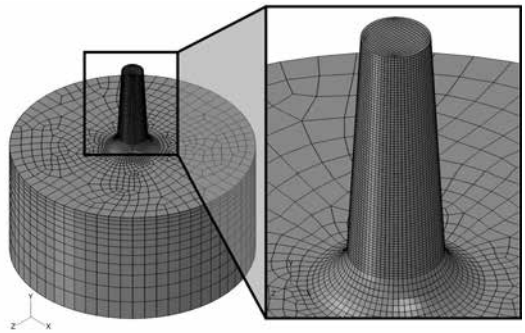

Figure 5.5 Example FE-mesh for modeling of the deformation of a micro-column.

For the determination of the crystal plasticity constants a column with deformation on one distinct slip system was selected. This allows to determine the self hardening parameters, τ_0, τ_∞ and h_0, of one slip system without influence of other slip systems. The load-displacement data determined from the simulation was compared to the deformation of the corresponding specimen which was determined from the analysis procedure given in section 5.1. A set of simulations was carried out to determine optimized parameters that allow for the correct reproduction of the load-displacement curve (see figure 5.6). Within these simulations both interaction

τ_0, MPa	τ_∞, MPa	h_0, MPa	q_{cp},-	q_{ncp},-
120.0	137.0	8000.0	2.0	10.0

Table 5.2 Crystal plasticity constants determined form micro-compression experiments.

coefficients, q_{cp} and q_{ncp}, were set to unity. The optimized parameters are given in table 5.2. Figure 5.7 qualitatively compares the deformation from the experiment and corresponding FE-simulation. The global slip direction of the column in the FE simulation is identical to the slip deformation in the corresponding experiment. Moreover, only the slip system with the highest Schmid factor is active in the simulation of the specimen oriented for single slip, which is shown in figure 5.8. The plastic deformation in the simulation is restricted to the upper part of the column confirming the assumption that the influence of the foot on the plastic deformation is negligible. The secondary slip system remains inactive until later stages of deformation.

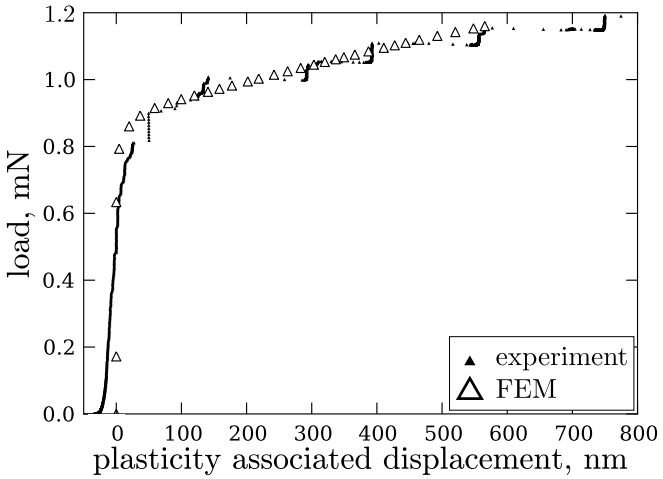

Figure 5.6 Load-displacement response of the specimen oriented for single slip (CC-1). Open symbols represent the simulation results, solid symbols give the experimental data.

After the self hardening parameters were determined, the interaction parameters were adjusted to reproduce the deformation of columns with more than one initially active slip system. The experimental load-displacement data of a column with two active coplanar slip systems was used to quantify the interaction coefficient q_{cp}. Another column with two non-coplanar slip systems provided the experimental data to determine the interaction coefficient q_{ncp}. The interaction coefficients are also given in table 5.2. These coefficients differ form the coefficients usually used in crystal plasticity simulations which are 1 for coplanar slip and 1.4 for non-coplanar slip (see [73]). Figure 5.9 depicts the experimental load-displacement data of the

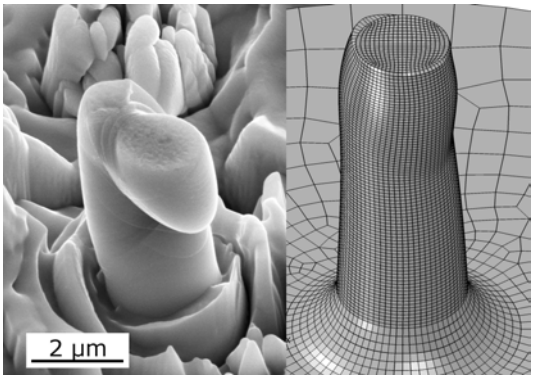

Figure 5.7 Comparison of the deformations of a tested specimen (CC-1) and the corresponding simulation. The simulation depicts the result corresponding to 10 % nominal strain while the maximum nominal strain in the experiment was 30 %. The slip direction in the experiment is identical to the slip direction in the simulation.

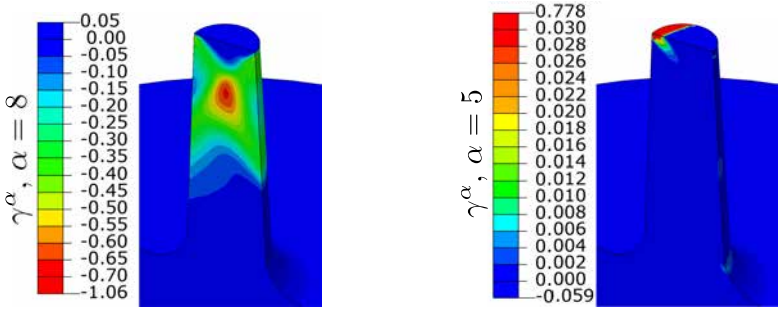

(a) **(b)**

Figure 5.8 Simulation of a deformed column (CC-1) shown in figure 5.2. The color code represents the shear strain, γ, (a) on the slip system with the highest Schmid factor, 0.48, and (b) the slip system providing the second highest Schmid factor, 0.40.

columns used for the parameter optimization together with the load-displacement data extracted from the respective simulations.

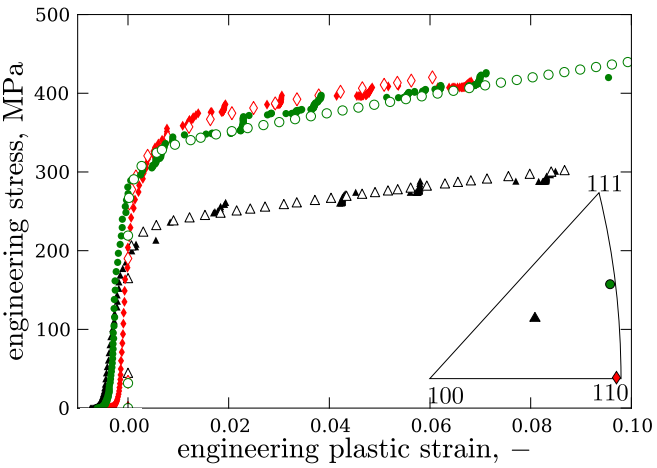

Figure 5.9 Load-displacement response (solid symbols) and FE-prediction (open symbols) for the columns used for the fitting of the crystal plasticity parameters (CC-1, CC-14 and CC-15).

The material model was verified by applying the parameter set to the FE simulations of the remaining columns. The results for three columns are shown in figure 5.10. The material model predicts the load-displacement response of columns with various orientations quite well.

In order to provide limits for the application of the crystal plasticity parameters the average value of the accumulated plastic strain, $\bar{\gamma}$, at an engineering plastic strain of 10 % in a column without the support was calculated. For the column oriented for single slip as given in figure 5.8 this value is on the order of 20 %. If during the application of the adjusted crystal plasticity model values beyond this limit are found at material points, the respective material behavior must be considered as an extrapolation of the model.

In the case of columns with the compression axis close to a [1 1 1] crystal orientation the material model overestimates the experimental yield stresses, as can be seen from figure 5.11. The reasons for this overestimation are probably related to the microscopic deformation mechanisms that govern the deformation of the micro-column. This deviation might be explained with the potentially unstable deformation due to compression in connection with the particular symmetry of this orientation but was not further investigated. However, it is shown in the following chapter that the overestimation has no influence on the simulation of the deformation of cantilevers.

Size Effects in Micro-Compression Tests

In the case of micro-column compression experiments on single-crystalline monolithic specimens, it is widely observed that the yield stresses increase when the

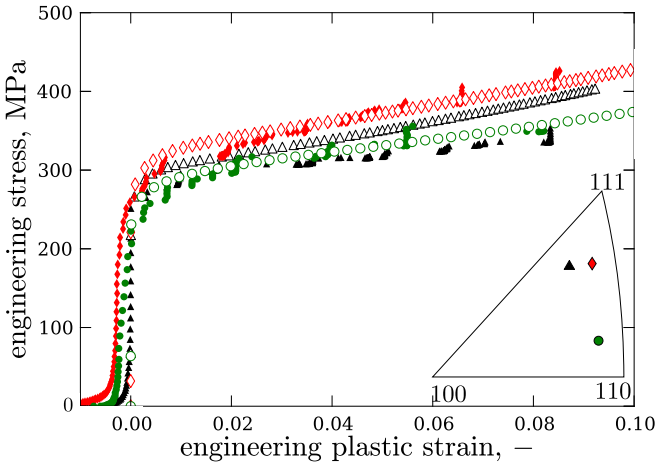

Figure 5.10 Examples for the application of the calibrated crystal plasticity model to columns with various orientations (CC-3, CC-7 and CC-17). Solid symbols are experimental data, open symbols represent simulation data.

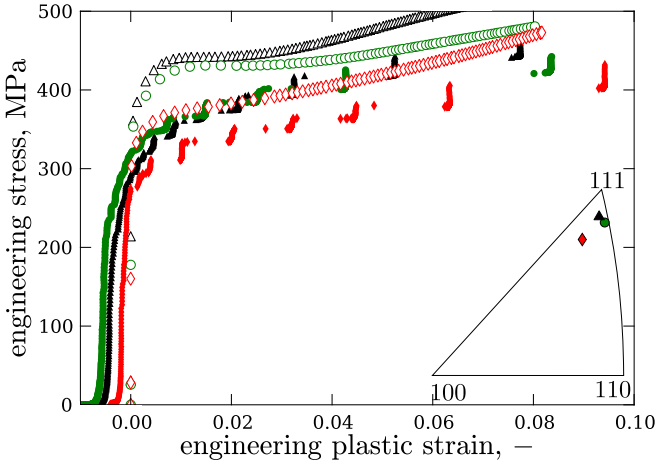

Figure 5.11 Load-displacement response of specimens with the compression axis close to a ⟨1 1 1⟩ crystal orientation (solid symbols; CC-9, CC-12 and CC-13). Open symbols represent the simulation results.

diameter of the micro-columns is decreased [16, 21], thus, for the present study an estimation of the influence of the size of the specimens on the deformation behavior is necessary.

Columns with nominal diameters of 1 µm, 2 µm and 3 µm and constant aspect ratios of 1 : 3 (diameter : height) were fabricated out of grains of similar orientations and tested with the same method as the columns presented in this chapter. Finite element simulations for each of the columns using the fitted parameter set were carried out and the results were compared to the experimental load-displacement data of the compression experiments. The load-displacement data is in good agreement with the experimental data from the compression experiments of all column sizes, as can be seen from figure 5.12. It can be concluded that crystal plasticity parameters, as determined from the micro-compression experiments on single crystalline columns of the model material, are not influenced by the size of the specimens in the investigated range between 1 µm and 3 µm. The absence of a size effect is not unexpected. Due to the alloying content and the thermo-mechanical treatment the microstructural lengthscale controlling the stress-strain behavior is much smaller than the geometric length scale as given by the diameter of the column. This is in contrast to well annealed single crystals of pure metals in which most size effects are observed.

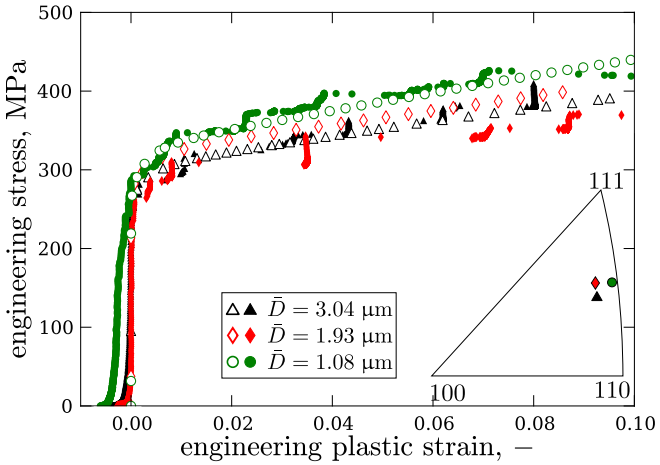

Figure 5.12 Load-displacement response of specimens with nominal diameters of 1 µm, 2 µm and 3 µm providing similar orientations along the column axis (CC-11, CC-15 and CC-16). The aspect ratio is 1 : 3 for each column. Solid symbols represent the experimental data, open symbols provide data extracted from FE-simulations.

Effects of the Boundary Conditions on the Simulation of Micro-compression Experiments

The boundary conditions can have a significant impact on the load-displacement data of micro-compression tests. For the simulations it was assumed that the surface at the foot of the column is smooth and the orientation of the surrounding material was neglected. Due to the tapered geometry of the column these regions were subject to elastic deformation only. Since the analysis of the micro-compression data excludes the elastic deformation, the assumed simplifications have no effect on the result.

The boundary conditions on top of the column can be important for the plastic deformation behavior. It is to be distinguished between effects induced by the lateral stiffness of the indenter and the friction between the indenter head and the top of the column. The lateral indenter stiffness is on the order of 10000 N/m while the lateral bending stiffness of the columns is on the order of 1000 N/m. Therefore, an indenter with infinite lateral stiffness was assumed. The friction between the indenter head and the column has not been quantified for the micro-compression tests presented here. SEM-images of tested columns show that the top surface of the columns did not alternate its shape plastically such that ideal adhesion between the indenter tip and the surrounding material is a reasonable approximation.

Summary

- Micro-column compression experiments were used to determine the load-displacement response of single crystals subjected to uniaxial stresses.
- A finite element crystal plasticity model was adopted to describe the deformation of single grains within a finite element framework.
- A set of crystal plasticity parameters was identified from the compression tests. These parameters are valid up to values of 20 % accumulated plastic strain.
- The material model was verified for various orientations with the exception of the case where orientation of the compression axis of the column is aligned with a [1 1 1] crystal orientation. The quality of the prediction for various orientations is summarized in figure 5.13.
- Influences on the measurement of crystal plasticity constants were discussed. In particular, the results were independent of the size of the columns.

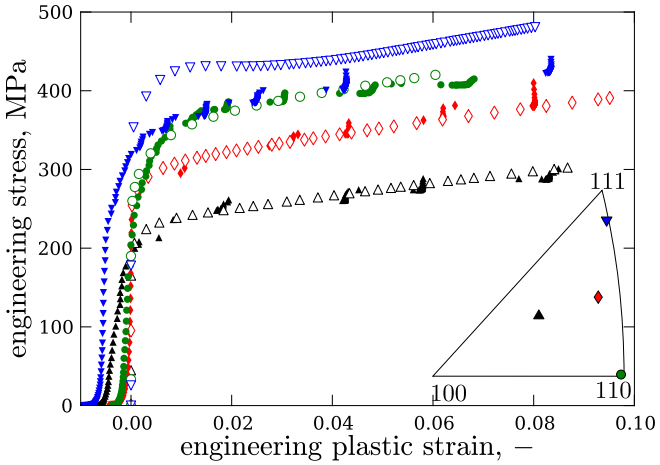

Figure 5.13 Anisotropic yield according to various crystal orientations (solid symbols). Open symbols represent the simulation results.

6 Determination of the Grain Boundary Strength

The determination of the strength of a single grain boundary requires the combination of the experimental technique as established in chapter 4 and the finite element based crystal plasticity model for the single grains presented in chapter 5. The integration of the crystal plasticity model into the finite element simulations for the notched cantilever specimens is presented here. Additionally, a cohesive zone model is introduced to the finite element framework to investigate the separation properties of a single grain boundary. Finally, the methodology is applied to two cantilevers that fractured after significant plastic deformation and shortly after the onset of plastic deformation, respectively. The results are discussed in terms of grain boundary strength.

6.1 Transfer of the Crystal Plasticity Model to the Cantilever Specimens

Finite element models for each cantilever were built according to the models presented in section 4.6 including the lateral position and the lateral stiffness of the indenter. The isotropic elastic material was replaced by the crystal plasticity model including the parameters determined in chapter 5. The cantilever was therefore partitioned into four sections as shown in figure 6.1(a). The two sections adjacent to the grain boundary were assigned the material orientations determined by EBSD measurements. In order to simplify the simulations, a specific material orientation was assigned to the sections not adjacent to the notch such that a [1 1 0] crystallographic axis was aligned with the cantilever axis. This is reasonable since simulations have shown that the crystallographic orientation of these sections has little effect on the load-displacement data and that this orientation is frequently found along the cantilever axis. The displacement at the grain boundary is prescribed to be continuous without further restrictions to the deformation. The cantilevers were loaded in displacement control using the average displacement rate identified from the experiments. In addition to the cantilevers with a grain boundary at the position of the notch, cantilevers with a notch in a single grain were fabricated. The corresponding orientations of the cantilever sections are given in figure 6.1(b).

Assessment of the Load-Displacement Response of the Cantilevers

The cantilevers with the notch placed in a single grain allow the assessment of the deformation of a grain during the bending experiment separately from any influence

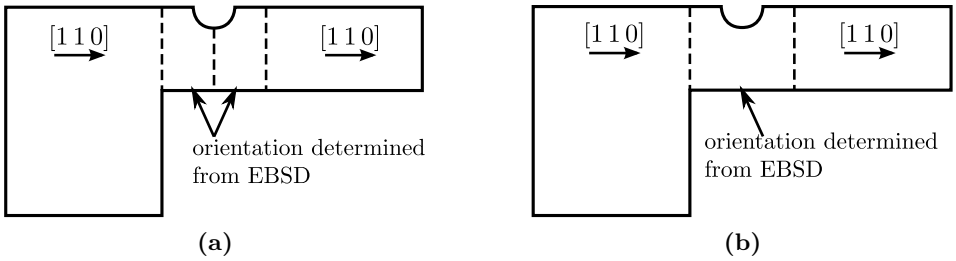

Figure 6.1 Orientations within the cantilever model (a) with the notch at the position of a grain boundary and (b) with the notch placed within a single grain.

of a grain boundary under the notch. In figure 6.2 the experimentally recorded load-deflection data for these cantilevers is compared to the corresponding data extracted from the respective simulations. Figure 6.3 shows the data for cantilevers with a grain boundary under the notch. Generally, the simulation data was in good agreement with the experimental data. However, differences between the experiments and the simulations exist. Possible reasons are discussed at the end of this section.

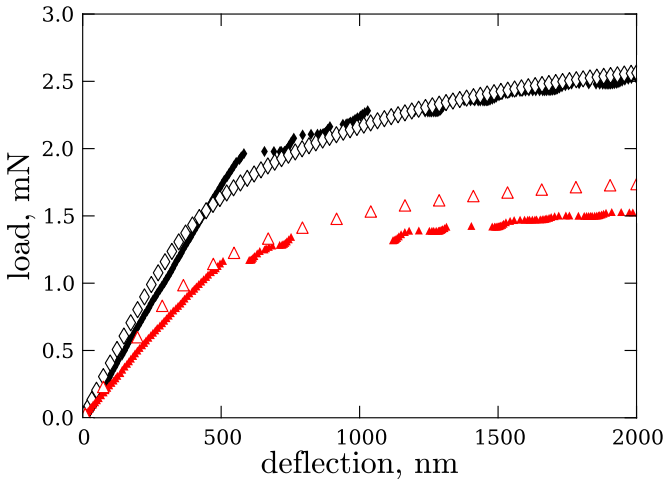

Figure 6.2 Comparison of the experimental load-deflection response of two cantilevers with the notch placed in a single grain (solid symbols) with the corresponding simulation data (open symbols).

Local Deformation in the Vicinity of the Notch

The simulations must capture the local deformations of the grains adjacent to the notch. In order to assess these deformations local measurements of the deformation field are required.

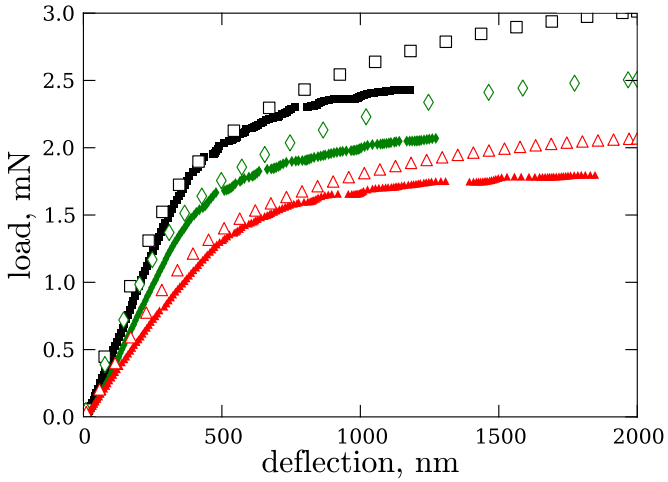

Figure 6.3 Comparison of the experimental load-deflection response of three cantilevers with a grain boundary under the notch (solid symbols) with the corresponding simulation data (open symbols).

Making use of an *in situ* test setup in the SEM, the displacement field around the notch was captured using digital image correlation, as described in section 3.4. In order to enable such measurements a platinum speckle pattern was created on the side surface of a cantilever in the region under the notch. The deposition of the platinum was achieved with the electron beam in combination with a gas injection system (GIS) to prevent any additional ion damage. The platinum pattern consisted of a large number of platinum dots such that the mechanical behavior of the cantilever was not affected by the pattern. The size of the dots was chosen according to the expected displacements, the desired magnification and the image resolution (pixel size) available. In order to capture the displacement field in the region measuring 8 µm along the cantilever axis and 6 µm along the cantilever height under the notch, platinum dots with average diameter of 200 nm were deposited. The spacing between the platinum dots was on the same order as the diameter

A reference image of the undeformed cantilever was recorded. The cantilever was then bent to a load of 1.6 mN making use of an *in situ* nanoindenter (Nanomechanics Inc.) equipped with a cube corner tip. The force on the cantilever was held constant while high resolution images of the deformed cantilever were recorded. The displacement field at the notch was determined by applying DIC to the reference image and the deformed image. The size of the subsets of pixels was on the order of the size of the platinum dots. Figure 6.4 shows the displacement field for the cantilever with a grain boundary under the notch. The experimentally determined displacement field and the displacement field extracted from the corresponding simulation at the same load were generally in good agreement. It can be concluded that not only the load-displacement curves but also the local deformations are captured by the simulations. The scatter resulting from the DIC measurement was on the order of ±5 nm while the maximum displacement was on the order of 50 nm. Hence,

the determination of the local strain field from the DIC data leads to a significant error. Inaccuracies in the displacement field under the notch may result from the scatter in the displacement measurement. Possible inaccuracies related to the finite element modeling are discussed at the end of this chapter.

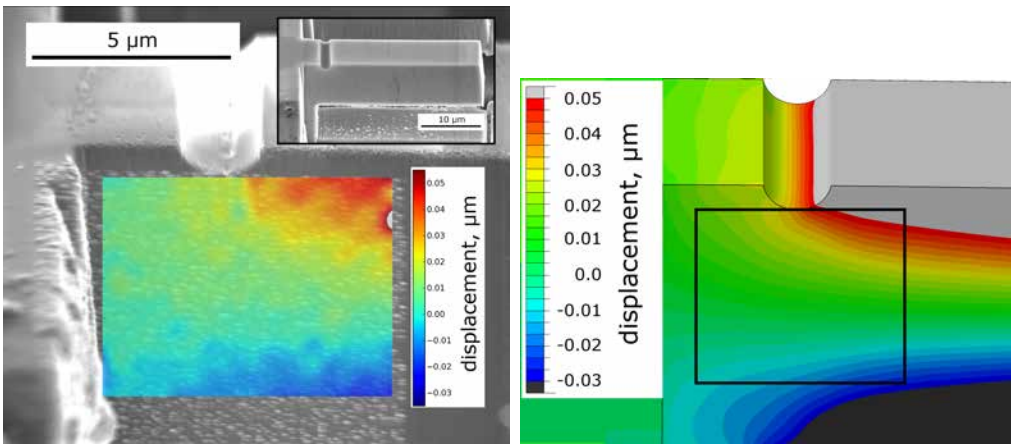

(a) **(b)**

Figure 6.4 Displacement field at the notch ground of a cantilever measured by digital image correlation (a) and extracted from the corresponding FEM simulation at the same load (b).

Deviations between Simulations and Experimental Data

The load-displacement data determined by the simulation is highly sensitive to the measured values of the characteristic dimensions. Figure 6.5(a) illustrates the effect of the geometry of the cantilever on the load-displacement data. The green triangles represent the load-displacement data extracted from a simulation of a cantilever with the nominal dimensions height : width : length = 8.0 µm : 5.0 µm : 20.0 µm. The black and red lines are the upper and lower limits calculated by varying the cantilever dimensions, respectively. The precision of the measurement of the cantilever dimensions from SEM images was better than 0.2 µm. Hence, the upper limit was achieved by adding 0.2 µm to the height and the width and by reducing the length by 0.2 µm. Accordingly, the lower limit was calculated with the width and the height reduced by 0.2 µm while the length was increased by 0.2 µm. These limits represent the worst case for deviations in the load-displacement data caused by the measurement of the geometry of the cantilevers.

While the global load-displacement response provides an overview of the deformation process the, local stress field at the grain boundary determines the fracture process. The evolution of the normal stress in the direction of the cantilever axis at the center of the notch ground was evaluated for the upper and the lower limiting cases in order to provide an estimation of the effect of the geometry on the local

stresses. In figure 6.5(b) this stress is given for the limiting curves. The differences in the geometry only slightly alter the stress at the notch ground.

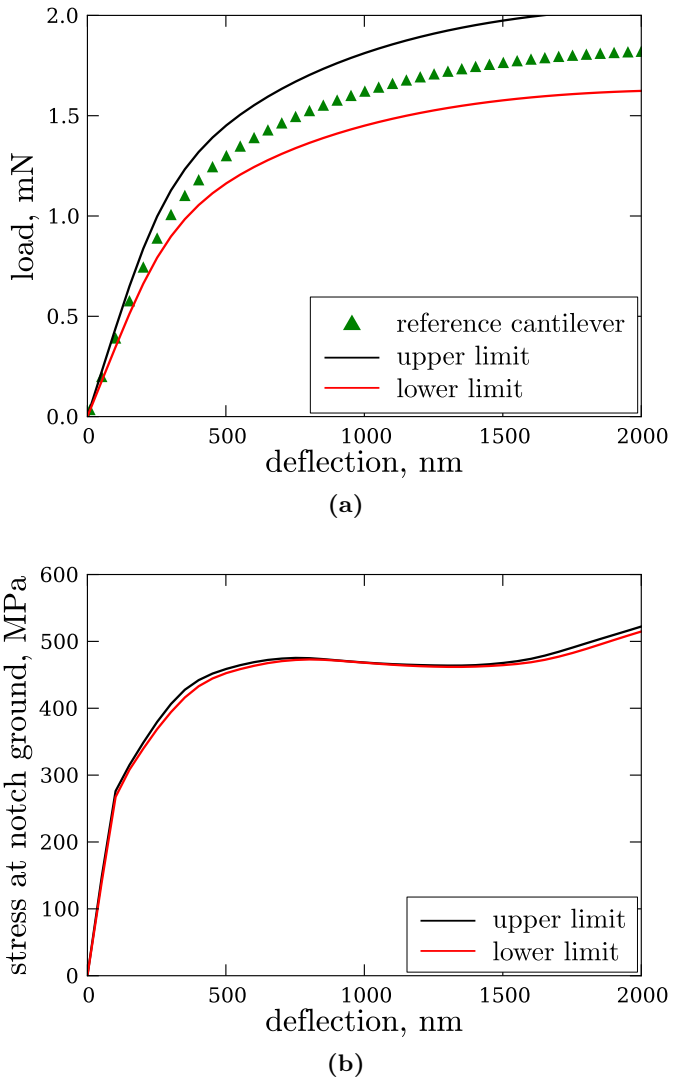

Figure 6.5 (a) Load-deflection response of a cantilever with the dimensions height : width : length = 8.0 µm : 5.0 µm : 20.0 µm together with the upper and lower limits due to deviations in the geometry. (b) Stress at the center of the notch ground for the upper and lower limits.

Deviations of the hardening parameters of the crystal plasticity model also influence the load-displacement response of a cantilever and the stresses at the grain boundary. In particular, the saturation stress, τ_∞, and the initial hardening modulus, h_0, (see section 5.2) determine the stress at a material point after the onset of plastic deformation. Starting with the cantilever geometry associated with the nominal dimensions, the saturation stress was varied by ±10 MPa and the initial

hardening modulus was varied by ±4000 MPa. Figure 6.6(a) illustrates the effect of the variation of the crystal plasticity parameters on the load-displacement curve. The variation of the saturation stress causes an increasing difference of the load with increasing deflection of the cantilever. The variation of the hardening modulus has only little influence on the data during the initial stages of plastic deformation and the differences even decrease at larger deflections.

The evolution of the normal stress along the cantilever axis at the center of the notch ground was determined from the simulations to estimate the effect of the variation of the crystal plasticity parameters on the fracture process 6.6(b). In particular, the saturation stress (solid lines) has a strong influence on the stress at the grain boundary. In contrast, the influence of the initial hardening modulus is moderate (dashed lines).

It is important to note that the crystal plasticity constants were determined to a maximum accumulated plastic strain of 20 %, as shown in chapter 5. Therefore, if the accumulated plastic strain in the cantilever exceeds 20 % the material response at the respective material points must be considered as an extrapolation of the validated material model. The plastic strain within must be assessed for each cantilever explicitly since the geometry and crystal orientation can cause significant differences of the maximum strain between specimens.

In conclusion, deviations of the load-displacement response between the experimental data and the simulations of cantilevers can be caused by uncertainties in the measurement of the geometry and deviations in the parameters of the crystal plasticity model. The stress in the vicinity of the grain boundary is less sensitive to the geometry but strongly depend on the saturation stress provided by the crystal plasticity model. Hence, a precise determination of the crystal plasticity parameters is required.

6.2 Cohesive Zone Model of the Grain Boundary

Figure 6.7 shows the distribution of the normal stress at the grain boundary as provided by the respective finite element simulation. A fracture criterion that is independent of the stress distribution at the grain boundary is required to analyze the fracture of a grain boundary. The cohesive zone modeling provides such a description within the finite element framework [74]. In this section the cohesive zone approach applied within the present work is described.

Description of the Applied Cohesive Zone Model

Since the thickness of a grain boundary is negligibly small, a constitutive law which relates the traction directly to the separation of the crack surfaces was chosen. Such a constitutive behavior is also called a traction-separation law which has three key aspects:

- the elastic part without damage

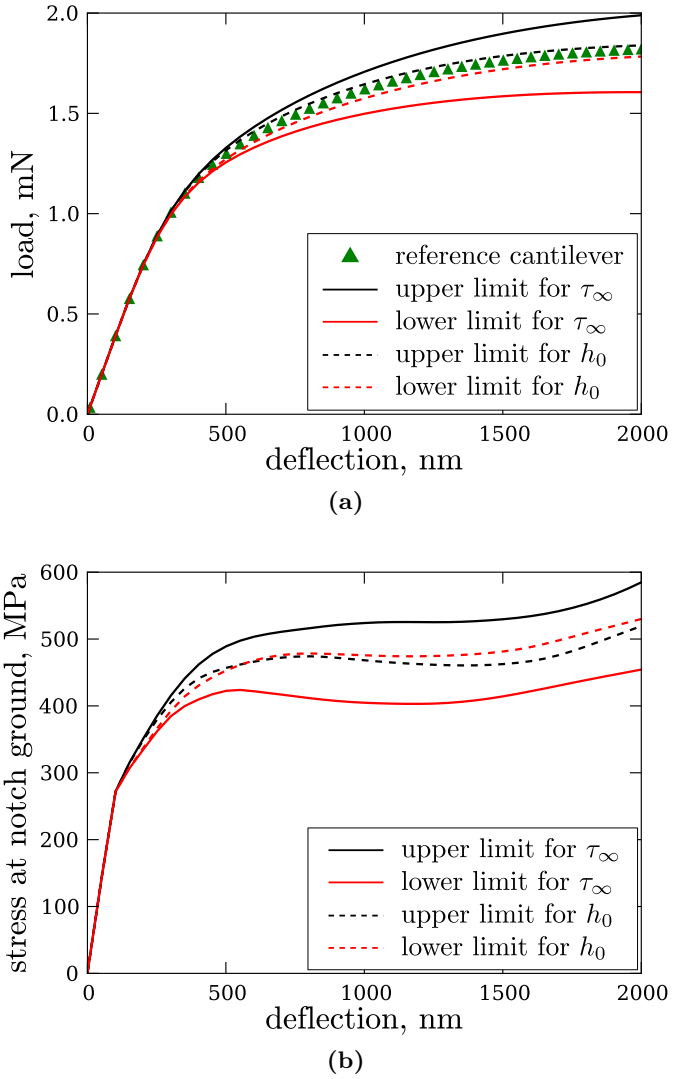

Figure 6.6 (a) Load-deflection response of a cantilever with the dimensions height : width : length = 8.0 µm : 5.0 µm : 20.0 µm. The red lines represent the deviations due to the variations of the initial hardening modulus of ±4000 MPa. The black lines represent the deviations when the saturation stress is varied by ±10 MPa. (b) The evolution of the normal stress at the center of the notch ground.

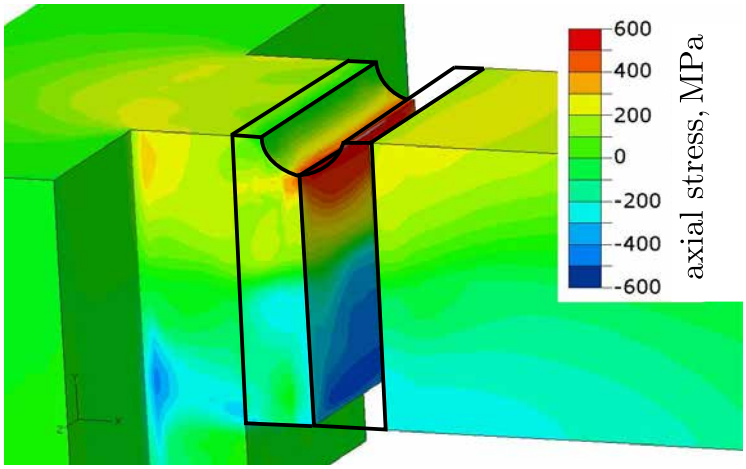

Figure 6.7 Normal stress along the cantilever axis at the grain boundary at the fracture load predicted by a finite element simulation.

- the initiation criterion that defines when damage starts
- the evolution of damage until complete failure

Figure 6.8 gives an illustration of the constitutive behavior of the bilinear traction-separation law used within this work.

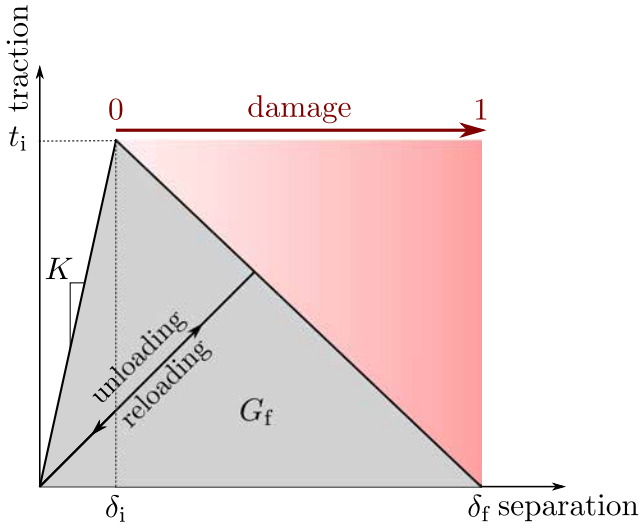

Figure 6.8 Representation of the traction-separation law applied within the present work.

Both the tractions and separations have three components: one normal component perpendicular to the surface and two shear components within the surface following an orthonormal coordinate system. For the present case only the traction-separation behavior normal to the grain boundary plane is considered since no shear

deformation or failure at the grain boundary was observed in the experiments presented here. Within the finite element code ABAQUS the elastic part is assumed to be linear elastic giving:

$$t = K \cdot \varepsilon_\delta = K \cdot \frac{\delta}{e}, \tag{6.1}$$

with t denominating the traction (i. e. stress) normal to the surface, δ being the separation of the crack surfaces and the elastic interface stiffness in absence of damage, K. The initial thickness of the cohesive layer is denoted by e and the strain in the cohesive layer is denoted by ε_δ. Since the cohesive zone represents a two dimensional surface with an infinitesimal thickness, e serves as a parameter for the calculation of the interfacial stiffness and is set to unity.

Damage is initiated when the stress normal to the surface is equal to the initiation traction, t_i. The initiation of damage by shear deformation is prohibited by the model used in this work since normal separation of the grain boundaries has been observed to be the dominant failure mode. Potential consequences of the limitation to normal damage initiation are briefly discussed at the end of this chapter. The damage initiation criterion is expressed in terms of the normal stress, t:

$$\frac{t}{t_\mathrm{i}} = 1. \tag{6.2}$$

It is important to note that only tensile traction generates damage while compressive stresses do not lead to the initiation of damage.

Finally, the evolution of damage needs to be specified. A damage variable, D, represents the damage in the material where $D = 0$ is undamaged material and $D = 1$ represents complete failure. The normal cohesive stress would be, $\bar{t}$, if no damage was present in the cohesive zone. This stress is reduced factor of $(1 - D)$ to calculate the actual cohesive stress after damage initiation, t:

$$t = (1 - D) \cdot \bar{t}. \tag{6.3}$$

Starting at the initiation point, $(\delta_\mathrm{i}, t_\mathrm{i})$, the traction continuously decreases until full fracture is achieved at $D = 1$, thus $t = 0$. Thereby, the maximum separation (i. e. the separation at complete failure) δ_f, is attained which is related to the fracture energy, G_f. For the bilinear traction-separation law the damage variable is given as:

$$D = \frac{\delta_\mathrm{f}(\delta - \delta_\mathrm{i})}{\delta(\delta_\mathrm{f} - \delta_\mathrm{i})} \tag{6.4}$$

where δ_f indicates the separation at complete failure. Following this approach the fracture energy, G_f, is expressed as the area under the traction-separation curve:

$$G_\mathrm{f} = \frac{1}{2}\,\delta_\mathrm{f}\,t_\mathrm{i}. \tag{6.5}$$

Once damage is initiated the material response for unloading is linear elastic with a reduced slope, $K(1 - D)$, compared to the initial slope during loading, K. Finally,

the reloading of the material is subject to the linear elastic behavior with the same reduced stiffness. It is important to note that the definition of damage for the cohesive zone does not correspond to the definition of damage of the cantilever as given in chapter 4. There, damage is described as the global loss of elastic stiffness of a cantilever due to a crack at the grain boundary. Damage in terms of the cohesive zone defines the local loss of load carrying ability at a cohesive element. Only if a large number of cohesive elements are damaged the elastic stiffness of the cantilever is reduced significantly.

Application within the Finite Element Framework

For each cantilever one cohesive layer was introduced at the position of the grain boundary. The cantilever model was separated into three parts: the cohesive zone representing the grain boundary, the supported part and the free part (see figure 6.9). These parts were tied together to ensure continuous displacement over the grain boundary. The meshes of the supported part and the free part were created analogously to the mesh used in section 6.1. The mesh for the cohesive zone was created as an irregular mesh in order to prevent any influences of the mesh structure on the failure. The elements were three dimensional 8-node elements (ABAQUS specification: COH3D8). The average edge length of the cohesive elements was half the edge length of the continuum elements at the notch. From the traction-separation law described previously, three parameters needed to be determined: the initial elastic constant K, the fracture energy to describe the damage propagation, G_f, and the traction at the point of damage initiation, t_i. It is important to note that the fracture energy is related to the separation at complete fracture by equation (6.5) such that these parameters are not independent.

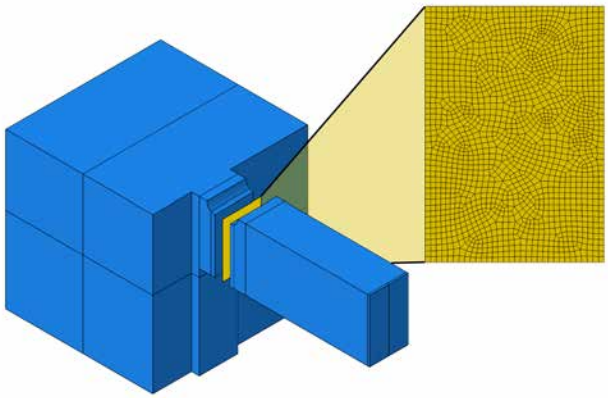

Figure 6.9 Integration of the cohesive zone into the cantilever.

The purpose of the cohesive layer is to provide a fracture criterion within the simulation while the deformation properties are completely captured by the material surrounding the grains. Therefore, the elastic interface stiffness, K, is chosen such that the cohesive layer does not influence the deformation behavior of the can-

tilever. A value of ten times the isotropic elastic modulus of the material ensures a sufficiently high normal stiffness of the cohesive layer. Additionally, the cohesive shear stiffness must be defined such that no shear deformations occur in the cohesive layer. The elastic shear deformations in both shear directions of the cohesive layer in absence of damage are described analogously to equation 6.1.* Therefore, the corresponding stiffness constant, K_S, applies for both shear directions and is set to a value of ten times the isotropic shear modulus.

In chapter 4 it has been shown that the grain boundaries fail without a significant decrease of the elastic stiffness of the cantilever prior to complete fracture. This implies a small fracture energy for the grain boundary, i. e. grain boundary failure is brittle. The determination of the fracture energy in terms of the cohesive zone elements requires crack propagation measurements. Since this was not possible with the present test setup a low value for the fracture energy has been selected. For pure aluminum bi-crystals subject to liquid metal embrittlement crack extension forces on in the range between $0.3\,\mathrm{J/m^2}$ and $3.0\,\mathrm{J/m^2}$ were found depending on the misorientation of the grain boundary [75]. Here a value of $5.0\,\mathrm{J/m^2}$ was used in order to ensure numerical stability of the simulations. The simulation was stopped when the time increment of the quasi static simulation achieved its minimum value of $10^{-5}\,\mathrm{s}$. This was defined as the point of final, complete fracture for the corresponding initiation stress since the quasi static simulations cannot account for the unstable crack propagation.

6.3 Determination of the Initiation Stress for two Representative Cantilevers

From the fracture experiments three representative cases can be identified: (a) grain boundaries that fracture right after the onset of plastic deformation, (b) grain boundaries where the fracture is initiated after extensive plastic deformation and (c) grain boundaries that do not fracture. In order to assess the capabilities of the method developed within this work it was applied to two cantilevers which represent cases (a) and (b) and which will be called cantilever A and cantilever B, respectively. The *post mortem* images of these specimens are shown in figure 6.10. It is worth noting that cantilever A seems to be more strongly deformed than cantilever B. This is basically related to the larger crack length of cantilever A and not to plastic deformation, as can be seen from the load-displacement data given in figures 6.11 and 6.12. The geometry of the cantilevers is given in table 6.1.

The orientation of the grains under the notch of the cantilevers was measured using EBSD prior to the fabrication of the specimens. The Cartesian coordinate system of the EBSD system with reference to the cantilever can be described as follows: the y-axis is parallel to the cantilever axis and the z-axis perpendicular to the top surface of the cantilever (i. g. parallel to the indenter axis). The Eulerian angles in Bunge notation [76] are given in table 6.2 for the respective grains together

*The traction-separation behavior is uncoupled.

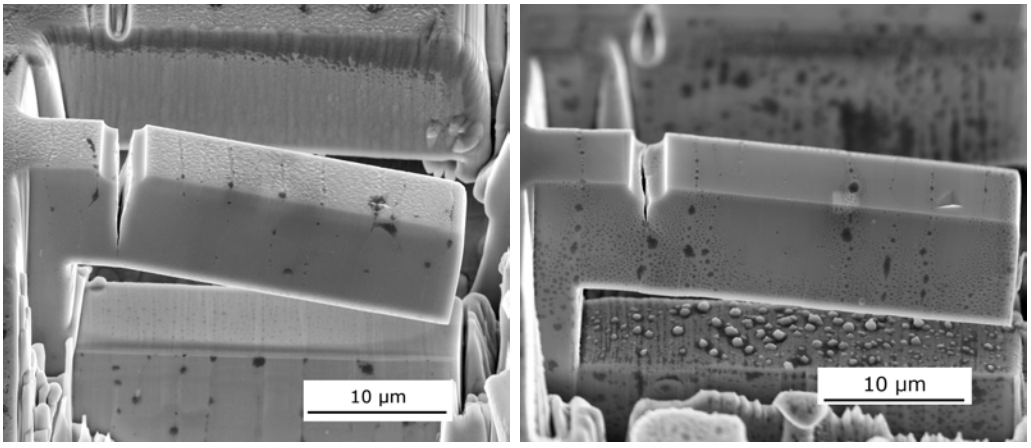

(a) cantilever A **(b)** cantilever B

Figure 6.10 Cantilevers showing fracture (a) directly after the onset of plastic deformation and (b) after pronounced plastic deformation.

cantilever	H, µm	L, µm	B, µm	d, µm	a, µm
A	8.70	21.64	6.13	3.13	1.02
B	9.43	26.70	7.02	4.55	1.13

Table 6.1 Geometry of the cantilevers A and B. H is the cantilever height, L is the cantilever length, B is the cantilever with, d is the position of the notch center and a is the depth of the notch.

with the misorientation angle, θ, referring to a plane grain boundary with its normal parallel to the cantilever axis. Both grain boundaries are high angle grain boundaries with similar misorientation angles on the order of 50°. It is important to note that the misorientation angle is used for a coarse characterization of a perfectly plane grain boundary while the inner structure of the grain boundary is not represented, e. g. local deviations of the grain boundary orientation and particles on the grain boundary plane.

The load-displacement data for cantilever A is given in figure 6.11. The grain boundary of cantilever A fractured at a deflection of (1000 ± 50) nm. The deflection at the point of fracture was approximated with an initiation stress, t_i, of (620 ± 10) MPa assuming a constant fracture energy of $5\,\mathrm{J/m^2}$. Cantilever B showed more plastic deformation prior to fracture at a deflection of (1800 ± 50) nm (see figure 6.12). The deflection at the point of fracture was approximated with an initiation stress, t_i, of (600 ± 10) MPa when the fracture energy was held constant at $5\,\mathrm{J/m^2}$. Hence, both grain boundaries fractured at similar initiation stresses while the cantilever deformation prior to fracture was significantly different. This is consistent with the fact that both grain boundaries showed similar misorientation angles.

cantilever	grain	ϕ_1	Φ	ϕ_2	θ
A	support	148.9°	62.1°	46.2°	47.5°
	free	152.4°	112.6°	55.9°	
B	support	209.4°	108.3°	218.3°	51.5°
	free	87.0°	92.2°	0.3°	

Table 6.2 Orientations of the grains under the notch for cantilevers A and B in terms of Eulerian angles (ϕ_1, Φ, ϕ_2) in the Bunge notation. The label "support" denotes the orientations of the grains close to the supported end, the label "free" denotes the orientations of the grains close to the free end of the cantilever. θ is the misorientation angle of the grain boundary.

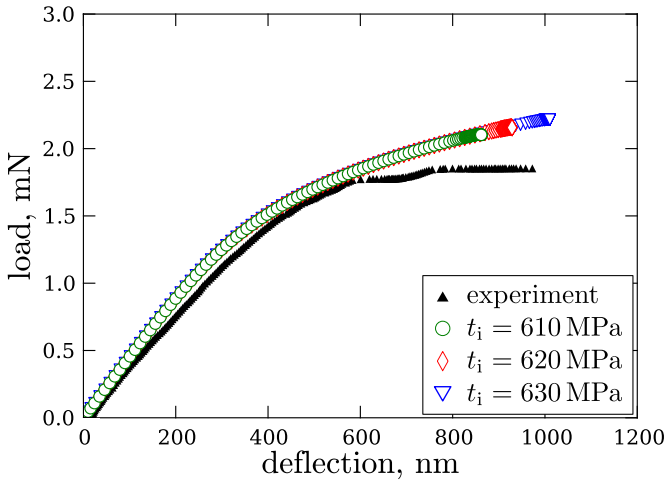

Figure 6.11 Load-displacement data of cantilever A. The cantilever failed at 1000 ± 50 nm. The initiation stress, t_i has been adjusted to match the displacement at failure while the fracture energy was kept constant at $5\,\mathrm{J/m^2}$.

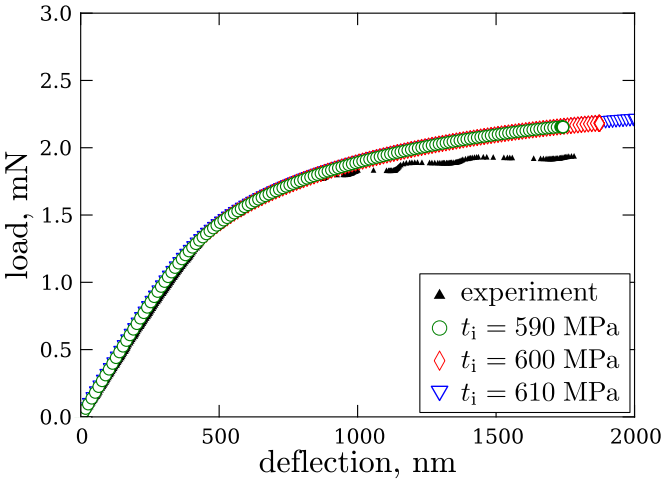

Figure 6.12 Load-displacement data of cantilever B. The cantilever failed at 1800 ± 50 nm. The initiation stress, t_i, has been adjusted to match the displacement at failure while the fracture energy was kept constant at $5\,\mathrm{J/m^2}$.

It is important to note that the simulations did not account for the final fracture process; the rapid failure of the grain boundary negates an analysis of crack propagation. Instead the time increment of the quasi static analysis was reduced down to a minimum value of 10^{-5} s prior to complete fracture. This last point of the simulation is defined as point of fracture for a simulation within this work.

In order to investigate the influence of the fracture energy on the results, the fracture energy was varied by $\pm 1\,\mathrm{J/m^2}$ for both cantilevers while the initiation stress was kept constant at 620 MPa and 600 MPa, respectively. For both cantilevers an increase in fracture energy shifted the final fracture in the simulations to larger values of cantilever deflection. Accordingly, the lower fracture energies shifted the final fracture to lower cantilever deflections. A variation of the fracture energy of 20 %, as given in figure 6.13, results in a variation of the deflection at fracture on the order of 10 %. The cohesive model is more sensitive to a variation of the initiation stress as can be seen from the fact that a variation of the deflection at fracture on the order of 10 % is caused by a variation of the initiation stress by approximately 2 %, as given in figures 6.11 and 6.12.

One possible reason for the significantly different deformation behavior of the cantilevers could be the cantilever geometry. The position of the notch, d, relative to the cantilever length, L, was $\frac{d}{L} = 0.14$ for cantilever A and $\frac{d}{L} = 0.17$ for cantilever B. The difference between these relative positions is not expected to influence the fracture behavior significantly. In turn, the analysis of the fracture stress by the method developed within this work includes effects of the cantilever geometry, which is a major advantage.

Another possible reason for the differences in the deformation behavior between cantilever A and B might be related to different stress distributions at the grain

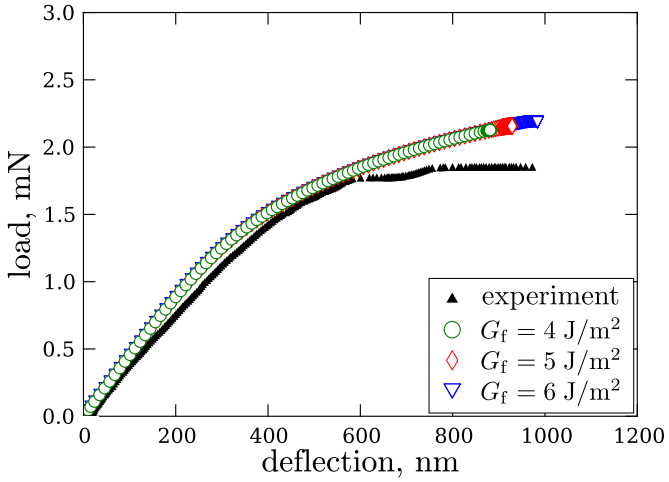

(a) cantilever A

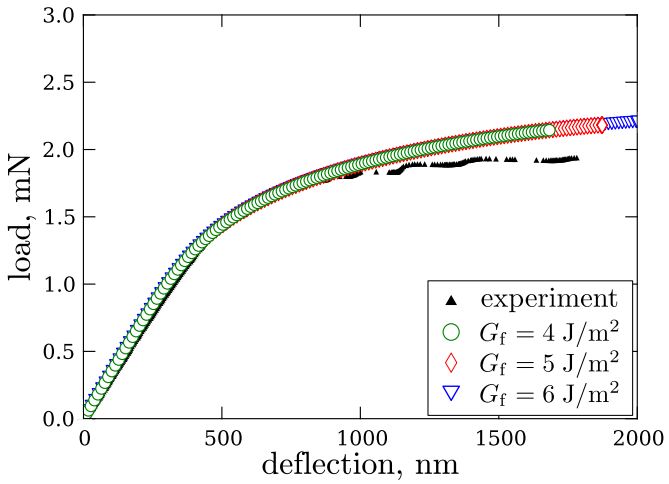

(b) cantilever B

Figure 6.13 Load-displacement data of (a) cantilever A and (b) cantilever B for a variation of the fracture energy, G_f, between 4 J/m^2 and 6 J/m^2. The initiation stress was 620 MPa for cantilever A and 600 MPa for cantilever B. In figure (b) the simulation for a fracture energy of 4 J/m^2 stopped before the increment was broken down for unknown reasons.

boundary. In order to investigate possible influences of the stress distribution, the initiation criterion and the damage in the cohesive zone were considered together with the distribution of the normal stress along the cantilever axis in the grain close to the supported end of the cantilever. An initiation stress of 620 MPa and a fracture energy of $5\,\mathrm{J/m^2}$ were chosen for the following simulations of cantilever A. Damage was initiated at a deflection of 750 nm. The value of the damage initiation criterion for the cohesive elements along the grain boundary is shown in figure 6.14(a). Damage was initiated at the notch ground when the initiation criterion attained a value of 1. This is consistent with the stress distribution in terms of normal stress along the cantilever axis at the grain boundary as depicted in figure 6.14(b). The stress distribution was not symmetric with respect to the center of the cantilever. Probably, this is caused by the anisotropic deformation of the grains and that the fact that the indenter was not positioned at the center of the cantilever axis. This underscores the importance of a three-dimensional simulation with an accurate representation of the position of the indenter and the use of an anisotropic material model. After damage was initiated a damage zone was formed around the locus of initiation at the notch ground, as can be seen for the last increment of the simulation shown in figure 6.14(c), which provides the final state prior to complete fracture. In this case damage approaches the maximum value of 1. The stress distribution at the grain boundary at the moment of fracture is shown in figure 6.14(d).

For the following simulations of cantilever B an initiation stress of 600 MPa and a fracture energy of $5\,\mathrm{J/m^2}$ were chosen. Damage in cantilever B was initiated below the notch ground, as can be seen in figure 6.15(a). The initiation of damage started at a cantilever deflection of 1060 nm. The stress distribution of normal stresses along the cantilever axis at damage initiation is shown in figure 6.15(b), providing its maximum below the notch ground. Moreover, a local maximum was found even further below the center of the notch ground. Such a stress distribution is likely to be caused by the anisotropic deformation of the grains. At the last increment of the simulation, a damage zone was found around the locus of primary damage initiation (see figure 6.15(c)). The stress distribution at the grain boundary within the last increment of the simulation is given in figure 6.15(d).

It is worth noting that the normal stress in the crystal sections close to the damaged zone was up to 10 % higher than the normal stress of the cohesive zone. This could be caused by inaccuracies in the formulation of the cohesive elements in combination with the visco-plastic material used for the crystal plasticity formulation. Moreover, it is important to note that the maximum accumulated plastic strain in the cantilever was locally on the order of 30 % for both cantilevers A and B. Accumulated plastic strains beyond 20 % result in an extrapolation of the of the material response beyond the limits of the determination of the crystal plasticity parameters given in section 5.3. Figure 6.16 shows that the region where the plastic parameters were extrapolated was located at the notch ground. The local stress distribution can be affected by this model depending on the accuracy of the extrapolation. However, the extrapolated material behavior only affects small regions such that no significant influence on the global load-displacement behavior is expected.

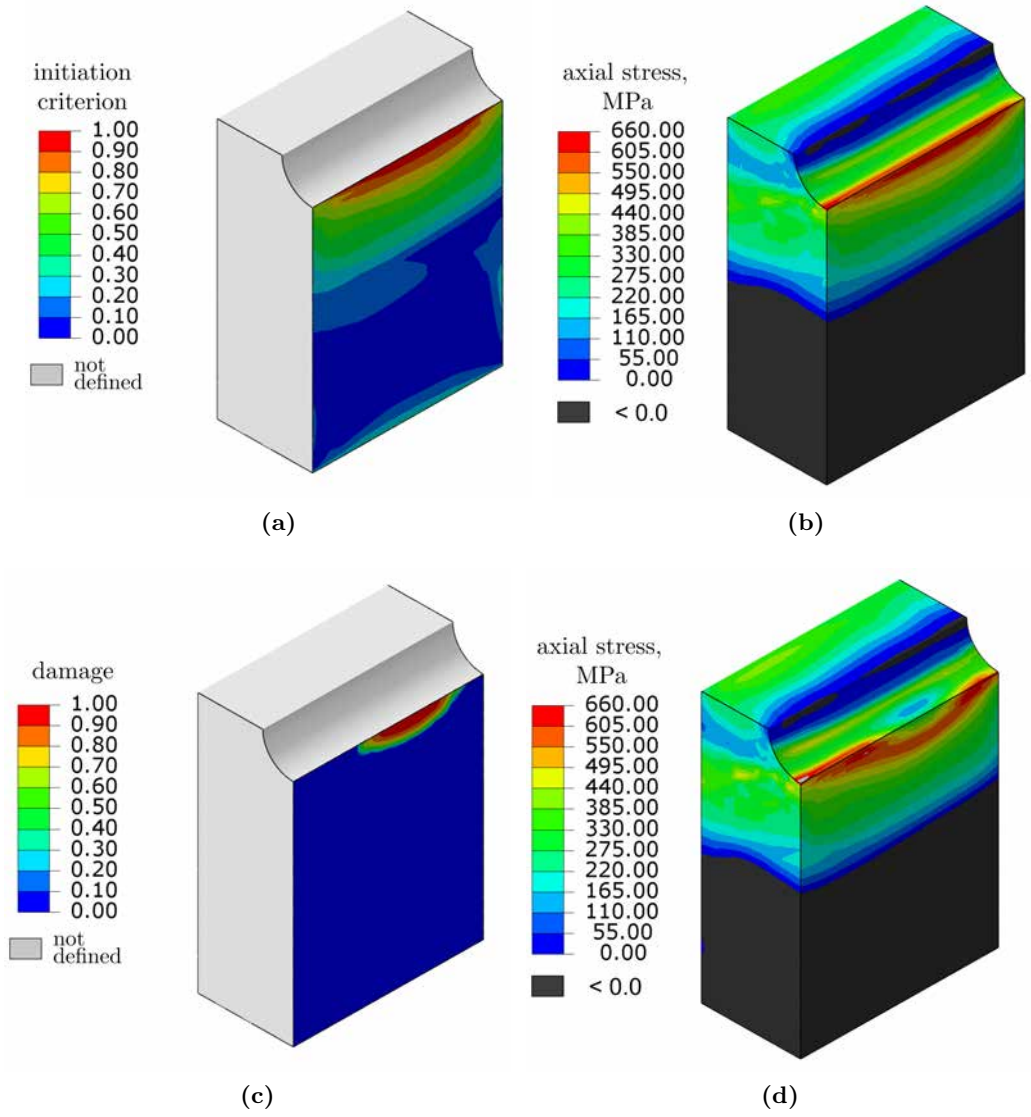

Figure 6.14 Cantilever A: (a) Initiation criterion and (b) stress distribution in the material adjacent to the grain boundary at the moment of initiation. (c) Damage and (d) normal stress distribution at the grain boundary for the last increment of the simulation.

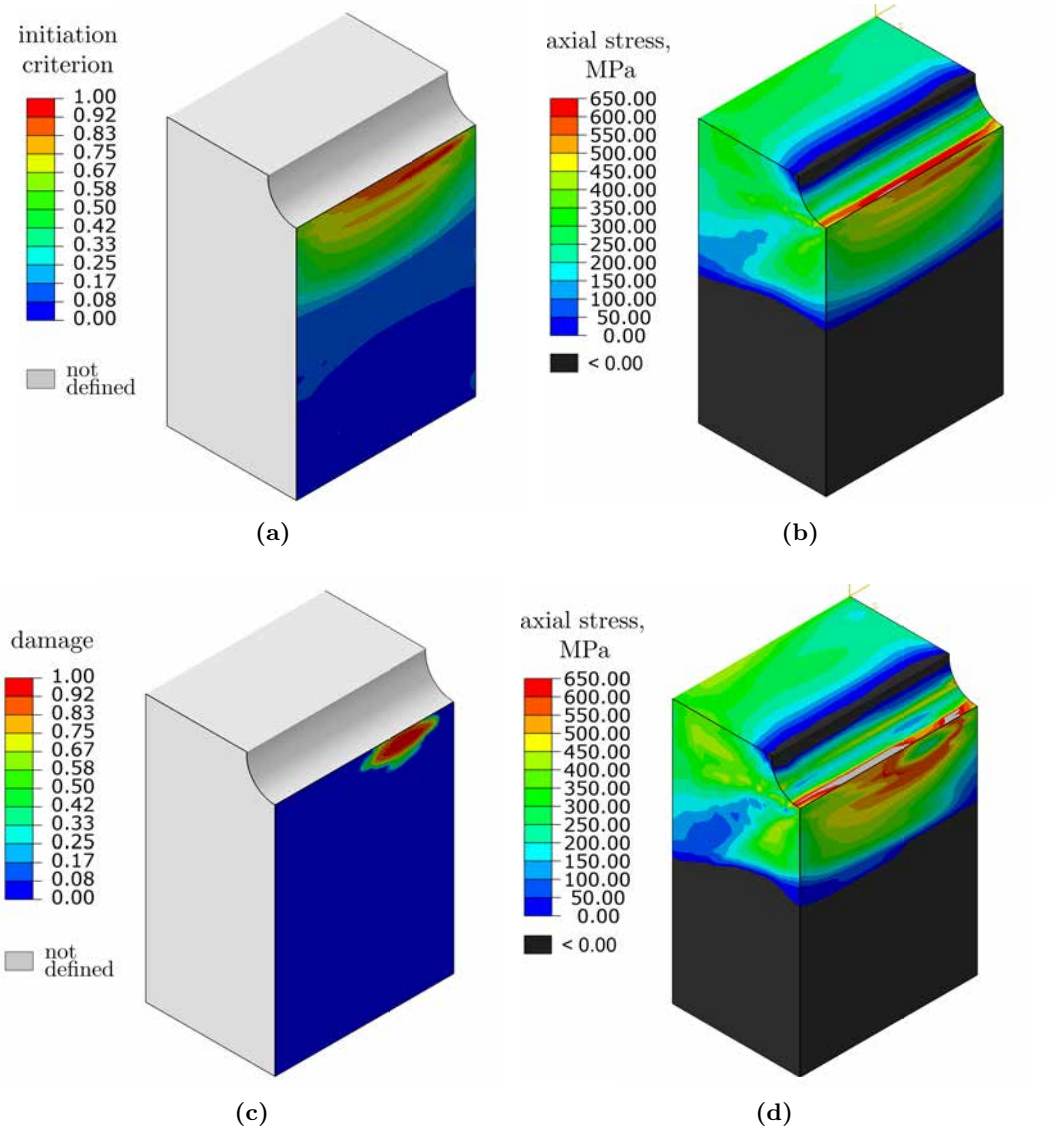

Figure 6.15 Cantilever B: (a) Initiation criterion and (b) stress distribution at the grain boundary at the moment of initiation. (c) Damage and (d) normal stress distribution at the grain boundary for the last increment of the simulation.

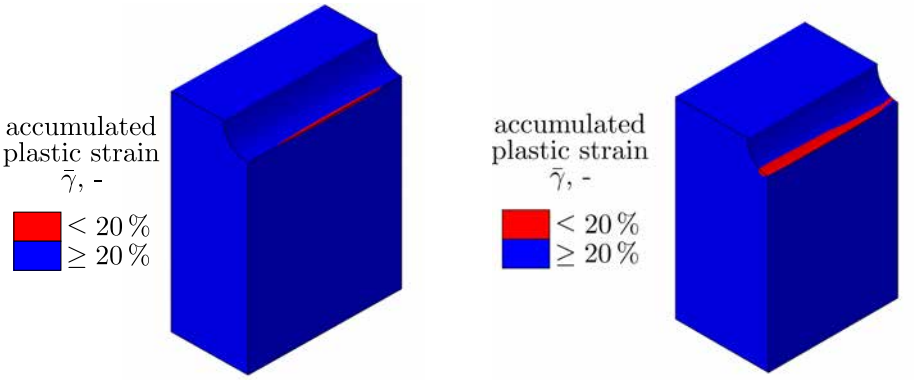

(a) cantilever A **(b)** cantilever B

Figure 6.16 Regions of the material in the grain close to the supported end where the plastic deformation is extrapolated (red domains, $\bar{\gamma} > 20\,\%$) for cantilevers A and B.

This analysis of the stress distribution at the grain boundary depends on the crystal plasticity model used for the simulations and the related boundary conditions at the grain boundary. For the present analysis a continuous displacement over the grain boundary, in absence of complete damage, has been assumed. Other boundary conditions at the grain boundary can significantly influence the stress fields, e. g. the zero shear condition perpendicular to the interface which makes the grain boundary a perfect obstacle to dislocations [77]. Furthermore, possible effects of strain gradients on the stress distribution are neglected within the present model. These effects are subject to current research activities [78, 35]. Moreover, particles and or precipitates on the grain boundary alter the stress field in the vicinity of the grain boundary locally. Finally, the actual structure of the grain boundary may deviate from the assumption of a perfectly plane boundary.

In conclusion, the model used in the present analysis sufficiently approximates the plastic deformation of the grains in the present model, although, it is not expected to provide an exact representation of the stress field at the grain boundary. The initiation stress in terms of the cohesive zone model is, thus, related to the inner structure of the grain boundary and possible effects of the boundary conditions and strain gradients.

Summary

- The adjusted model of crystal plasticity can be successfully transfered from micro-columns to micro-cantilever specimens.
- The cantilever model has been extended by a cohesive zone for investigations into fracture parameters.

- The method presented here for grain boundary fracture analysis of single brittle grain boundaries in ductile metals has been applied to two cantilever specimens with significantly different deformation characteristics but similar misorientations of the grain boundary of interest. Despite the differences in the deformation behavior, the method identified similar damage initiation stresses for both grain boundaries.
- The cohesive zone model for brittle fracture is more sensitive to the initiation stress than to the fracture energy. Therefore, the initiation stress was adjusted for the brittle fracture of the grain boundary while the fracture energy was held constant at $5\,\mathrm{J/m^2}$.
- The crystal plasticity model approximates the plastic deformation of the grains with sufficient accuracy to determine the initiation stress in terms of the cohesive zone model. This initiation stress is related to the inner structure of the grain boundary and possible effects of the boundary conditions at the grain boundary and strain gradient effects.

7 Conclusions

Within the present work a method for the separation of single grain boundaries in plastically deforming metals has been presented. Notched micro-cantilever specimens were fabricated from the aluminum-lithium alloy 2198 using focused ion beam milling with a gallium ion source. The specimens were fabricated with a U-notch placed at the boundary of interest close to the supported end of the cantilever. The FIB fabrication lead to the embrittlement of the grain boundaries which helped to increase the number of successfully tested specimens; a great benefit for the development of the method. Using a nanoindenter the cantilevers were bent to fracture. The cantilevers were deformed plastically and no significant decrease of the elastic stiffness was found prior to fracture. It can be concluded that the fracture of the grain boundaries is brittle while all permanent deformation of the cantilevers can be attributed to the plastic deformation of the grains. Making use of a finite element model including an isotropic elastic constitutive law, specimens with varying geometries were compared to each other. In the analysis of the specimens it was found that the actual lateral stiffness of the indenter must be included in the finite element simulations to provide accurate results.

In order to capture the anisotropic plastic deformation of the grains a crystal plasticity finite element model was applied. It has been shown that in technical alloys, where single crystals of the respective tempers are usually not available, the parameters for the crystal plasticity model can be successfully determined by using a hybrid approach combining micro-compression tests and finite element simulations incorporating the material model. However, further investigations are required since no match between experiment and simulation could be achieved for the specific case when a [1 1 1] crystal orientation is aligned with the column axis.

The crystal plasticity model adjusted from micro-compression experiments has been transfered to the oligo-crystalline cantilevers. The finite element simulations predicted the deformation behavior of these cantilevers both globally, as shown by the load-displacement curves, and locally, as shown by the DIC measurement of the displacement field. Thus, it is possible to use crystal plasticity parameters determined from micro-compression experiments to predict the deformation of a micro-cantilever.

Finally, the finite element simulations of the cantilevers were extended by a cohesive zone. The initiation stress at the grain boundary was adjusted in terms of the traction-separation law of the cohesive zone. The simulations were more sensitive to the initiation stress for fracture than to the fracture energy. Therefore, the fracture energy was assumed to have a low constant value. This is consistent with the fact that no propagation of a grain boundary crack could be measured from the

experiments. However, such measurements would be required for the determination of the fracture energy in terms of the cohesive zone model.

The methodology presented within this work can be used to investigate the fracture properties of a specific single grain boundary. The anisotropic plastic deformation of the grains adjacent to the grain boundary of interest is sufficiently described within this model to determine an initiation stress for a specific grain boundary in terms of a cohesive zone model. This initiation stress is related to the inner structure of the grain boundary and possible effects of strain gradients and boundary conditions at the grain boundary.

In the future such experiments may assist in investigations of the influence of the structure of grain boundaries in technical alloys on the fracture behavior [2] and in the research of liquid metal embrittlement of grain boundaries [75, 79]. For such investigations the determination of the fracture energy depending on the character of the respective grain boundary is important. This requires experiments with measurable crack propagation. Possibly, this can be achieved by using trapezoidal cross-sections of the cantilevers which provide increasing crack widths with increasing crack lengths. Moreover, the methodology can be extended to investigate the influence of shear stresses on the failure of grain boundaries. However, any influence from the ions used during the FIB preparation of the specimens on the grain boundary properties must be avoided. Hence, for aluminum alloys the gallium source must be replaced. A good candidate is a xenon plasma source which is currently under development.

Bibliography

[1] S Suresh, AK Vasudevan, M Tosten and PR Howell. Microscopic and macroscopic aspects of fracture in lithium containing aluminum alloys. *Acta Metallurgica*, 35:25–46, 1987.

[2] AK Vasudevan and RD Doherty. Grain boundary ductile fracture in precipitation hardened aluminum alloys. *Acta Metallurgica*, 35:1193–1219, 1987.

[3] WC Oliver and GM Pharr. An improved technique for determining hardness and elastic modulus using load and displacement sensing indentation experiments. *Journal of Materials Research*, 7:1564–1583, 1992.

[4] WC Oliver and GM Pharr. Measurement of hardness and elastic modulus by instrumented indentation: Advances in understanding and refinements to methodology. *Journal of Materials Research*, 19:3–20, 2004.

[5] DM Ebenstein and LA Pruitt. Nanoindentation of biological materials. *Nanotoday*, 1:26–33, 2006.

[6] G Lewis and Nyman JS. The use of nanoindentation for characterizing the properties of mineralized hard tissues: State-of-the art review. *Journal of Biomedical Materials Research Part B: Applied Biomaterials*, 87B:286–301, 2008.

[7] G Constantinides, FJ Ulm and K van Vliet. On the use of nanoindentation for cementitious materials. *Materials and Structures*, 36:191–196, 2003.

[8] CA Botero, E Jiminez-Pique, C Baudin, N Salan and L Llanes. Nanoindentation of Al2O3/Al2TiO5 composites: Small-scale mechanical properties of Al2TiO5 as reinforcement phase. *Journal of the European Ceramic Society*, in Press, 2012.

[9] T Burgess and M Ferry. Nanoindentation of metallic glasses. *Materials Today*, 12:24–32, 2009.

[10] EG Herbert, WC Oliver and GM Pharr. Nanoindentation and the dynamic characterization of viscoelastic solids. *Journal of Applied Physics D*, 41:074021–074021–9, 2008.

[11] S Suresh, TG Nieh and BW Choi. Nano-indentation of copper thin films on silicon substrates. *Scripta Materialia*, 41:951–957, 1999.

[12] N Huber, WD Nix and H Gao. Identification of elastic-plastic material parameters from pyramidal indentation of thin films. *Proceedings of the Royal Society of London Series A*, 458:1593–1620, 2002.

[13] R Saha and WD Nix. Effects of the substrate on the determination of thin film mechanical properties by nanoindentation. *Acta Materialia*, 50:23–38, 2002.

[14] N Huber and C Tsakmakis. Determination of constitutive properties from spherical indentation data using neural networks, Part I: the case of pure kinematic hardening in plasticity laws. *Journal of the Mechanics and Physics of Solids*, 47:1569–1588, 1999.

[15] N Huber and C Tsakmakis. Determination of constitutive properties from spherical indentation data using neural networks, Part II: plasticity with nonlinear isotropic and kinematic hardening. *Journal of the Mechanics and Physics of Solids*, 47:1589–1607, 1999.

[16] MD Uchic, DM Dimiduk, JN Florando and WD Nix. Sample dimensions influence strength and crystal plasticity. *Science*, 305:986–989, 2004.

[17] O Kraft, M Hommel and E Arzt. X-ray diffraction as a tool to study the mechanical behaviour of thin films. *Materials Science and Engineering*, A288:209–216, 2000.

[18] JH Han and MTA Saif. In situ microtensile stage for electromechanical characterization of nanoscale freestanding films. *Review of Scientific Instruments*, 77:045102–045102–8, 2006.

[19] N Andre, M Colombier, V de Longeville, D Fabregue, T Gets, S Gravier, T Pardoen and JP Raskin. Microfabrication-based nanomechanical laboratory for testing the ductility of submicron aluminium films. *Microelectronic Engineering*, 84:2714–2718, 2007.

[20] D Kiener, W Grosinger, G Dehm and R Pippan. A further step towards an understanding of size-dependent crystal plasticity: In situ tension experiments of miniaturized single-crystal copper samples. *Acta Materialia*, 56:580–592, 2008.

[21] CA Volkert and ET Lilleodden. Size effects in the deformation of sub-micron Au columns. *Philosophical Magazine*, 86:5567–5579, 2006.

[22] D Kiener, C Motz, T Schöberl, M Jenko and G Dehm. Determination of mechanical properties of copper at the micron scale. *Advanced Engineering Materials*, 8:1119–1125, 2006.

[23] MD Uchic, PA Shade and DM Dimiduk. Micro-compression testing of FCC metals: a selected overview of experiments and simulations. *Journal of Materials Research*, 61:36–41, 2009.

[24] WD Nix, JR Greer, G Feng and ET Lilleodden. Deformation at the nanometer and micrometer length scales: Effects of strain gradients and dislocation starvation. *Thin Solid Films*, 515:3152–3157, 2007.

[25] TA Parthasarathy, SI Rao, DM Dimiduk, MD Uchic and DR Trinkle. Contribution to size effect of yield strength from the stochastics of dislocation source lengths in finite samples. *Scripta Materialia*, 56:313–316, 2007.

[26] C Motz, D Weygand, J Senger and P Gumbsch. Initial dislocation structures in 3-D discrete dislocation dynamics and their influence on microscale plasticity. *Acta Materialia*, 57:1744–1754, 2009.

[27] H Zhang, BE Schuster, Q Wei and KT Ramesh. The design of accurate micro-compression experiments. *Scripta Materialia*, 54:181–186, 2006.

[28] D Kiener, C Motz and G Dehm. Micro-compression testing: A critical discussion of experimental constraints. *Materials Science and Engineering A*, 505:79–87, 2009.

[29] C Kirchlechner, J Keckes, J Micha and G Dehm. In situ microlaue: Instrumental setup for the deformation of micron sized samples. *Advanced Engineering Materials*, 13:837–844, 2011.

[30] D Raabe, D Ma and F Roters. Effects of initial orientation, sample geometry and friction on anisotropy and crystallographic orientation changes in single crystal microcompression deformation: A crystal plasticity finite element study. *Acta Materialia*, 55:4567–4583, 2007.

[31] TP Weihs, S Hong, JC Bravman and WD Nix. Mechanical deflection of cantilever microbeams: A new technique for testing the mechanical properties of thin films. *Journal of Materials Research*, 3:931–942, 1988.

[32] JN Florando and WD Nix. A microbeam bending method for studying stress-strain relations for metal thin films on silicon substrates. *Journal of the Mechanics and Physics of Solids*, 53:619–638, 2005.

[33] JS Stölken and AG Evans. A microbend test method for measuring the plasticity length scale. *Acta Materialia*, 46:5109–5115, 1998.

[34] C Motz, R Pippan and T Schöberl. Mechanical properties of micro-sized copper bending beams machined by the focused ion beam technique. *Acta Materialia*, 53:4269–4279, 2005.

[35] E Demir, D Raabe and F Roters. The mechanical size effect as a mean-field breakdown phenomenon: Example of microscale single crystal beam bending. *Acta Materialia*, 58:1876–1886, 2010.

[36] J Gong and AJ Wilkinson. Anisotropy in the plastic flow properties of single-crystal α titanium determined from micro-cantilever beams. *Acta Materialia*, 57:5693–5705, 2009.

[37] J Gong and AJ Wilkinson. A microcantilever investigation of size effect, solid-solution strengthening and second-phase strengthening for $\langle a \rangle$ prism slip in α-Ti. *Acta Materialia*, 59:5970–5981, 2011.

[38] CJ Wilson, A Ormeggi and M Narbutovskih. Fracture testing of silicon microcantilever beams. *Journal of Applied Physics*, 59:2386–2393, 1996.

[39] TP Halford, K Takashima, Y Higo and P Bowen. Fracture test of microsized TiAl specimens. *Fatigue and Fracture of Engineering Materials and Structures*, 28:695–701, 2005.

[40] K Matoy, H Schönherr, T Detzel, T Schöberl, R Pippan, C Motz and G Dehm. A comparative micro-cantilever study of the mechanical behavior of silicon based passivation films. *Thin Solid Films*, 518:247–256, 2009.

[41] F Iqbal, J Ast, M Göken and K Durst. In situ micro-cantilever tests to study fracture properties of NiAl single crystals. *Acta Materialia*, 60:1193–1200, 2012.

[42] T Klüsner, S Wurster, P Supancic, R Ebner, M Jenko, J Glätzle, A Püschel and R Pippan. Effect of specimen size on the tensile strength of WC–Co hard metal. *Acta Materialia*, 59:4244–4252, 2011.

[43] H Hirakata, Y Takahashi, VD Truong and T Kitamura. Role of plasticity on interface crack initiation from a free edge and propagation in a nano-component. *International Journal of Fracture*, 145:261–271, 2007.

[44] P Zhao, F Shang, Y Yan and T Kitamura. Reinvestigation of the effect of plasticity on delamination process of Si/Cu interface in a ductile nano-cantilever. *International Journal of Fracture*, 161:65–78, 2010.

[45] K Matoy, T Detzel, M Müller, C Motz and G Dehm. Interface fracture properties of thin films studied by using the micro-cantilever deflection technique. *Surface and Coatings Technology*, 204:878–881, 2009.

[46] DEJ Armstrong, ME Rogers and SG Roberts. Micromechanical testing of stress corrosion cracking of individual grain boundaries. *Scripta Materialia*, 61:741–743, 2009.

[47] DEJ Armstrong, AJ Wilkinson and SG Roberts. Micro-mechanical measurements of fracture toughness of bismuth embrittled copper grain boundaries. *Philosophical Magazine Letters*, 91:394–400, 2011.

[48] CA Volkert and AM Minor. Focused ion beam microscopy and micromachining. *MRS Bulletin*, 32:389–399, 2007.

[49] H Bei, S Shim, EP George, MK Miller, EG Herbert and GM Pharr. Compressive strengths of molybdenum alloy micro-pillars prepared using a new technique. *Scripta Materialia*, 57:397–400, 2007.

[50] D Tabor. The hardness of solids. *Review of Physics in Technology*, 1:145–179, 1970.

[51] J Illingworth and J Kittler. A survey of the hough transform. *Computer Vision, Graphics and Image Processing*, 44:87–116, 1988.

[52] C Maurice and R Fortunier. A 3D hough transform for indexing EBSD and Kossel patterns. *Journal of Microscopy*, 230:520–529, 2008.

[53] HA Bruck, SR McNeill, MA Sutton and WH Peters. Digital image correlation using newton-raphson method of partial differential correction. *Experimental Mechanics*, 29:261–267, 1989.

[54] TC Chu, WF Ranson, MA Sutton and WH Peters. Applications of digital-image-correlation techniques to experimental mechanics. *Experimental Mechanics*, 25:232–244, 1985.

[55] Z Wang and P Vo. A free 2D and 3D digital image corellation (DIC) moire software. Avaliable at http://www.opticist.org/node/73.

[56] R Becker, A Nedleman, S Suresh, V Tvergaard and AK Vasudevan. An analysis of ductile failure by grain boundary void growth. *Acta Metallurgica*, 37:99–120, 1989.

[57] T Pardoen, D Dumont, A Deschamps and Y Brechet. Grain boundary versus transgranular ductile failure. *Journal of the Mechanics and Physics of Solids*, 51:637–665, 2003.

[58] PNT Unwin and GC Smith. The microstructure and mechanical properties of Al-6 percent Zn-3 percent Mg. *Journal of the Institute of Metals*, 97:299–310, 1969.

[59] AK Vasudevan, EA Ludwiczak, SF Baumann, RD Doherty and MM Kersker. Fracture behavior in Al-Li alloys: role of grain boundary delta. *Materials Science and Engineering*, 72:L25–L30, 1985.

[60] P Cavaliere and A de Santis. Effect of anisotropy on fatigue properties of AA2198 Al-Li plates joined by friction stir welding. *Metallurgical Science and Technology*, 26:21–30, 2008.

[61] D Schnubel. *Laser heating as approach to retard fatigue crack growth in aircraft aluminium structures*. PhD thesis, Helmholtz-Zentrum Geesthacht, Technische Universität Hamburg-Harburg, 2012. HZG Report 2012–5.

[62] D Kupka and H Ovri. Nanoindentation measurement of the elastic modulus in AA2198. Private Communication.

[63] Standard test method for measurement of fracture toughness, ASTM E1820. Annual Book of ASTM Standards, Volume 03.01, 2008. 1070–1117.

[64] E Goens. Elastizitätskonstanten des Aluminiumeinkristalls. *Annalen der Physik*, 14:233–242, 1933.

[65] JCM Li and YT Chou. The role of dislocations in the flow stress grain size relationships. *Metallurgical Transactions*, 1:1145–1159, 1970.

[66] R Maaß, S Van Petegem, D Grolimund, H Van Swygenhoven, D Kiener and G Dehm. Crystal rotation in Cu single crystal micropillars: In situ laue and electron backscatter diffraction. *Applied Physics Letters*, 92:071905–071905–3, 2008.

[67] Y Huang. A user material subroutine incorporating single crystal plasticity in the abaqus finite element program, technical report mech 178. Technical report, Harvard University, Division of applied sciences, 1991.

[68] D Peirce, RJ Asaro and Needleman A. An analysis of nonuniform and localized deformation in ductile sigle crystals. *Acta Metallurgica*, 30:1087–1119, 1982.

[69] RJ Asaro. Crystal plasticity. *J. Appl. Mech.-Trans.*, 50:921–934, 1983.

[70] RJ Asaro. Micromechanics of crystals and polycrystals. *Advances in Applied Mechanics*, 23:1–115, 1983.

[71] S Graff. *Micromechanical Modeling of Deformation in hcp Metals*. PhD thesis, Technische Universität Berlin, Germany, 2007.

[72] ET Lilleodden. Microcompression study of Mg (0001) single crystal. *Scripta Materialia*, 62:532–535, 2010.

[73] F Roters, P Eisenlohr, L Hantcherli, DD Tjahjanto, TR Bieler and D Raabe. Overview of constitutive laws, kinematics, homogenization and multiscale methods in crystal plasticity finite-element modeling: Theory, experiments, applications. *Acta Materialia*, 58:1152–1211, 2010.

[74] *ABAQUS Analysis User's Manual (version 6.11), 31.5 Cohesive Elements, Dassault Systèmes, 2011.*

[75] JA Kargol and DL Albright. The effect of relative crystal orientation on the liquid metal induced grain boundary fracture of aluminum bicrystals. *Metallurgical Transactions A*, 8:27–34, 1977.

[76] V. Randle and O. Engler. *Introduction to Texture Analysis*. Gordon and Breach Science Publishers, 2000.

[77] LP Evers, WAM Brekelmans and MGD Geers. Scale dependent crystal plasticity framework with dislocation density and grain boundary effects. *International Journal of Solids and Structures*, 41:5209–5230, 2004.

[78] A Ma, F Roters and D Raabe. On the consideration of interactions between dislocations and grain boundaries in crystal plasticity finite element modeling –theory, experiments, and simulations. *Acta Materialia*, 54:2181–2194, 2006.

[79] KA Unocic, MJ Mills and GS Daehn. Effect of gallium focussed ion beam milling on preparation of aluminum thin foils. *Journal of Microscopy*, 240:227–238, 2010.

Vorabveröffentlichung

D Kupka and ET Lilleodden. Mechanical testing of solid-solid interfaces at the microscale. *Experimental Mechanics*, 52:649–658, 2012

Danksagung

Die vorliegende Arbeit entstand während meiner Tätigkeit als wissenschaftlicher Mitarbeiter in der Abteilung Experimentelle Werkstoffmechanik der Helmholtz-Zentrum Geesthacht GmbH.

Herrn Prof. Dr.-Ing. habil. Norbert Huber danke ich für die Möglichkeit diese Arbeit am Institut für Werkstoffmechanik am Helmholtz-Zentrum Geesthacht anfertigen zu dürfen. Sein großes Engagement bei der Initiierung und Umsetzung von Forschungsvorhaben werden mir in Erinnerung bleiben, ebenso wie seine Offenheit gegenüber neuen Ideen und deren Umsetzung. Des Weiteren möchte ich Herrn Prof. Dr. rer. nat. Gerold Schneider für die Übernahme des Zweitgutachtens dieser Arbeit danken.

Besonders bedanken möchte ich mich bei Frau Dr. Erica Lilleodden für die Betreuung und ihren persönlichen Einsatz.

Herrn Dr. Ingo Scheider und Herrn Dr. Dirk Steglich danke ich für die Unterstützung bei der Umsetzung der Simulationen. Bei Frau Julia Hütsch und Frau Petra Fischer möchte ich mich für die Hilfe bei der Erarbeitung der grundlegenden Methoden zur Durchführung der mikro-mechanischen Experimente bedanken. Darüber hinaus bin ich Herrn Dr. Dirk Schnubel für die Diskussionen sowie das Korrekturlesen der Arbeit dankbar.

Mein Dank gilt den ehemaligen und derzeitigen Mitarbeitern der Abteilungen Experimentelle Werkstoffmechanik und Simulation von Werkstoff- und Strukturverhalten für die angenehme Arbeitsatmosphäre und ihre Unterstützung.

Nicht zuletzt bedanke ich mich bei Herrn Dr. Jürgen Markmann, Herrn Dr. Markus Ziehmer, Anne Groth, Josephin Enz und Stefan Riekher für die Hilfe bei der Ausrichtung der kleinen Feier nach meiner Promotionsprüfung.

Meinen Eltern Wolfgang und Brigitte Kupka danke ich besonders für die vorbehaltlose Unterstützung und den Rückhalt bei allen Entscheidungen.